Microgravity flow boiling experiments with liquid-vapor mixture inlet onboard the International Space Station

Issam Mudawar[a,*], V.S. Devahdhanush[a], Steven J. Darges[a],

Mohammad M. Hasan[b], Henry K. Nahra[b], R. Balasubramaniam[c], Jeffrey R. Mackey[d]

[a] Purdue University Boiling and Two-Phase Flow Laboratory (PU-BTPFL), School of Mechanical Engineering, Purdue University, 585 Purdue Mall, West Lafayette, IN 47907, USA

[b] NASA Glenn Research Center, 21000 Brookpark Road, Cleveland, OH 44135, USA

[c] Case Western Reserve University, 10900 Euclid Ave., Cleveland, OH 44106, USA

[d] HX5, LLC 3000 Aerospace Parkway, Brookpark, OH 44142, USA

Abstract – This article is part of a series of studies culminating from the multi-objective Flow Boiling and Condensation Experiment (FBCE) onboard the International Space Station, which utilized the Flow Boiling Module (FBM) for experiments between February and July 2022. This study investigates microgravity flow boiling of n-Perfluorohexane with liquid-vapor mixture (two-phase) inlet conditions to the FBM with either one or two opposite walls heated. The FBM's channel has a rectangular cross-sectional area of 5.0 × 2.5 mm^2 and a heated length of 114.6 mm. Key parameters of interest include mass velocity (180 – 2400 kg/m^2s), inlet quality (-0.01 – 0.87), inlet pressure (120 – 200 kPa), and heat flux (1.8 W/cm^2 to critical heat flux), and a large database is amassed. The flow is visualized via a high-speed video camera and photographs are recorded at each heating increment to assess the periodic flow patterns within the channel and the near-wall interfacial behavior. Flow patterns are complex and mainly characterized by high- and low-density fronts alternately traversing the channel to yield high- and low-density-dominant periods of boiling. At all operating conditions, high-density fronts are faster during high-density-dominant periods. At low inlet qualities, the flow is annular near the channel inlet with a central vapor core surrounded by an annular liquid layer. Each high-density front having a high liquid fraction leaves a thin liquid layer sheared onto the heated walls. Boiling occurs within the liquid layer and a vapor layer is formed next to the heated wall. Inlet quality and mass velocity most dictate the overall flow patterns followed by heating configuration, and to a much lesser extent, heat flux and inlet pressure. Heat transfer characteristics are assessed via averaged boiling curves, streamwise profiles of wall temperature and heat transfer coefficient, and parametric curves of local and averaged heat transfer coefficients. Inlet pressure has an insignificant effect on heat transfer. At similar operating conditions, both the heating configurations yield similar trends and values of heat transfer coefficient and critical heat flux (CHF, slightly higher for single-sided) even though double-sided heating adds twice the heat to the fluid and doubly raises local quality. The heat fluxes required for both onset of nucleate boiling degradation and CHF are larger at high mass velocities and low inlet qualities. For a fixed inlet quality, high mass velocities yield higher average heat transfer coefficients at both lower and higher heat fluxes, while the nucleate boiling regime at intermediate heat fluxes is unaffected. For a fixed mass velocity, higher inlet qualities

yield higher and lower average heat transfer coefficients at lower and higher heat fluxes, respectively.

Keywords: microgravity; flow boiling; liquid-vapor mixture inlet; flow patterns; high-density fronts; heating configuration; two-phase heat transfer coefficient; International Space Station

* Author to whom correspondence should be addressed; Tel. (765) 494-5705; Fax (765) 494-0539; E-mail: *mudawar@ecn.purdue.edu;* Website: *https://engineering.purdue.edu/BTPFL*

Nomenclature

D_h	hydraulic diameter [m]
$\bar{f}_{HDF}$	frequency of HDFs averaged along channel length [Hz]
G	mass velocity [kg/m^{2}s]
g	gravitational acceleration [m/s^2]
g_e	gravitational acceleration on Earth [m/s^2]
μg_e	microgravity [m/s^2]
H	height of channel's cross section [m]
H_{tc}	conduction distance through heating strip [m]
h	enthalpy [J/kg]; heat transfer coefficient [W/m^{2}K]
$\bar{h}$	average heat transfer coefficient [W/m^{2}K]
h_{fg}	latent heat of vaporization [J/kg]
k	thermal conductivity [W/m.K]
L_d	upstream development length [m]
L_e	downstream exit length [m]
L_h	heated length [m]
$\dot{m}$	mass flow rate [kg/s]
N_z	number of streamwise measurement locations
P_h	heated perimeter [m]
p	pressure [Pa]
q	heat [W]
q''	heat flux [W/m^2]
q''_{CHF}	critical heat flux [W/m^2]
q''_{ONBD}	heat flux corresponding to ONBD [W/m^2]
$\%q$	percentage of heat flux [% of W/m^2]
T	temperature [°C]
$\bar{T}$	average temperature [°C]
ΔT_{sub}	fluid subcooling, $\Delta T_{sub} = T_{sat} - T_f$ [°C]
t	time [s]

$\bar{u}_{HDF}$	velocity of HDFs averaged along channel length [m/s]
W	width of channel's cross section [m]
x	flow quality
x_e	thermodynamic equilibrium quality
z	streamwise coordinate [m]

Subscripts

a	denotes wall 1 or 2 (= 1 or 2)
BHM	with respect to the BHM
f	liquid; bulk fluid
g	vapor
h	heated
in	inlet to channel's heated section; inlet
net,loss	net heat loss between the BHM inlet and the FBM heated section inlet
out	outlet of channel's heated section; outlet
s	solid
sat	saturation
tc	thermocouple in heating strip
w	wall
wa	wall 1 or 2 (= *w*1 or *w*2)
z	local (along streamwise direction)

Acronyms

BHM	Bulk Heater Module
CHF	Critical Heat Flux
FBCE	Flow Boiling and Condensation Experiment
FBM	Flow Boiling Module
FIR	Fluid Integrated Rack onboard the ISS
GRC	NASA's Glenn Research Center
HDF	High-Density Front
ISS	International Space Station
LDF	Low-Density Front
MST	Mission Sequence Testing
nPFH	n-Perfluorohexane
NVG	Net Vapor Generation
ONB	Onset of Nucleate Boiling
ONBD	Onset of Nucleate Boiling Degradation

PU-BTPFL Purdue University Boiling and Two-Phase Flow Laboratory
RTD Resistance Temperature Detector

1. Introduction

1.1 Phase-Change Thermal Management Schemes for Space Applications

Two-phase thermal management systems have been identified as a critical component of future aerospace systems including high-power-density energy conversion equipment, avionics, Rankine-power-cycle-based Fission Power Systems (FPS), and onboard life support systems [1]. A broad range of gravitational fields are experienced in aerospace applications, ranging from microgravity (μg_e) to hypergravity ($>1g_e$), and hence the strength of body force acting on the fluid also varies over a broad range. This affects both the heat transfer and flow physics of boiling schemes, where liquid and vapor, possessing densities differing by several orders of magnitude, coexist.

The present work is part of a long-term endeavor by the Purdue University Boiling and Two-Phase Laboratory (PU-BTPFL) to investigate relevant two-phase thermal management schemes for adoption in space applications. Fundamental research since the mid-1980s has led to the development of practical thermal management solutions for a broad variety of applications such as space, computer electronics, data centers, avionics, energy, laser, microwave, radar, materials processing, *etc*. The resulting expertise gained regarding numerous two-phase schemes, including capillary flows, pool boiling, falling films, flow boiling in macro-channels and mini/micro-channels, jet impingement, sprays, and hybrid cooling schemes, has yielded the following conclusions regarding their implementation in space applications [2]:

(i) Despite their passive circulation attributes, capillary devices (*e.g.*, heat pipes, capillary pumped loops, loop heat pipes) can only tackle exceedingly small power densities.

(ii) Pool boiling (*e.g.*, using thermosyphons) is very problematic in μg_e. In the absence of a body force to remove bubbles from the heated surface, the produced vapor aggregates into a few enormously sized bubbles that resist liquid replenishment, and critical heat flux (CHF) is reached at exceedingly small surface heat fluxes.

(iii) Falling-film schemes, because of reliance on gravity to drive the cooling liquid film, are inoperable in μg_e.

(iv) Jet impingement is well known for its ability to tackle remarkably high heat fluxes. However, multiple jets are required to maintain uniform surface temperatures for sensitive devices. This requires an increase in coolant flow rate, which is less desirable in space applications.

(v) Spray cooling mirrors the high-heat-flux advantages of jets but dispersing the liquid flow as droplets upon the heating surface provides better cooling uniformity with a lesser flow

rate than jets. This is one reason sprays are found in several space applications especially in fuel delivery and chill down.

(vi) Macro-channel and mini/micro-channel boiling are well suited to cooling high-heat-flux surfaces in space applications and will be investigated further in the present study. Preferable attributes include small weight and volume requirements (often using *cold plates*), and ability to tackle high-heat-fluxes. This is due to reliance on flow inertia, rather than body force, to flush bubbles away from heated surfaces and maintain supply of fresh liquid for further boiling.

1.2 Effects of Body Force on Flow Boiling

Numerous studies have investigated the influence of reduced gravity on flow boiling. This has primarily been done during short periods of μg_e achieved via drop towers (*e.g.*, Ma and Chung [3]), sounding/suborbital/ballistic rockets, and parabolic flights (*e.g.*, Iceri *et al*. [4]). While providing cost-effective μg_e data, each method has its drawbacks. For instance, the μg_e period during free fall in a drop tower is too short to reach steady state for most experiments [5]. This is less prevalent on sounding rockets and parabolic flights, but small fluctuations in the μg_e level (termed *g-jitter*) [6] degrade the quality of μg_e and artificially enhance heat transfer [7].

Steady, long periods of μg_e can be achieved onboard shuttles/recoverable satellites [8–11], and the International Space Station (ISS) [7,12,13], as has been demonstrated for pool boiling experiments. Researchers collaborating with the Japanese Aerospace eXploration Agency (JAXA) performed flow boiling experiments onboard the ISS during 2017 – 2019. Thus far, their research objectives [14] and heat loss estimates [15,16] have been reported. Plans for future flow boiling experiments onboard the ISS have been outlined by several research groups in conjunction with the European Space Agency (ESA). The first [17], aims to observe bubble growth and behavior, study the effects of electric fields, shear flow, and binary mixtures on single bubbles, and the interactions between bubbles. The other [18], aims to study flow boiling of nPFH in a 6-mm-diameter copper tube, at much lower mass velocities of 20 – 150 kg/m^{2}s than the present study. A more detailed literature review of boiling experiments in μg_e is provided in the authors' prior study [19].

1.3 Flow Boiling with Saturated Inlet

Subcooled liquid is the preferred inlet state for thermal management applications due to its potential to enhance both heat transfer and CHF. However, in certain applications, such as the evaporator in vapor-compression heat pump and refrigeration cycles, fluid enters as a saturated two-phase mixture. Furthermore, extensive thermal management systems consist of a single flow loop to manage numerous heat sources connected in series. As fluid absorbs heat along the loop,

it will reach saturation, and heat sources downstream will endure saturated two-phase inlet conditions. Flow patterns and heat transfer performance are heavily dependent on the channel's inlet conditions, especially inlet void fraction.

In contrast to pure liquid inlet, fewer studies have investigated flow boiling heat transfer with two-phase inlet and reported different trends of heat transfer with respect to inlet quality. Sharon *et al.* [20] studied flow boiling heat transfer of water in a concentric annular gap for both subcooled and saturated inlet conditions. Their experiments covered a pressure range of 0.13 – 0.7 MPa, mass velocities of 330 and 570 kg/m^{2}s, and an inlet quality range of -0.05 – 0.15 for two different annular gap sizes of 0.191 and 0.317 mm. With saturated inlet conditions, vapor entered the gap as slugs at relatively high qualities of ~0.14 to the larger gap and at inlet qualities barely above 0 to the smaller gap, and wall temperature oscillated with larger amplitudes at higher wall superheats. At low pressures and flow rates, increasing inlet quality deteriorated heat transfer due to higher void fractions within the gap, and this phenomenon is more pronounced for smaller gaps. On the other hand, at a moderate pressure of 0.3 MPa in larger gaps, increasing inlet quality enhances heat transfer for low wall superheats (< 12°C), and at a certain critical superheat, heat transfer deteriorates due to increased void fractions in the gap resulting in intermittent and partial dryout. This critical heat superheat decreases upon increasing inlet quality.

A prior PU-BPTFL effort, Kharangate *et al.* [21] investigated flow boiling of FC-72 with two-phase inlet in a rectangular channel of cross-section of 2.5 × 5.0 mm^2 , length of 114.6 mm, and heated along either one or two opposite walls. Experiments were performed in vertical upflow, vertical downflow, and horizontal flow orientations in 1g_e to analyze the effects of gravity on flow boiling with two-phase inlet. Their experimental conditions include inlet qualities of 0.00 – 0.69, mass velocities of 183.5 – 2030.3 kg/m^{2}s, and inlet pressures of 109.7 – 191.8 kPa. Inconsistent trends with respect to increasing inlet quality were caused by the conflicting effects of increased acceleration and quality of the flow. This was most pronounced at low flow rates during horizontal flow with single-sided heating, which resulted in stratified flow and asymmetrical average heat transfer coefficients between the top and bottom walls. At mass velocities higher than ~800 kg/m^{2}s, greater inertia results in better agreement of average heat transfer coefficient between top and bottom wall heating, and by mitigating the effects of gravity, the results converged for all orientations. At high inlet qualities and double-sided heating, the effects of gravity were less pronounced than at low flow rates and single-sided heating.

The influence of surface wettability on flow boiling of deionized water in a rectangular micro-channel was analyzed by Li *et al.* [22] for relatively low inlet qualities of 0.03 – 0.10. Two boiling surfaces were compared: bare silicon wafer and silicon wafer deposited with 100-nm silicon dioxide. The experimental conditions were mass velocity of 120, 240, 360 kg/m^{2}s, heat flux of 4 – 20 W/cm^2, and inlet gage pressure of 0.3 – 11.7 kPa. As inlet vapor quality increased,

heat transfer severely degraded for their bare (hydrophilic) surface due to increased void fraction and resulting longer durations of intermittent dryout. On the other hand, heat transfer remained relatively constant for the superhydrophilic surface due to a more consistent and uniform distribution of the annular liquid film atop the superhydrophilic surface.

Flow boiling experiments of deionized water in a rectangular channel with a downward-facing heater at low mass velocities of 110 – 288 kg/m^{2}s, low inlet qualities of 0.003 – 0.036 (a very small range), and different channel orientations of 15 – 90° were performed by Gong *et al.* [23]. Within the ranges tested, heat transfer coefficient increased with increasing quality, especially at low heat fluxes. This dependence weakens as heat flux is increased. At all operating conditions for flow orientations greater than 60° to the horizontal, bubble motion is governed by both inertia and buoyancy, resulting in greater heat transfer coefficient than the more-horizontal orientations.

Huang *et al.* [24] examined flow boiling of ammonia with both near-saturated (inlet subcooling of 0 – 0.5°C) and two-phase (inlet quality of 0 – 0.01) inlet conditions to a radial micro-pin-fin heat sink with an emphasis on cooling down hotspots. Their experiments covered mass velocities of 34 – 182 kg/m^{2}s, heat fluxes of 752 – 1397 W/cm^2, and saturation temperatures of 26 and 30°C. They investigated the effects of these parameters on heat transfer performance. Two-phase inlets suffered from deteriorated heat transfer performance compared to near-saturated inlets.

To the best of the authors' knowledge, no μg_e flow boiling studies exist for two-phase inlet conditions, and this will be the focus of the present study.

1.4 Flow Boiling and Condensation Experiment (FBCE)

The *Flow Boiling and Condensation Experiment* (FBCE) is a collaborative effort between researchers at PU-BTPFL and the NASA Glenn Research Center (GRC) to study gravitational effects on two-phase flows, culminating in long-duration μg_e experiments onboard the ISS. Over the years, experiments to analyze gravitational effects on flow boiling and condensation have increased in complexity and reliability. Initial experiments consisted of flow boiling with subcooled inlet at different orientations in Earth gravity (*e.g.*, [25]) to isolate the components of gravity; similar work was later done for flow boiling with two-phase inlet [21]. Preliminary short-duration μg_e experiments were performed via a parabolic flight for flow boiling with subcooled inlet [26], but not for two-phase inlet. These experiments provided the expertise required to design the final FBCE system for the ISS.

FBCE consists of a single main flow loop, which is used for both flow boiling and condensation experiments by interchanging the test module. Either the Flow Boiling Module (FBM) or a condensation module can be connected to the common FBCE system. Prior to

launching to the ISS, the final FBCE system, equipped with the FBM, underwent Mission Sequence Testing (MST) in early 2021, which was a set of flow boiling experiments conducted in the vertical upflow orientation in Earth gravity. The MST experiments were performed for a subset of the experimental matrix planned for the ISS, and detailed results regarding subcooled inlet and saturated two-phase inlet are respectively presented in [27,28] and [29]. Consolidated databases formed from all pre-ISS FBCE experiments led to the development of new correlations for both subcooled flow boiling heat transfer in [30] and CHF in [31] for broad ranges of operating parameters, heating configurations, and gravitational fields.

In August 2021, the FBCE system along with the FBM was launched to the ISS in discrete modules and installed into the Fluid Integrated Rack (FIR) by astronauts. A photograph after complete installation of the FBCE modules into the FIR is shown in Fig. 1 with key components labeled. After passing several safety checks, a multitude of flow boiling experiments were performed between February 2022 and July 2022, which yielded a μg_e database encompassing a broad range of operating parameters for two heating configurations. Thus far, the effects of various parameters on heat transfer and interfacial flow physics have been analyzed for flow boiling with subcooled inlet conditions with single [19] and two, opposite [32] heated walls. Analysis of CHF for subcooled inlet including the trigger mechanism, parametric trends, and assessment of predictive tools has been done in [33].

At this juncture, the FBCE system is configured to run μg_e flow boiling experiments with two-phase inlet to address the absence of such experimental data and knowledge in the literature, despite their importance for space applications.

Flow Boiling and Condensation Experiment (FBCE)
Installed into the ISS's Fluid Integrated Rack

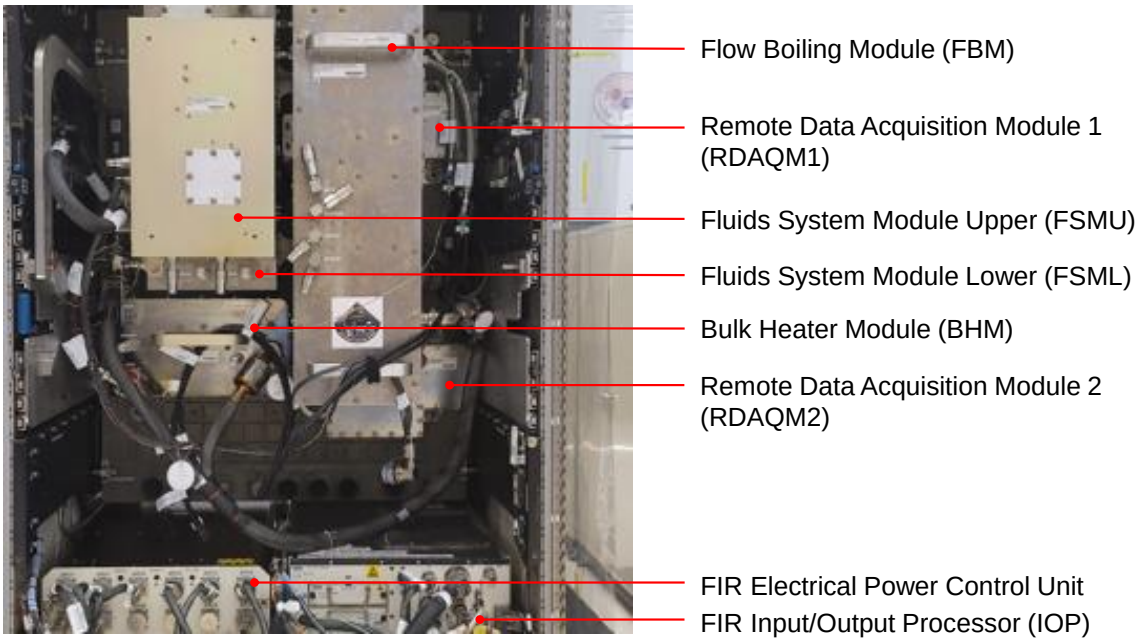

Fig. 1 Photograph of FBCE modules installed into the Fluid Integrated Rack on the ISS.

1.4 Objectives of Study

This study is aimed at investigating the heat transfer and flow physics of μg_e flow boiling with two-phase (liquid-vapor mixture) inlet conditions to a rectangular channel with both single- and double-sided heating. Mass velocity and inlet quality are varied over broad ranges at two different inlet pressures, and for each set of inlet conditions, heat flux is incremented from a minimum until CHF occurs. A large database is amassed for two-phase inlet in μg_e for the first time in the literature with experiments conducted for several different combinations of operating conditions within the limits of the experimental system. Flow physics and heat transfer characteristics are investigated in an elaborate manner. Flow patterns are presented to assess the periodic transient flow patterns within the channel and the near-wall interfacial behavior. Heat transfer performance is assessed by a combination of flow boiling curves, streamwise profiles of wall temperature and heat transfer coefficient, and parametric curves of local and average heat transfer coefficients. Parametric effects on various aspects are elucidated.

2. Experimental Methods

Based on the recommendations of a past NASA-funded study on potential fluids for space applications [34], n-Perfluorohexane (nPFH, C_6F_{14}) is chosen for the present experiments for its remarkable thermophysical properties aiding thermal management in space missions. For the most complete writeup of experimental methods, the reader is referred to the authors' prior article on subcooled inlet [19]; only the most important aspects and differences are described here.

2.1 Two-Phase Flow Loop

A schematic of the FBCE system's closed flow loop, showing the components and instrumentation paramount for the present experiments, is shown in Fig. 2. Subcooled liquid nPFH is positively displaced by a gear pump, and it flows through a Coriolis flow meter and a filter in succession. Liquid nPFH then enters a preheater, called the Bulk Heater Module (BHM), which is equipped with a set of heaters and boils the liquid to a two-phase mixture of desired quality. The two-phase nPFH mixture enters the test module, called the Flow Boiling Module (FBM), where more heat is added to the nPFH to increase its quality. This higher-quality nPFH enters a nPFH-to-water heat exchanger, where it condenses and cools down to a subcooled liquid, which then enters a static mixer, where it attains thermodynamic equilibrium in the subcooled state.

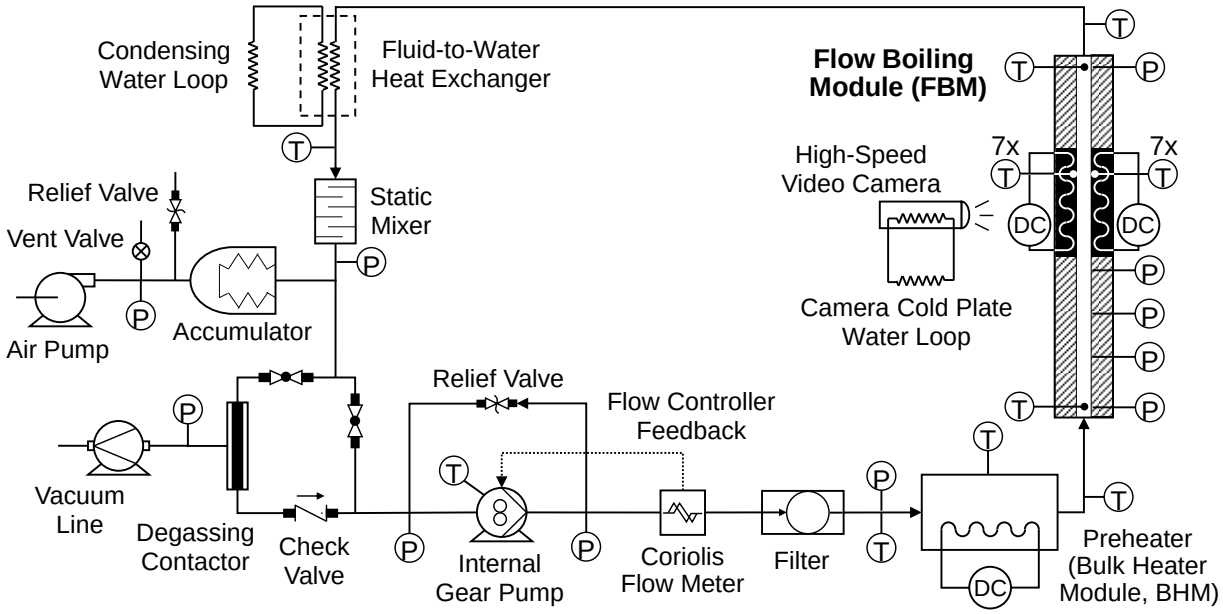

Fig. 2 Schematic of the FBCE system's two-phase flow loop showing the components and instrumentation paramount for flow boiling experiments. Adapted from the authors' prior study [19].

The majority of the nPFH is stored in an accumulator connected to the main flow loop downstream of the static mixer. The accumulator helps both set a reference pressure point in the loop and reduce/eliminate two-phase flow instabilities during experimentation [35] by varying the pressure and volume of air via an air pump and vent valve assembly, while isolating the nPFH and air via inbuilt bellows. The nPFH is ensured to be free of non-condensable gases by having a degassing contactor on a flow path parallel to the main flow loop between the accumulator's connection point and the pump and degassing it at regular intervals prior to experimentation. The degassing contactor contains a semi-permeable membrane and degassing involves applying vacuum on one side of the membrane, while nPFH is flowed through the other side at extremely low flow rates.

2.2 Flow Boiling Module (FBM)

Schematics of the overall construction of the FBM, construction of heating strips, and designation of heated walls and local wall temperatures are respectively illustrated in Figs. 3(a-c). The FBM is primarily constructed from three polycarbonate plates stacked together in the order of respective thicknesses 25.15, 5.0, and 25.15 mm (see Fig. 3(a)). The middle plate contains the flow channel in the form of a milled rectangular slot of 5.0 mm depth and 2.5 mm width, yielding a 3.33 mm hydraulic diameter. Two oxygen-free heating strips of 114.6 mm length, 15.5 mm width, and 1.04 mm thickness are provided on either side of the flow channel. The heating strips are designed to be wider than the flow channel to provide practical provision for O-ring sealing.

The bottom schematic in Fig. 3(a) shows the longitudinal design of the FBM, with the overall flow channel consisting of a 327.7 mm upstream development length, 114.6 mm middle heated length, and 60.7 mm downstream exit length. Only the heated section is of importance to this study. The flow enters and exits the FBM at 90° angles to the flow channel, but the provision of the development and exit lengths, in addition to a honeycomb flow straightener close to the FBM inlet, ensures the flow streamlines within the heated section are parallel to the channel walls.

The schematic in Fig. 3(b) shows the detailed construction of each heating strip, which has a flat heating surface in contact with the nPFH, and on the opposite side, a set of six thick-film resistive heaters within a milled-out depression. This results in the distance between the heated wall and the heaters to be minimal at 0.56 mm. A 0.9 mm gap is provided between successive heaters so thermocouples can contact the strip. This strip design, with a minimal heat capacity, enables quick temperature response and accurate CHF measurement [26,36]. The heaters are electrically wired in a way they can be independently powered for both single- and double-sided heating experiments, and the maximum power for each strip is 175 W. The FBM's key dimensions are reported in Table 1.

Table 1 Key dimensions of the FBM.

Upstream development length, L_d	327.7 mm
Heated length, L_h	114.6 mm
Downstream exit length, L_e	60.7 mm
Thermocouple locations (7) from heated section start, z_{tc}	5.4, 22.7, 40.0, 57.3, 74.6, 91.9, 109.2 mm
Channel height (unheated), H	5.0 mm
Channel width (heated), W	2.5 mm
Hydraulic diameter, D_h	3.33 mm

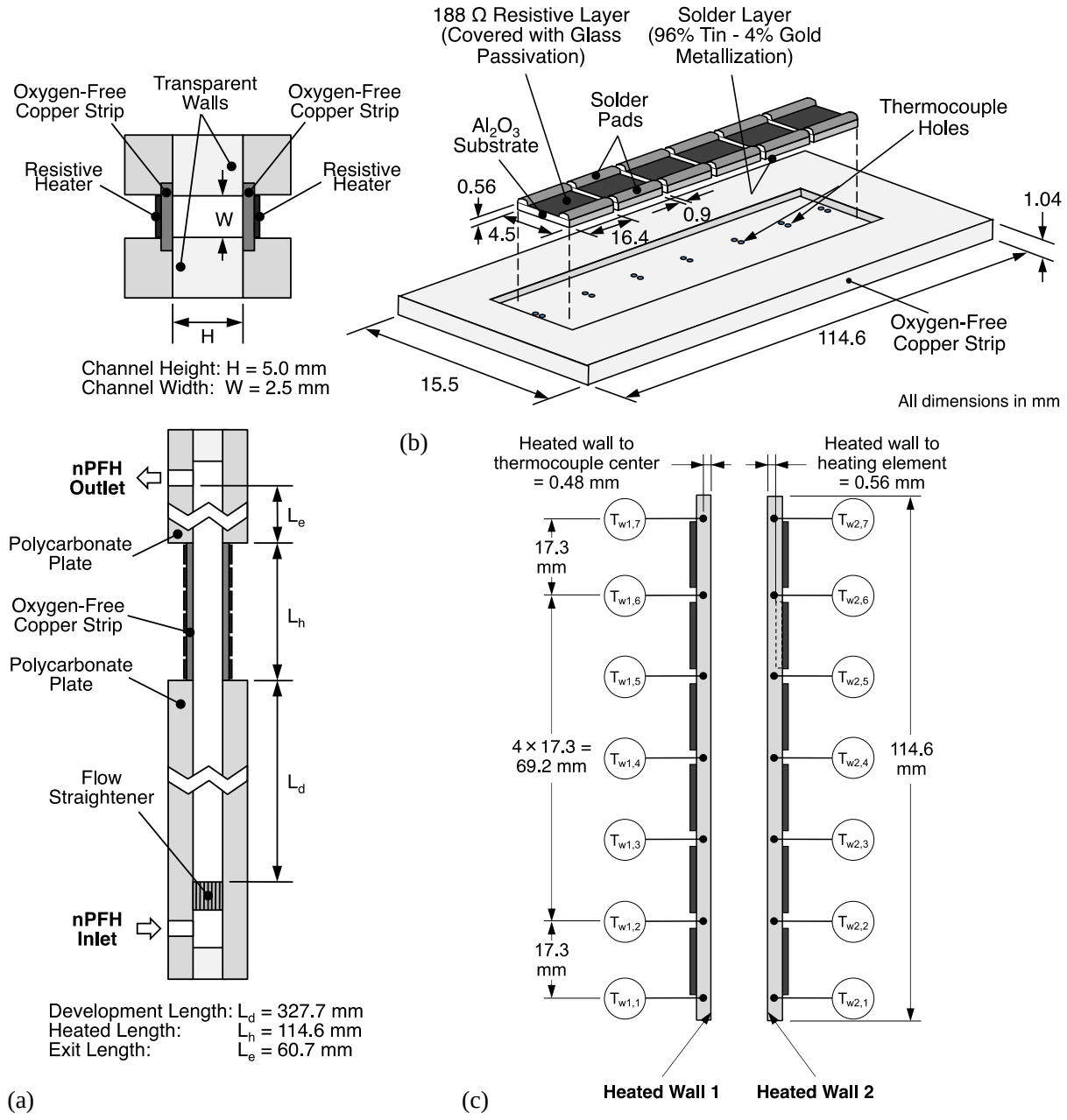

Fig. 3 Schematics of (a) overall construction of Flow Boiling Module (FBM), (b) construction of heating strips, and (c) designation of heated walls and local wall temperatures. Adapted from the authors' prior study [19].

2.3 Flow Visualization System, Data Measurement Instrumentation, and Safety Precautions

Flow visualization of two-phase features within the FBM's heated section is done using a high-speed video camera pointed at one of the two transparent unheated walls, while the opposite wall is backlit with light emitting diodes. Images are continuously captured onto an image buffer during experiments, but only the latest 1 second is recorded for each heat increment, except for the CHF increment, for which the latest 7 seconds are recorded. Key specifications of the captured

images include 2000-frames-per-second frame rate, 10-μs shutter speed, 2040×164-pixel resolution and ~90 μm spatial resolution (deduced using Ronchi ruling). The captured images are uniformly post-processed to enable easier discerning of complex flow features.

As shown in Fig. 2, local pressure and temperature are measured at several points in the flow loop via absolute pressure transducers and thermocouples and RTDs. Local pressure within the FBM is obtained via five absolute pressure transducers, of which one each is provided close to the FBM inlet and outlet, and the other three are provided within the FBM's development length. In this study, p_{in} and p_{out} denote pressure measurements just upstream and downstream of the heated section. T_{in} and T_{out}, respectively denoting bulk fluid temperatures at the FBM inlet and outlet, are measured via type-E thermocouples extending into the flow. Local temperatures of the heating strips are measured via type-E thermocouples attached within shallow hemispherical indentations on the strip, yielding a minuscule distance of H_{tc} = 0.48 mm between the heating surface and the thermocouple tip's center. Mass flow rate of nPFH is measured via the Coriolis flow meter. The power to each heating strip is calculated from the respective voltage and current measured internally within a data acquisition system (DAQ). The measured data from all sensors are collected within two DAQs and a continuous temporal record is saved at a 5 Hz sampling rate whenever experiments are in process and 1 Hz rate whenever the FBCE system is powered on. Everything is remotely controlled via FBCE flight software. The maximum uncertainty in these data measurements is reported in Table 2.

Table 2 Maximum uncertainty in data measurements.

Data Measurement	**Maximum Uncertainty**
Temperature (thermocouples)	±0.5°C
Temperature (RTDs)	±0.5°C
Pressure	±0.7 kPa
FBM heater power	±0.3% reading
Preheater power	±0.6% reading
Mass flow rate	±0.6% reading

Some precautionary safety provisions in the FBCE system include:

(i) a secondary set of seven type-E thermocouples on each heating strip to provide hardware feedback to shut the heaters down in the event any local temperature exceeds 132°C,

(ii) thermocouples and Resistance Temperature Detectors (RTDs) within the BHM to provide feedback to shut the heaters down in the event the BHM heating surface exceeds 130°C or the BHM's outlet fluid temperature exceeds 100°C,

(iii) two relief valves across the ends of the pump to crack open in the event the differential pressure exceeds 199.95 kPa for the first valve, and to serve as a backup, 206.84 kPa for the second valve, and

(iv) a relief valve on the accumulator's air side to crack open in the event the pressure differential between the air line and ISS environment exceeds 137.90 kPa.

2.4 Experiment Procedure and Summary

The present ISS experiments for two-phase inlet (summarized in Appendix A) were remotely executed from NASA GRC over a sporadic period from February 2022 to July 2022. Each predetermined experimental case is executed by providing inputs of G, p_{in}, and $x_{e,in}$ to the FBCE software in the form of experimental parameters. After transmission to the ISS, the flow loop is given sufficient time to reach a steady state. One of the two heating strips are powered for single-sided heating, whereas both heating strips are powered for double-sided. The first twelve FBM heat increments, from a minimum level to near-CHF, are predetermined and inputted into the software. Each increment is allowed for a period of 120 – 180 seconds to reach a steady state before the heaters are automatically incremented to the next step. If CHF is not attained within the first twelve steps, more fine increments are automatically provided at a minimal 1.25 W to accurately capture CHF. CHF is defined to occur when at least one heating-strip temperature reaches 122°C, and the FBCE software executes a software reset of the heater power to a minimum level. The value of CHF, q''_{CHF}, lies in-between the heat increment that caused the 122°C attainment and the prior heat increment that reached steady state, so it is determined from the average of these two heat increments. Temporal variations of temperatures and heat fluxes for a typical experimental case are provided in Appendix B.

2.5 Data Processing and Experimental Ranges

The present experimental data is processed very similar to the $1g_e$ MST experiments [29]. The temporal records are scrutinized, and the last 20-s period of each heat increment is averaged to obtain steady-state datapoints. The thermophysical properties of nPFH required for further processing are obtained from the NIST-REFPROP database [37]. The fluid enthalpy at the BHM's inlet is directly evaluated from the BHM's inlet fluid temperature, $T_{BHM,in}$, and pressure, $p_{BHM,in}$. Details on heat losses both upstream of and within the FBM are provided in Appendix C, using which the enthalpy at the FBM inlet, h_{in}, is determined. Fluid enthalpy at the FBM outlet is calculated from an energy balance over the FBM as

$$h_{out} = h_{in} + \frac{q''_w P_h L_h}{\dot{m}}, \tag{1}$$

where P_h is heated perimeter and is equal to channel width, W, for single-sided heating, and $2W$ for double-sided.

Thermodynamic equilibrium qualities at both the FBM's inlet and outlet are determined as

$$x_e = \frac{h - h_f\big|_p}{h_{fg}\big|_p}, \tag{2}$$

where h is local enthalpy and both h_f saturated liquid enthalpy and h_{fg} latent heat of vaporization are evaluated at local pressure.

The designation of local wall temperatures, as shown in Fig. 3(c), is $T_{wa,z}$, where wa is the heated wall ($w1$ or $w2$) and z the streamwise measurement location (1 upstream through 7 downstream). Each measured strip temperature, T_{tc}, is converted to T_w using

$$T_w = T_{tc} - \frac{q''_w H_{tc}}{k_s}, \tag{3}$$

a result of assuming uniform heat flux and 1-D heat conduction, where k_s is the thermal conductivity of copper. Since the fluid is saturated all along the heated length, local fluid temperature, $T_{f,z}$, is equal to the local saturation temperature, $T_{sat,z}$, which is estimated via linear interpolation between values at the inlet and outlet. Local heat transfer coefficient is defined as

$$h_{a,z} = \frac{q''_{wa}}{T_{wa,z} - T_{f,z}}, \tag{4}$$

and for $N_z = 7$ streamwise measurement locations, averaged heat transfer coefficient for the entire heated wall is determined as

$$\bar{h} = \frac{\sum_{N_z} h_{a,z} L_{h,z}}{L_h}, \tag{5}$$

where $L_{h,z}$ is the heated length of each unit cell represented by the local value, and L_h is the total heated length. Averaged wall temperature, $\overline{T_w}$, is similarly determined.

A summary of key parameters of the ISS steady-state database for flow boiling with two-phase inlet is included in Table 3 for both single- and double-sided heating. Note that this only includes the latest (final) trial of each case, and they reached CHF.

Table 3 Summary of key parameters of ISS microgravity steady-state database for two-phase inlet with single- and double-sided heating (only the latest, final trials of each case). The corresponding experiments are listed in Appendix A.

	Single-Sided Heating	**Double-Sided Heating**
Mass velocity, G	179.97 – 2400.00 kg/m^{2}s	179.36 – 2400.00 kg/m^{2}s
Mass flow rate, $\dot{m}$	2.25 – 30.00 g/s	2.24 – 30.00 g/s
Inlet pressure, p_{in}	119.56 – 178.84 kPa	120.72 – 200.44 kPa
Inlet temperature, T_{in}	64.79 – 77.84˚C	64.95 – 80.82˚C
Inlet quality, $x_{e,in}$	-0.012 – 0.868	-0.047 – 0.864

Wall heat flux, q''_w	1.78 – 38.17 W/cm^2	1.93 – 39.02 W/cm^2
Outlet pressure, p_{out}	112.71 – 167.37 kPa	112.98 – 181.19 kPa
Outlet temperature, T_{out}	58.72 – 70.32˚C	58.82 – 79.08˚C
Outlet quality, $x_{e,out}$	0.032 – 0.936	0.046 – 0.974

3. Visualization of Microgravity Flow Boiling with Two-Phase Inlet – Results and Discussion

Images of flow patterns within the FBM's heated length are presented in this section. First, image sequences at various operating conditions are presented to establish commonly observed transient flow characteristics. Subsequently, figures depicting the average flow pattern observed at different heat fluxes along the boiling curve are parametrically investigated.

A schematic representation of single- and double-sided heating configurations are shown in Figs. 4(a) and (b), respectively. All flow visualization images conform to this format wherein fluid enters from the bottom end of the channel at the specified inlet conditions. Either one wall or both walls are heated for single- and double-sided heating, respectively. For single-sided heating, the choice of heated wall has insignificant influence on boiling behavior in μg_e and has shown to yield near-identical results (refer to Appendix F and [19,32]).

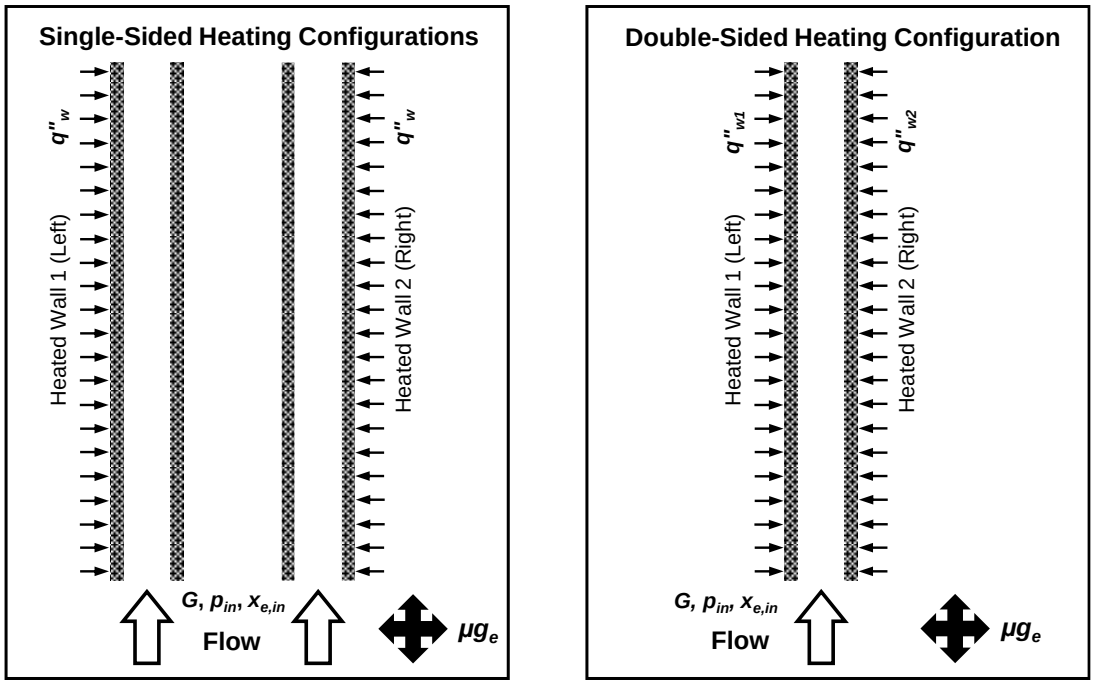

(a) (b)

Fig. 4 Schematics of (a) single- and (b) double-sided heating configurations. A liquid-vapor mixture of nPFH enters the channel at the specified mass velocity of G, inlet pressure of p_{in}, and inlet quality of $x_{e,in}$ while the walls are heated with a heat flux of q''_w. Adapted from the authors' prior study [19,32].

3.1 Near-Wall Flow Boiling Characteristics for Two-Phase Inlet

Figs. 5 and 6 highlight the near-wall phenomena which are not very apparent in subsequent images. Fig. 5 contains a representative image of transitory flow pattern entering the channel in which distinct flow structures can be identified; this is for a case that transitions to CHF. The lighter regions represent either pure liquid or pure vapor into the channel depth, while the darker regions represent liquid-vapor interfaces; differentiating between pure liquid and vapor is based on local quality, expected vapor void fraction, and associated flow physics. A central vapor core encased in annular liquid enters the channel. Boiling commences at the upstream edge and a vapor layer forms along each heated wall. A similar flow pattern is assumed to enter the channel for all other two-phase inlet cases of similar $x_{e,in}$, however, turbulent mixing introduces three dimensionality in the flow structures, complicating images. Further downstream, as the generated vapor layers gradually move toward the fast-moving vapor core and coalesce with it, interactions within the channel become less clear. Fig. 6 highlights the typical near-wall interfacial behavior in the channel's middle portion, albeit for different operating conditions to the image shown in Fig. 5. Accompanying each image is a contour of the vapor and liquid phases focused near the left-heated-wall region during single-sided heating. As the two-phase mixture passes through the channel, a thin residual liquid layer wets the heated wall. Boiling occurs within the liquid layer, gradually depleting it, as it slides along the channel.

The subsequent flow images presented in this section will focus on observable parametric trends affecting (i) the periodic transient flow patterns within the channel and (ii) the near wall interfacial behavior.

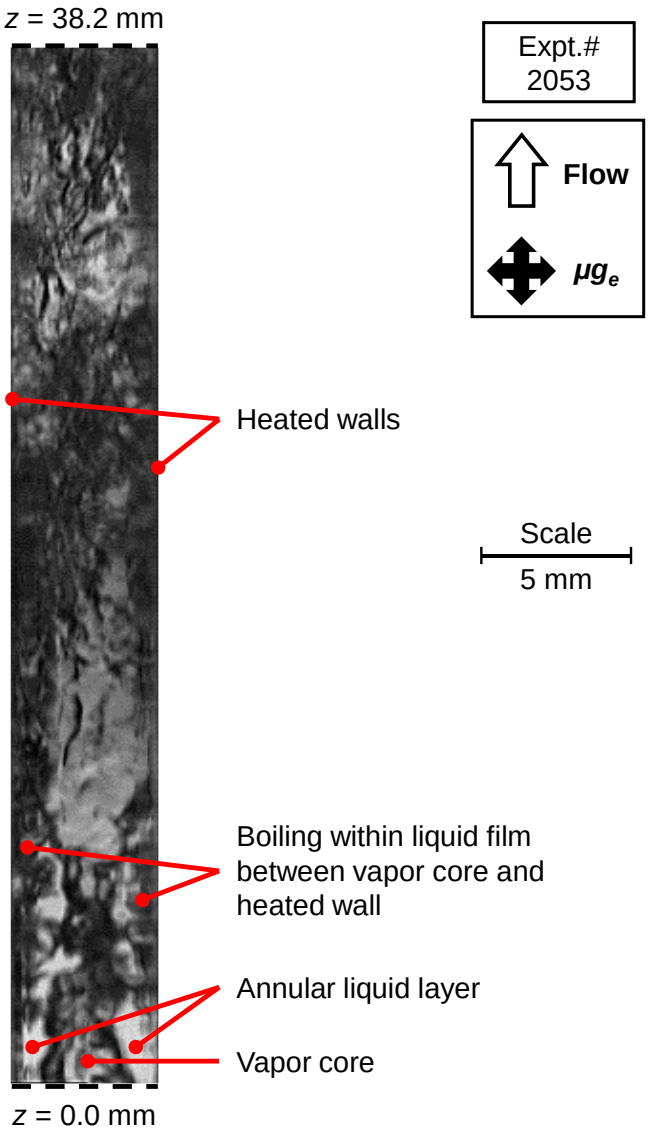

Fig. 5 Flow features in the channel's upstream region as distinct annular flow enters the channel for double-sided heating with a mass velocity of $G \approx 800$ kg/m^{2}s and inlet quality of $x_{e,in} = 0.064$. Channel width is 5 mm.

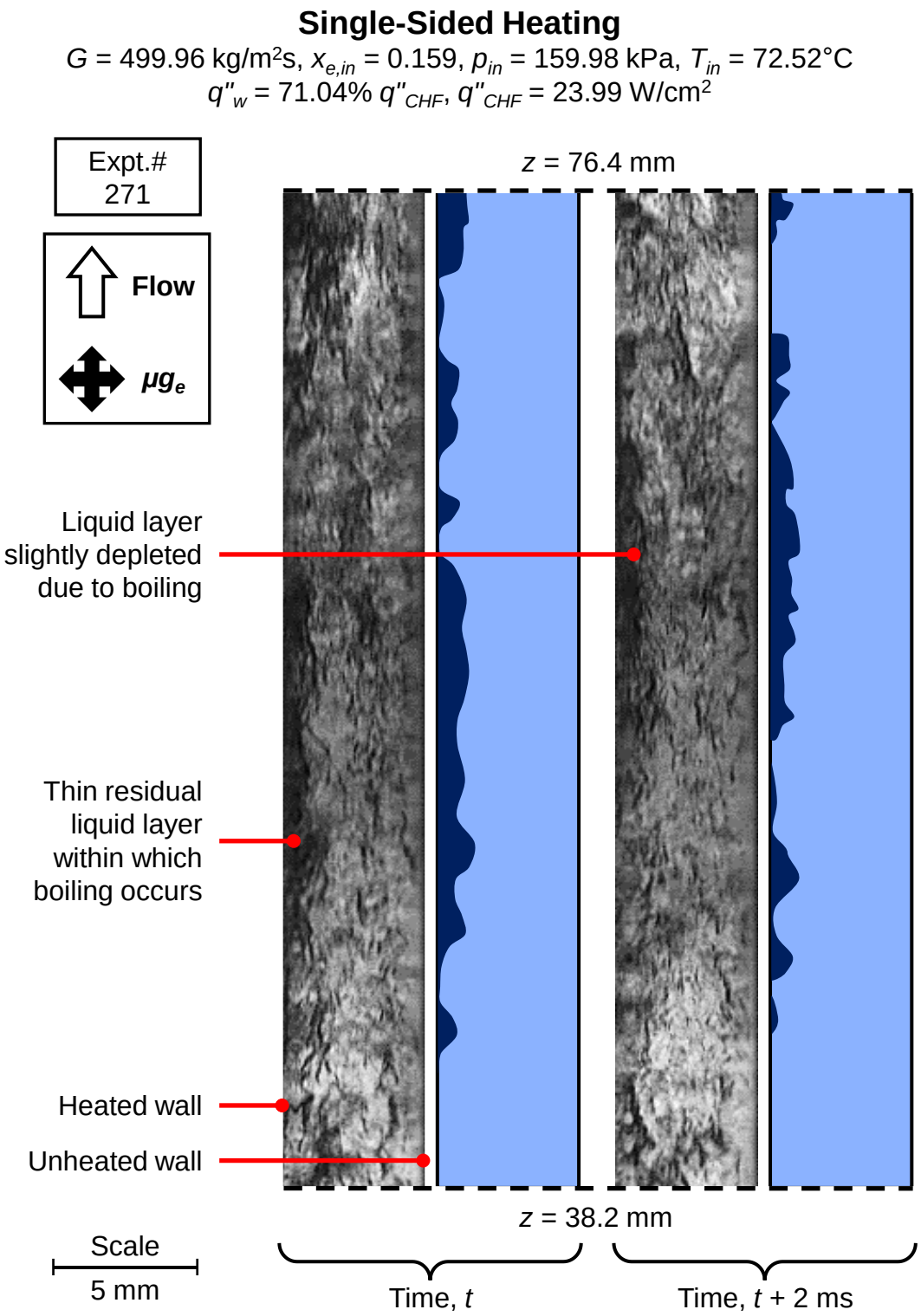

Fig. 6 Flow features in the channel's middle portion showing a liquid layer sliding along the heated wall. This is accompanied by interpreted contours of the liquid and vapor phases. Operating conditions are noted above the images. Time interval between successive images is 2 ms and channel width is 5 mm.

3.2 Image Sequences of Periodic Transient Flow Patterns

3.2.1 Image Sequences at High Inlet Quality – Effects of Heat Flux and Heating Configuration

Fig. 7 portrays images of transient flow patterns for $G \approx 500$ kg/m^{2}s, $x_{e,in} = 0.364$, and a lower heat flux of $q''_w = 31.08\%\ q''_{CHF}$ with single-sided heating of the channel's left wall. Fig. 7(a) shows flow patterns over a period of 750.0 ms with 25.0 ms of interval between consecutive images, and the respective elapsed time is listed below each image. During the first 75.0 ms, the channel is predominantly occupied by vapor, and the images are visually lighter, due to minimal interfacial features. The darker patches sparsely distributed throughout the channel are due to denser interfacial features that have greater concentrations of entrained liquid and are termed *High-Density Fronts* (HDFs). HDFs are of relatively low quality compared to the remainder of the channel, which is occupied by a vapor-abundant mixture, termed *Low-Density Fronts* (LDFs). As time progresses from 100.0 to 350.0 ms, more pronounced HDFs sporadically propagate through the channel. The HDFs temporarily become fewer between 375.0 and 475.0 ms, before a large HDF traverses at 500.0 ms. Between 525.0 and 750.0 ms, HDFs gradually become less prominent. Figs. 7(b) and (c) feature image sequences, with a finer temporal resolution of 2 ms, for low- and high-density-dominant periods, respectively. The time instants specified beneath these images correspond to those in Fig. 7(a). Each sequence begins with an HDF aligned at the inlet of the channel. Comparing Figs. 7(b) and 7(c), HDFs are larger and quicker to traverse the channel during the high-density-dominant period due to an abundance of liquid facilitating boiling, increased vapor production, and greater flow acceleration.

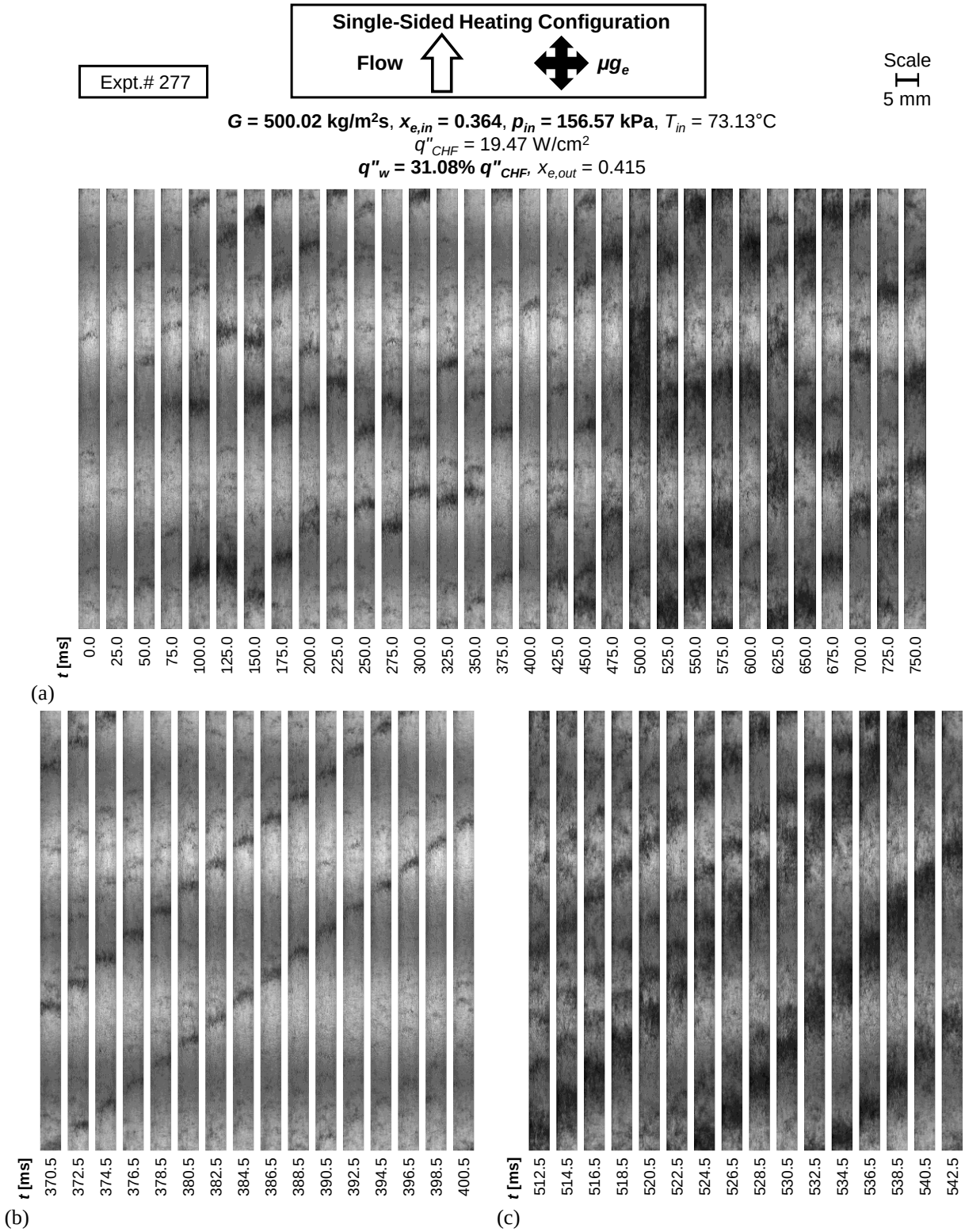

Fig. 7 Flow visualization image sequences for single-sided heating of left wall with mass velocity of $G \approx 500$ kg/m^{2}s, inlet quality of $x_{e,in} = 0.364$, and wall heat flux of $q''_w = 31.08\%$ q''_{CHF}. Shown are (a) the overall transient behavior over an extended time period (25 ms between images), (b) low-density-dominant period (2 ms between images), and (c) high-density-dominant period (2 ms between images). Channel width is 5 mm.

From the temporal flow image sequences, the time taken for a HDF to traverse the full channel length can be quantified, from which the mean velocity ($\bar{u}_{HDF}$) and mean frequency ($\bar{f}_{HDF}$) of HDFs during that period can be determined. The results of this quantification during both low- and high-density-dominant periods are presented in Table 4 for all flow image sequences presented in this paper (Figs. 7-17, D.1, D.2). Each row in the table corresponds to a figure of unique operating conditions, and the numbers for low- and high-density-dominant periods respectively correspond to subfigures (b) and (c) in each of these figures. For Fig. 7, $\bar{u}_{HDF}$ = 2.80 m/s during the low-density period, and it increases to 4.02 m/s during the high-density period. This could be attributed to the presence of more liquid within the channel during the high-density period, which results in temporally increased boiling and flow acceleration. Because each HDF is faster during this period, the frequency of HDF passage, $\bar{f}_{HDF}$, increases proportionally. Another hypothesis for this phenomenon is density wave oscillations (DWOs) due to boiling within the BHM situated upstream of the FBM; increased vapor production resulting in a low-density period within the BHM could accelerate the high-density-dominant period within the FBM, and inversely, a high-density period within the BHM could decelerate the low-density-dominant period within the FBM. These hypotheses show how the flow patterns for two-phase inlet conditions are a result of boiling within both the BHM and FBM and are very complex manifestations. The aforementioned trends hold true for all operating conditions in this paper.

Table 4 Quantification of mean velocity and mean frequency of HDFs during both low- and high-density-dominant periods for all flow image sequences presented in this paper.

			Mean Operating Conditions					Low-Density-Dominant Period		High-Density-Dominant Period	
Fig.	**Expt.#**	**G [kg/m^{2}s]**	**$x_{e,in}$**	**p_{in} [kPa]**	**Heating Config.**	**q''_w [W/cm^2]**	**$x_{e,out}$**	**$\bar{u}_{HDF}$ [m/s]**	**$\bar{f}_{HDF}$ [Hz]**	**$\bar{u}_{HDF}$ [m/s]**	**$\bar{f}_{HDF}$ [Hz]**
7	277	500.02	0.364	156.57	Single	6.05	0.415	2.80	24.39	4.02	35.09
8	277	500.02	0.364	156.57	Single	18.34	0.484	3.32	28.99	4.78	41.67
9	278	499.99	0.367	157.58	Double	5.03	0.443	2.90	25.32	4.49	39.22
10	278	499.99	0.367	157.58	Double	17.55	0.580	3.02	26.32	4.58	40.00
11	271	499.96	0.159	159.98	Single	5.71	0.207	2.70	23.53	4.32	37.74
12	271	499.96	0.159	159.98	Single	22.57	0.293	2.76	24.10	3.70	32.26
D.1	2078	499.95	0.175	163.55	Double	5.74	0.260	2.67	23.26	5.21	45.45
D.2	2078	499.95	0.175	163.55	Double	21.98	0.434	3.10	27.03	4.58	40.00
13	2061	499.95	0.100	162.68	Double	21.16	0.348	2.34	20.41	4.78	41.67
14	2079	650.44	0.100	163.65	Double	21.58	0.298	3.58	31.25	5.21	45.45
15	270	790.41	0.108	131.49	Double	23.54	0.290	3.82	33.33	5.33	46.51
16	2055	1599.93	0.124	172.95	Double	21.04	0.225	7.39	64.52	8.82	76.92
17	2087	650.44	0.094	134.05	Double	21.82	0.294	3.47	30.30	5.88	51.28

Fig. 8 depicts image sequences for the same experimental case as Fig. 7 but at a higher heat flux of q''_w = 94.23% q''_{CHF}. A high-density-dominant period exists at the beginning of Fig. 8(a), from 0 to 50 ms, and HDFs gradually fade thereafter. Comparing the low-density-dominant period in Fig. 8(b) to Fig. 7(b), HDFs are quicker in traversing the channel at the higher heat flux, evident from the HDF velocity increasing from $\bar{u}_{HDF}$ = 2.80 to 3.32 m/s. A similar phenomenon occurs during the high-density-dominant periods at low and high heat fluxes, respectively in Figs. 7(c) and 8(c), and HDFs become lighter as they traverse the channel at the higher heat flux due to more rapid boiling, which again results in increased HDF velocity from $\bar{u}_{HDF}$ = 4.02 to 4.78 m/s.

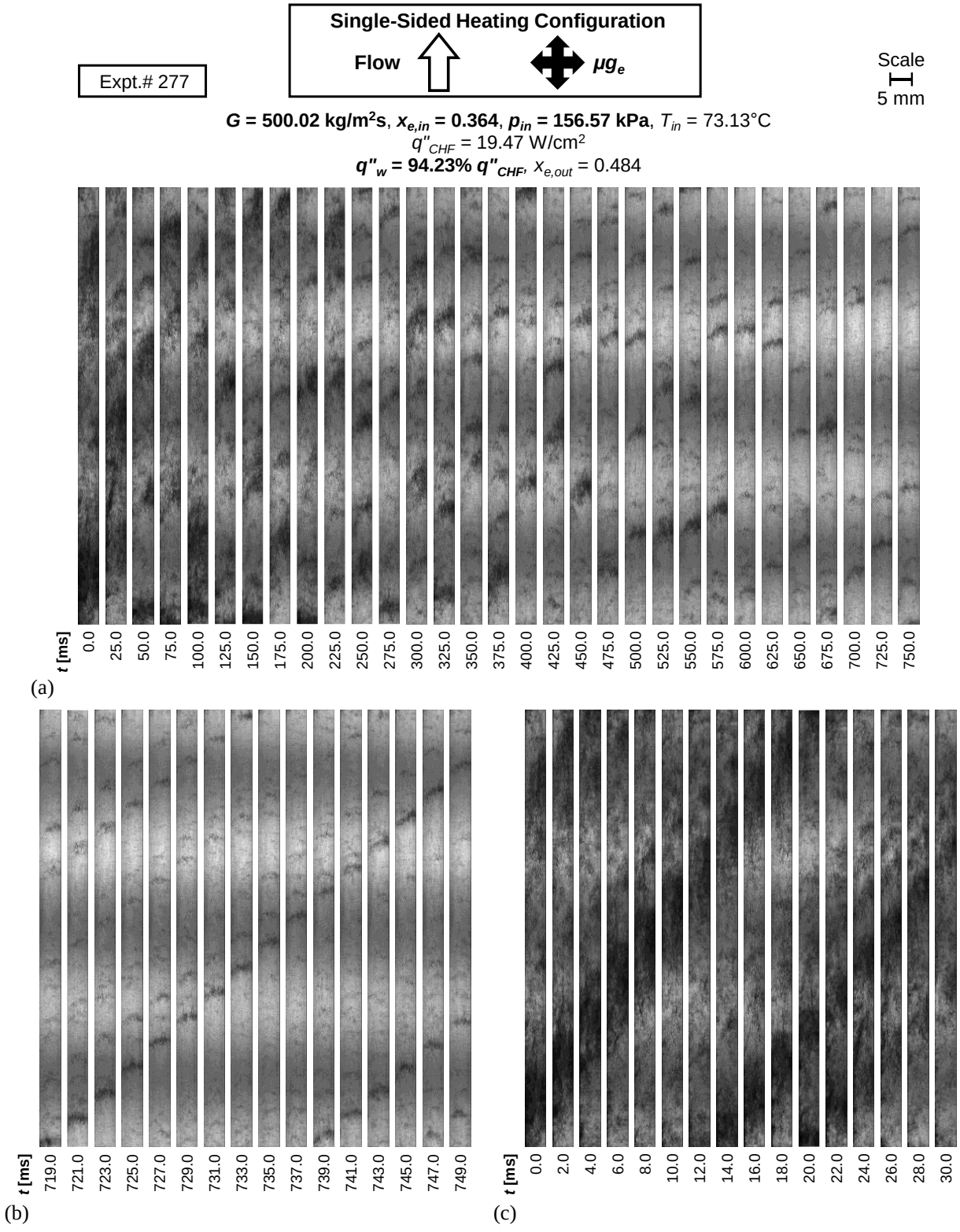

Fig. 8 Flow visualization image sequences for single-sided heating of left wall with mass velocity of $G \approx 500$ kg/m^{2}s, inlet quality of $x_{e,in} = 0.364$, and wall heat flux of $q''_w = 94.23\%$ q''_{CHF}. Shown are (a) the overall transient behavior over an extended time period (25 ms between images), (b) low-density-dominant period (2 ms between images), and (c) high-density-dominant period (2 ms between images). Channel width is 5 mm.

Sequential images with similar operating conditions of $G \approx 500$ kg/m^{2}s, $x_{e,in} = 0.367$, but double-sided heating at $q''_w = 27.15$ and 94.63% q''_{CHF} are respectively shown in Figs. 9 and 10. Due to the abundance of vapor, differences between the flow patterns for single- and double-sided heating at both heat fluxes are subtle, even during the high-density-dominant periods. However, compared to single-sided heating, the HDFs fade more quickly as they pass through the channel in double-sided heating, due to twice the amount of heat added to the fluid for similar heat fluxes. The only trend that can be ascertained by comparing the quantified velocities for single- versus double-sided heating in Table 4 is the increased HDF acceleration during transition from the low- to high-density periods. For example, during single-sided heating in Figs. 7 and 8, $\bar{u}_{HDF}$ increases by 1.22 and 1.46 m/s at $q''_w = 6.05$ and 18.34 W/cm^2, respectively, whereas during double-sided heating in Figs. 9 and 10, $\bar{u}_{HDF}$ increases by 1.59 and 1.56 m/s for similar operating conditions.

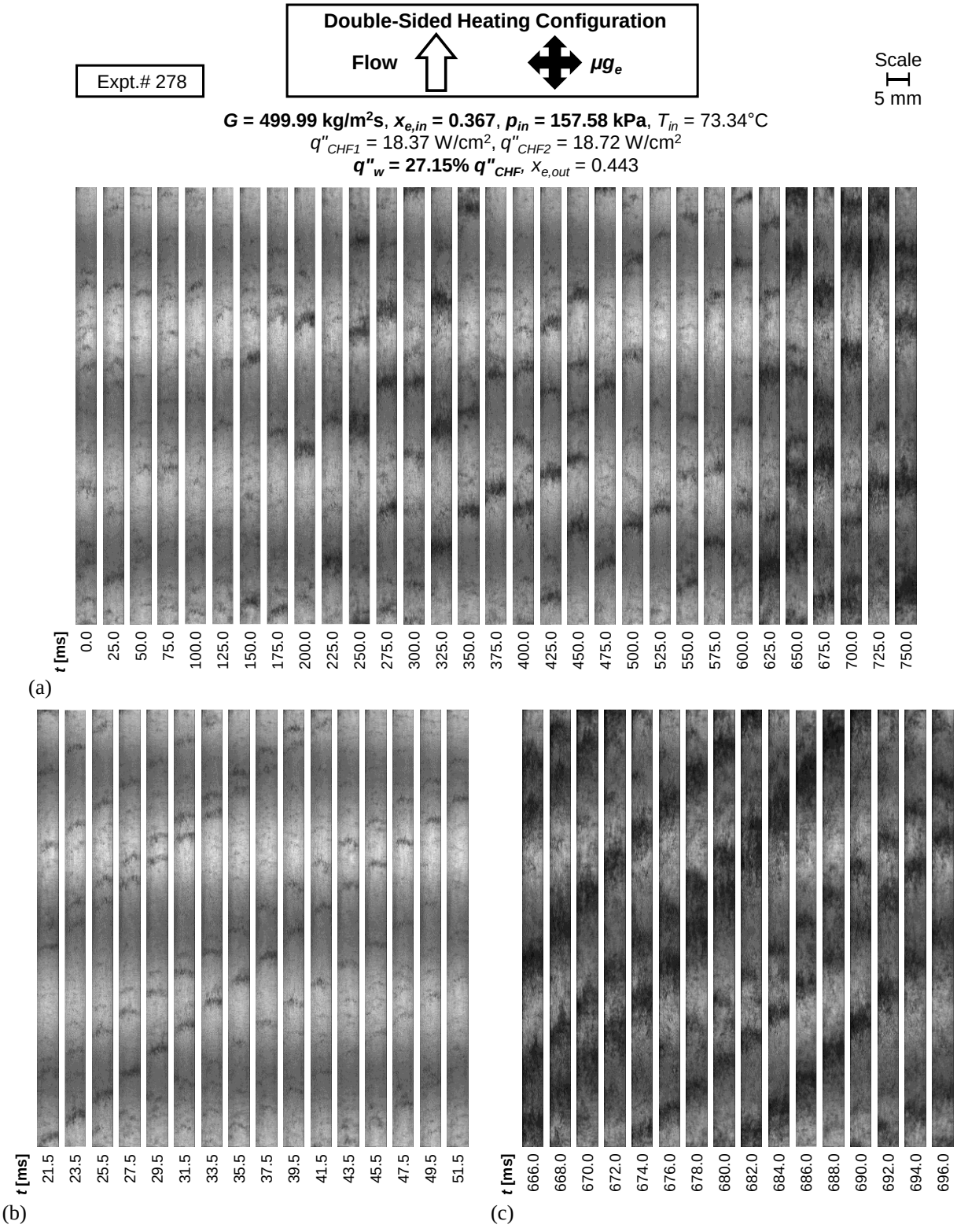

Fig. 9 Flow visualization image sequences for double-sided heating with mass velocity of $G \approx$ 500 kg/m^{2}s, inlet quality of $x_{e,in}$ = 0.367, and wall heat flux of q''_w = 27.15% q''_{CHF}. Shown are (a) the overall transient behavior over an extended time period (25 ms between images), (b) low-density-dominant period (2 ms between images), and (c) high-density-dominant period (2 ms between images). Channel width is 5 mm.

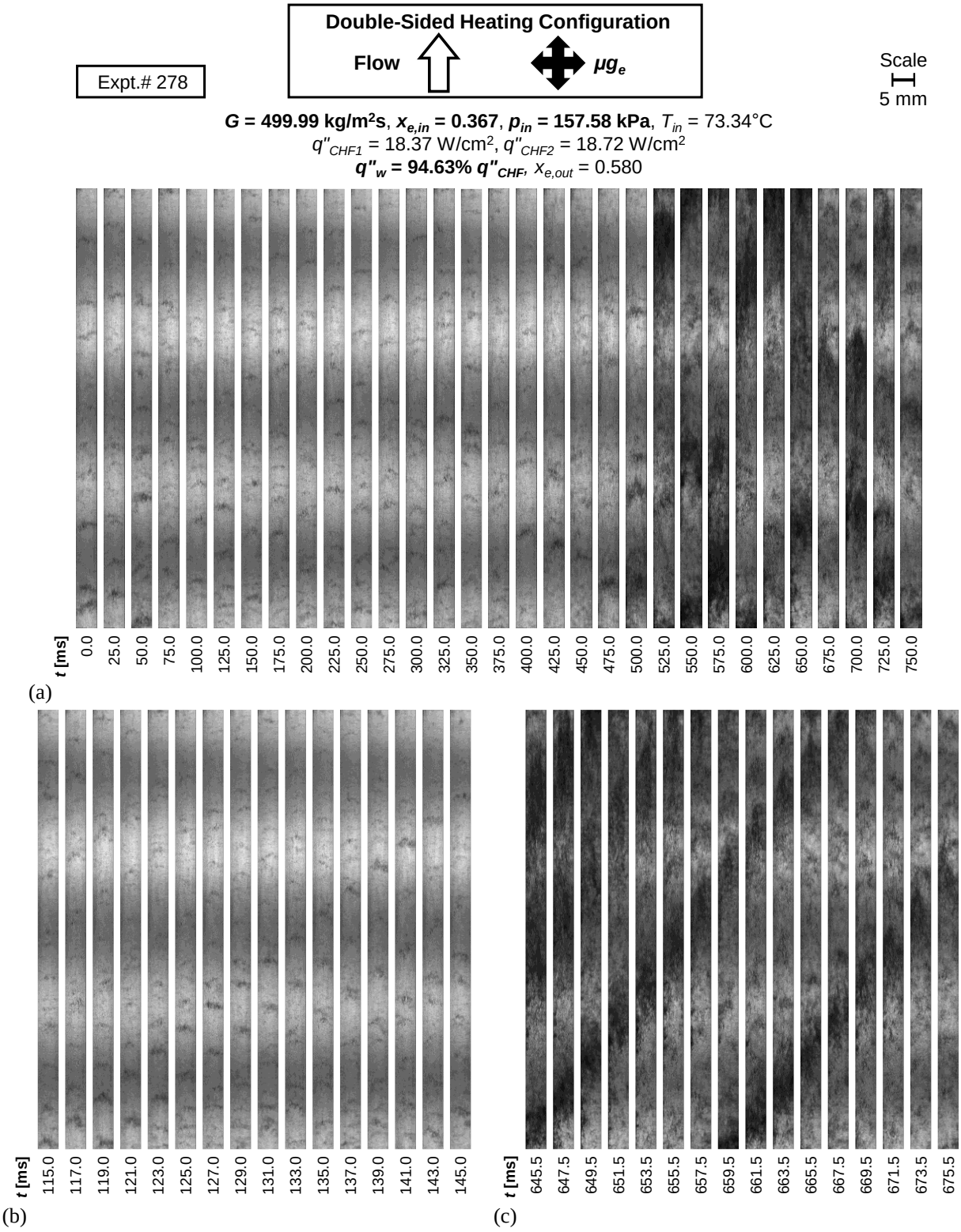

Fig. 10 Flow visualization image sequences for double-sided heating with mass velocity of $G \approx$ 500 kg/m²s, inlet quality of $x_{e,in}$ = 0.367, and wall heat flux of q''_w = 94.63% q''_{CHF}. Shown are (a) the overall transient behavior over an extended time period (25 ms between images), (b) low-density-dominant period (2 ms between images), and (c) high-density-dominant period (2 ms between images). Channel width is 5 mm.

3.2.2 Image Sequences at Low Inlet Quality – Effects of Inlet Quality and Heat Flux

Fig. 11 depicts image sequences for left wall heating with $G \approx 500$ kg/m^{2}s, $q''_w = 23.80\%\ q''_{CHF}$, and a lower $x_{e,in} = 0.159$. Throughout the extended sequence in Fig. 11(a), the channel contains more liquid and is darker compared to Figs. 7-10 at higher $x_{e,in}$. From 175.0 to 250.0 ms, the channel is almost completely devoid of HDFs, until a large HDF enters the channel at 300.0 ms. Within the low-density-dominant period in Fig. 11(b), the traversing HDFs are more pronounced than at the higher $x_{e,in}$ of Fig. 7(b). As HDFs pass during the high-density period in Fig. 11(c), a liquid layer clearly coats the walls due to shear. Boiling occurs within this liquid layer along the heated left wall, perturbing the interface as it traverses the channel. This is clearly seen as a darker region next to the heated left wall and lighter region next to the unheated right wall (see Fig. 6 for an enlarged representative view). The liquid layer passes through the channel, and a new HDF enters the channel at 349.0 ms, rewetting the wall. Fig. 12 shows flow sequences for the same experimental case, but at a higher heat flux of $q''_w = 94.08\%\ q''_{CHF}$. Similar to the comparison of low and high heat fluxes at the higher $x_{e,in}$, differences are very subtle during the low-density period. During the high-density period shown in Fig. 12(c), the liquid layer coating the heated wall is not sustained through the entire channel at higher heat fluxes. Approaching CHF, the interface of the liquid layer that follows the HDF entering the channel is clearly observed upstream along the left wall at 129.0 ms; this is marked in Fig. 12(c) with red arrowheads. As time progresses, it follows the HDF downstream, grows further from the wall as boiling occurs, and lightens until it completely evaporates by 143.0 ms. Images for double-sided heating at similar operating conditions are presented in Appendix D to validate the effects of heating configuration.

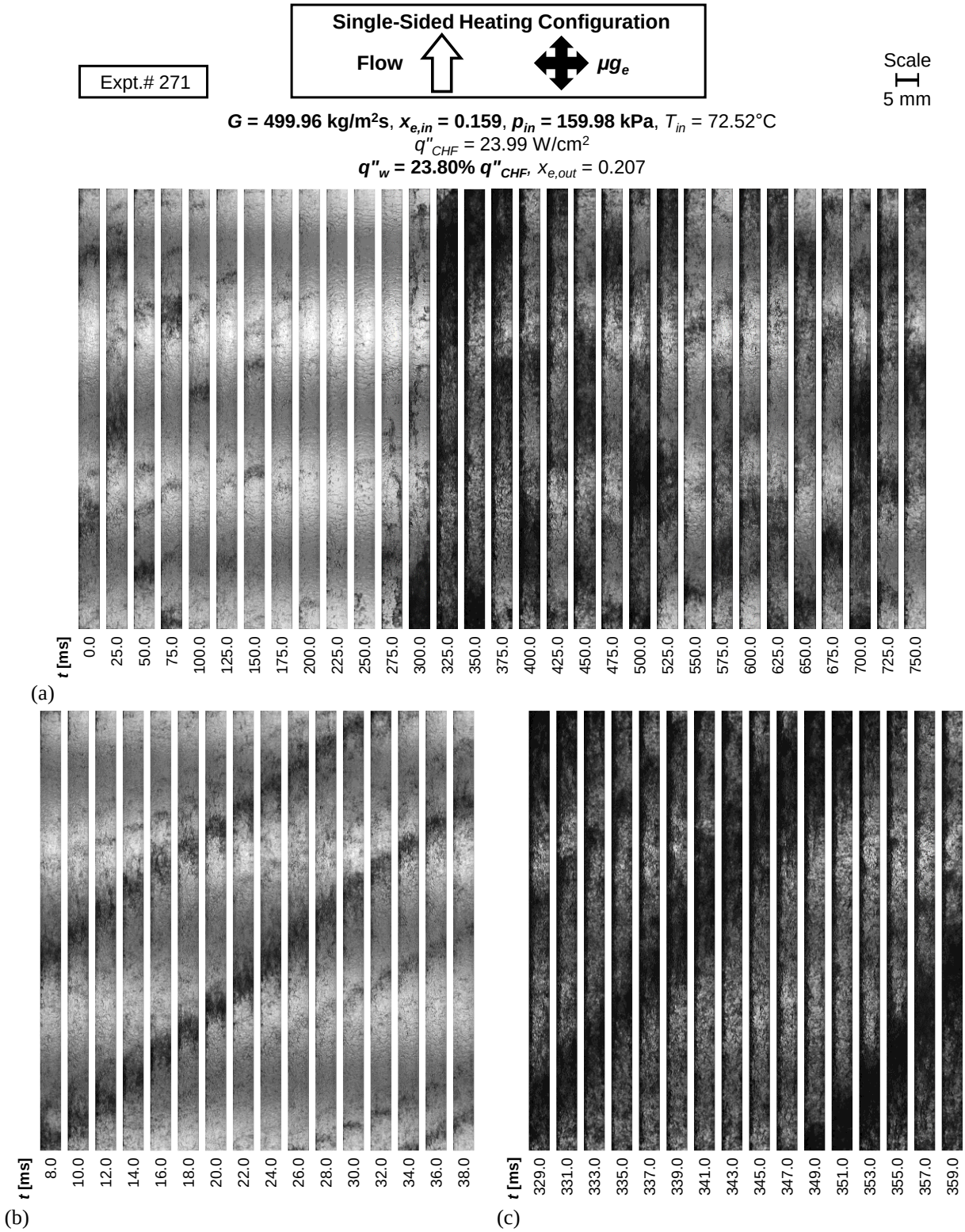

Fig. 11 Flow visualization image sequences for single-sided heating of left wall with mass velocity of $G \approx 500$ kg/m^{2}s, inlet quality of $x_{e,in} = 0.159$, and wall heat flux of $q''_w = 23.80\%$ q''_{CHF}. Shown are (a) the overall transient behavior over an extended time period (25 ms between images), (b) low-density-dominant period (2 ms between images), and (c) high-density-dominant period (2 ms between images). Channel width is 5 mm.

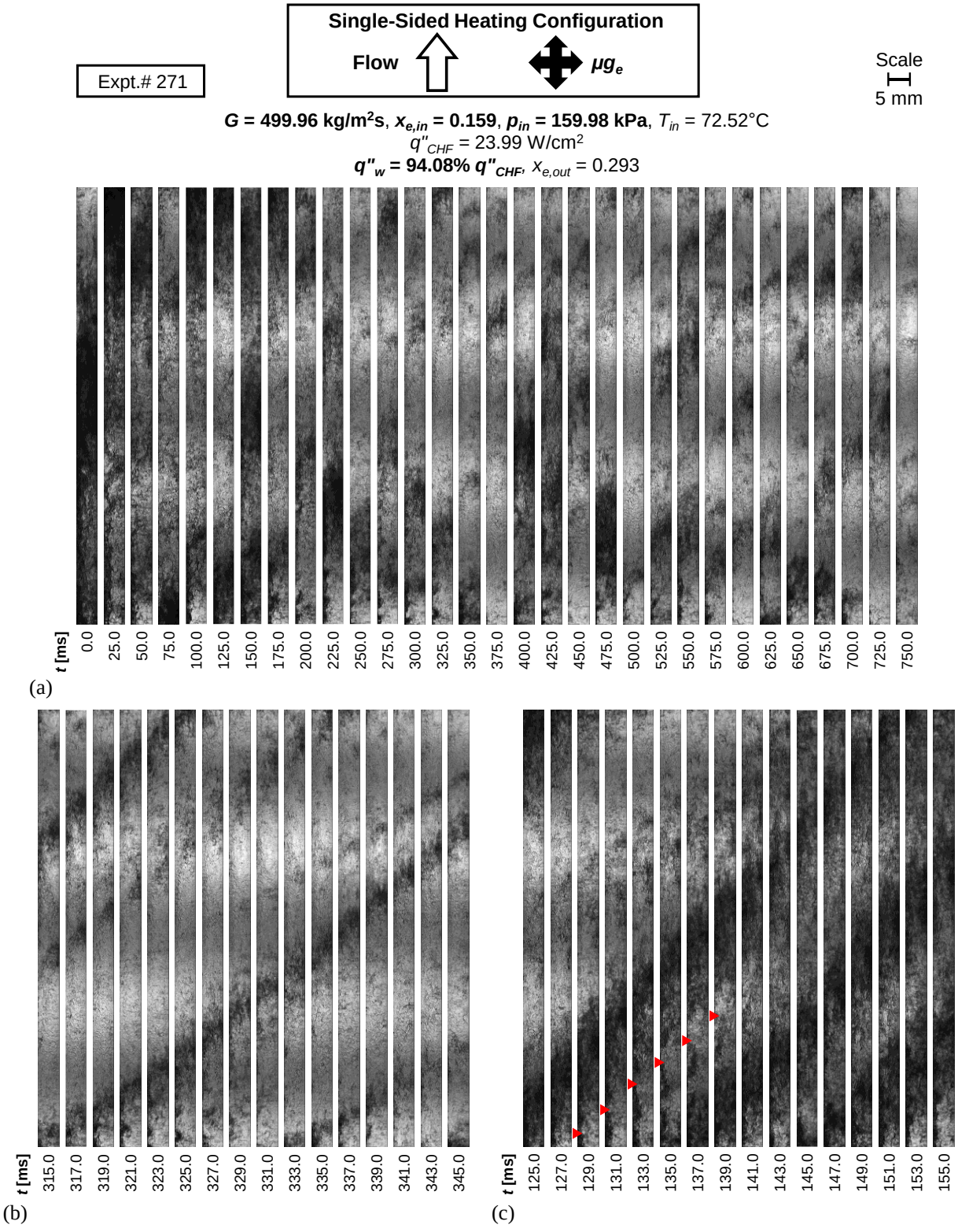

Fig. 12 Flow visualization image sequences for single-sided heating of left wall with mass velocity of $G \approx 500$ kg/m^{2}s, inlet quality of $x_{e,in} = 0.159$, and wall heat flux of $q''_w = 94.08\%$ q''_{CHF}. Shown are (a) the overall transient behavior over an extended time period (25 ms between images), (b) low-density-dominant period (2 ms between images), and (c) high-density-dominant period (2 ms between images). Channel width is 5 mm.

3.2.3 Image Sequences at Low Inlet Quality – Effects of Mass Velocity

Fig. 13-16 presents image sequences for double-sided heating with respective $G \approx 500$, 650, 790, and 1600 kg/m^{2}s, all at $x_{e,in} \approx 0.10$, and $q''_w \approx 83\%\ q''_{CHF}$. Evident in Figs. 13(a)-16(a) is the increasing influence of HDFs with increasing G. Figs. 14 and 15 show relatively small increases in G compared to the image sequences in previous figures. The overall flow patterns and observations made at lower G still hold. One notable difference is the speed at which HDFs propagate through the channel. In Fig. 13(b), with $G \approx 500$ kg/m^{2}s, the HDF entering the channel at the beginning of the sequence remains within it over the entire sequence. However, in Fig. 14(b) for $G \approx 650$ kg/m^{2}s, and Fig. 15(b) for $G \approx 790$ kg/m^{2}s, the HDF exits the channel after 30 and 28 ms, respectively. This is similarly observed in Figs. 13(c) and 15(c) where the HDF initially at the channel inlet exits in ~24 and 22 ms, respectively. Flow patterns are drastically different at the highest G, in Fig. 16. Liquid is dispersed throughout the entire channel due to increased turbulence and mixing, and the distinction between low- and high-density-dominant periods becomes less clear. Table 4 confirms that, as G is increased from 500 to 1600 kg/m^{2}s (Figs. 13-16), HDF velocity monotonically increases from $\bar{u}_{HDF} = 2.34$ to 7.39 m/s during the low- and from 4.78 to 8.82 m/s during the high-density-dominant period.

3.2.4 Image Sequences at Low Inlet Quality – Effects of Inlet Pressure

Fig. 17 contains flow sequences for double-sided heating with similar operating conditions as Fig. 14, $G \approx 650$ kg/m^{2}s, $x_{e,in} \approx 0.10$, and $q''_w \approx 83\%\ q''_{CHF}$, but a lower inlet pressure of p_{in} = 134.05 kPa, compared to 163.65 kPa in Fig. 14. Similar flow patterns are observed for the two pressures during all respective periods. Compared to inlet quality, mass velocity, and heat flux, inlet pressure has a negligible influence on flow patterns for the relatively narrow range of p_{in} in the present study.

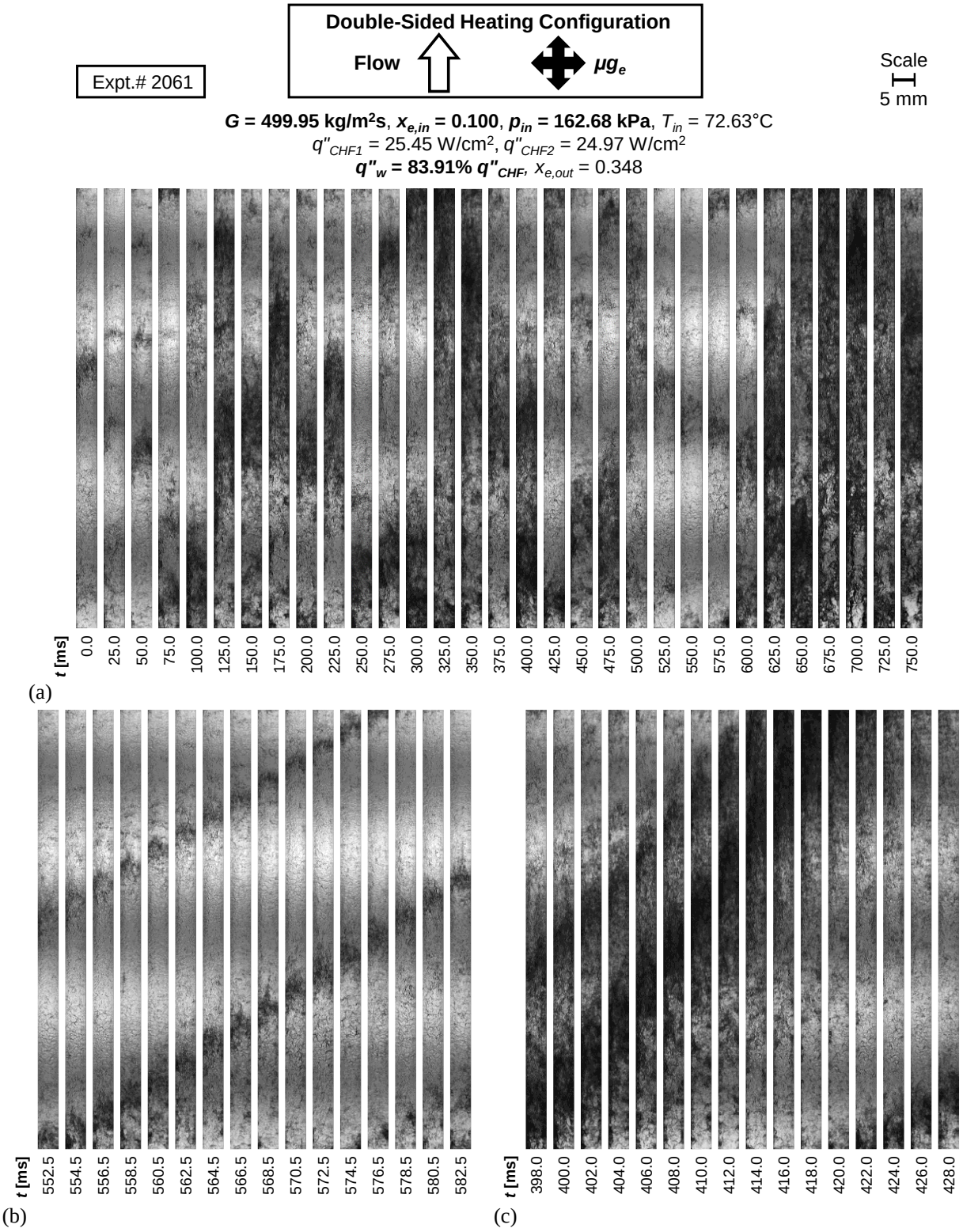

Fig. 13 Flow visualization image sequences for double-sided heating with mass velocity of $G \approx$ 500 kg/m²s, inlet quality of $x_{e,in}$ = 0.100, and wall heat flux of q''_w = 83.91% q''_{CHF}. Shown are (a) the overall transient behavior over an extended time period (25 ms between images), (b) low-density-dominant period (2 ms between images), and (c) high-density-dominant period (2 ms between images). Channel width is 5 mm.

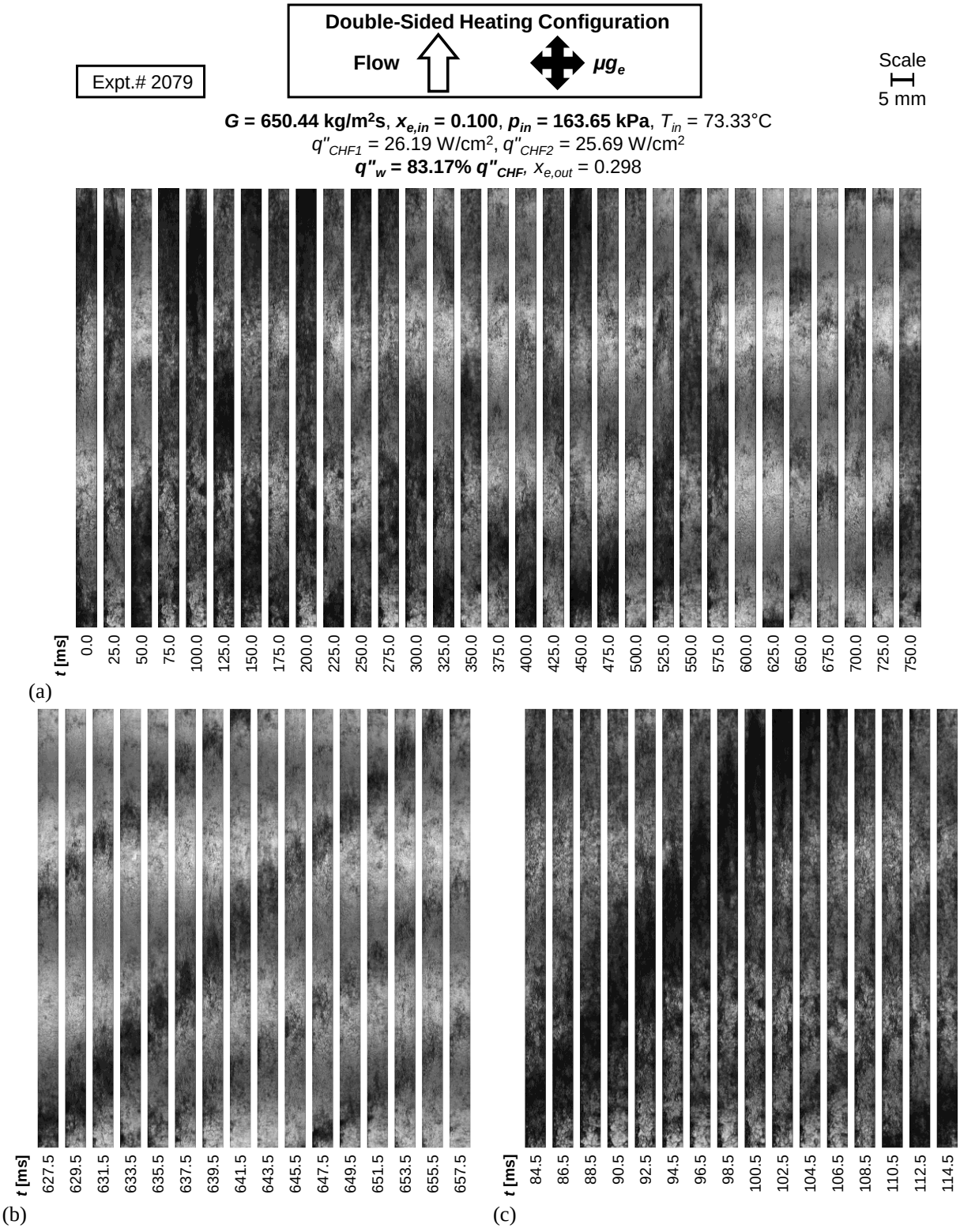

Fig. 14 Flow visualization image sequences for double-sided heating with mass velocity of $G \approx$ 650 kg/m²s, inlet quality of $x_{e,in}$ = 0.100, and wall heat flux of q''_w = 83.17% q''_{CHF}. Shown are (a) the overall transient behavior over an extended time period (25 ms between images), (b) low-density-dominant period (2 ms between images), and (c) high-density-dominant period (2 ms between images). Channel width is 5 mm.

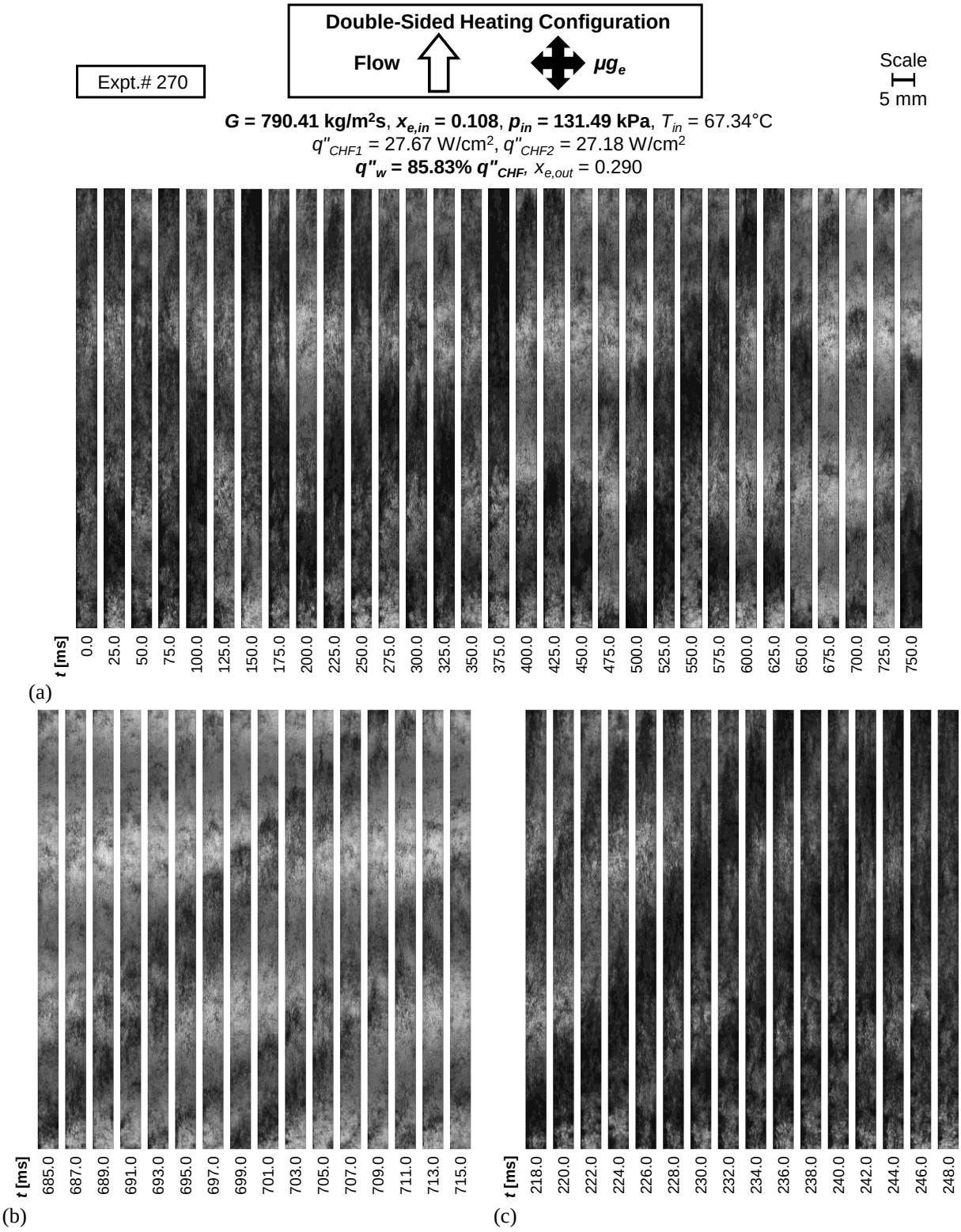

Fig. 15 Flow visualization image sequences for double-sided heating with mass velocity of $G \approx$ 790 kg/m²s, inlet quality of $x_{e,in}$ = 0.108, and wall heat flux of q''_w = 85.83% q''_{CHF}. Shown are (a) the overall transient behavior over an extended time period (25 ms between images), (b) low-density-dominant period (2 ms between images), and (c) high-density-dominant period (2 ms between images). Channel width is 5 mm.

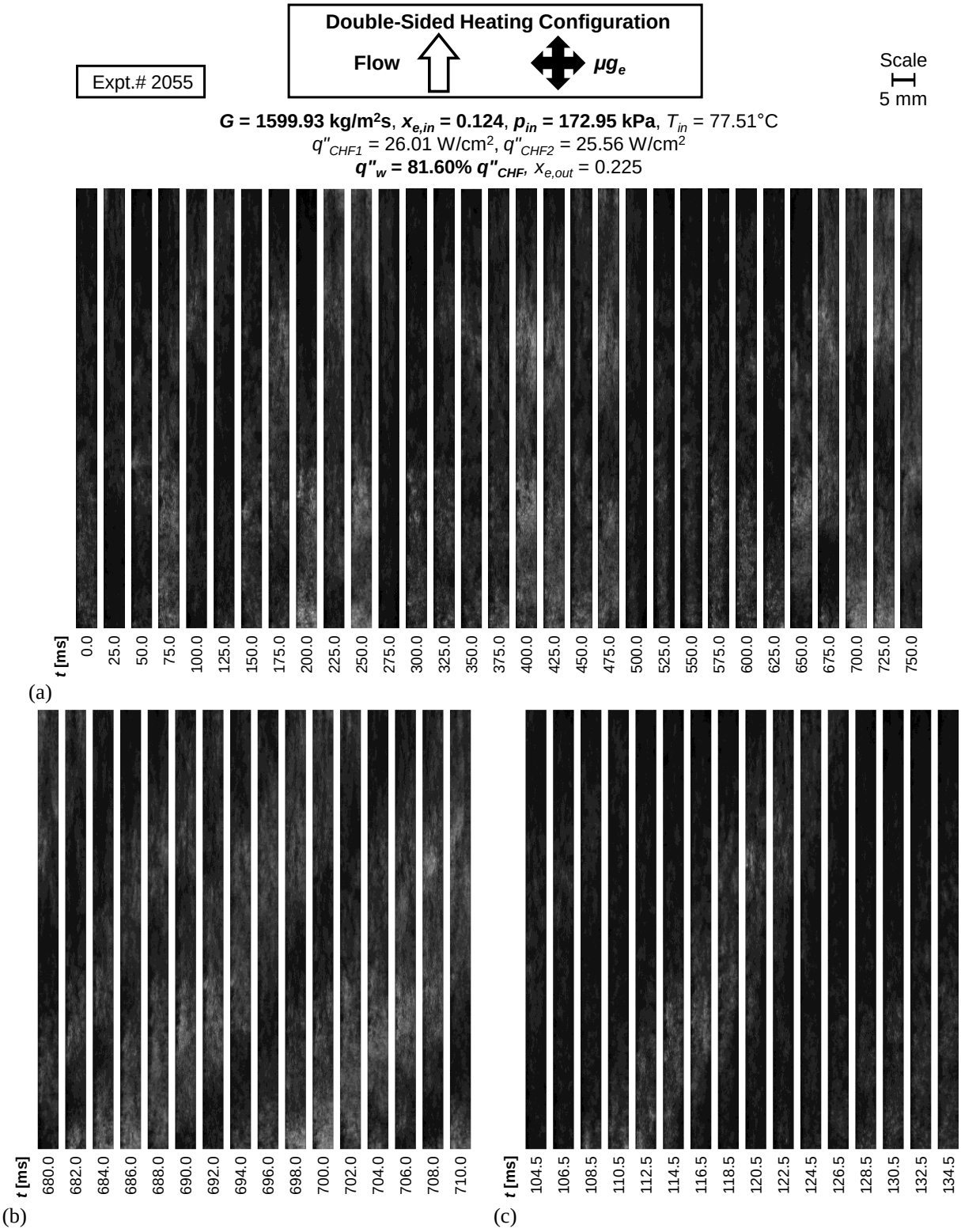

Fig. 16 Flow visualization image sequences for double-sided heating with mass velocity of $G \approx$ 1600 kg/m^{2}s, inlet quality of $x_{e,in}$ = 0.124, and wall heat flux of q''_w = 81.60% q''_{CHF}. Shown are (a) the overall transient behavior over an extended time period (25 ms between images), (b) barely low-density-dominant period (2 ms between images), and (c) high-density-dominant period (2 ms between images). Channel width is 5 mm.

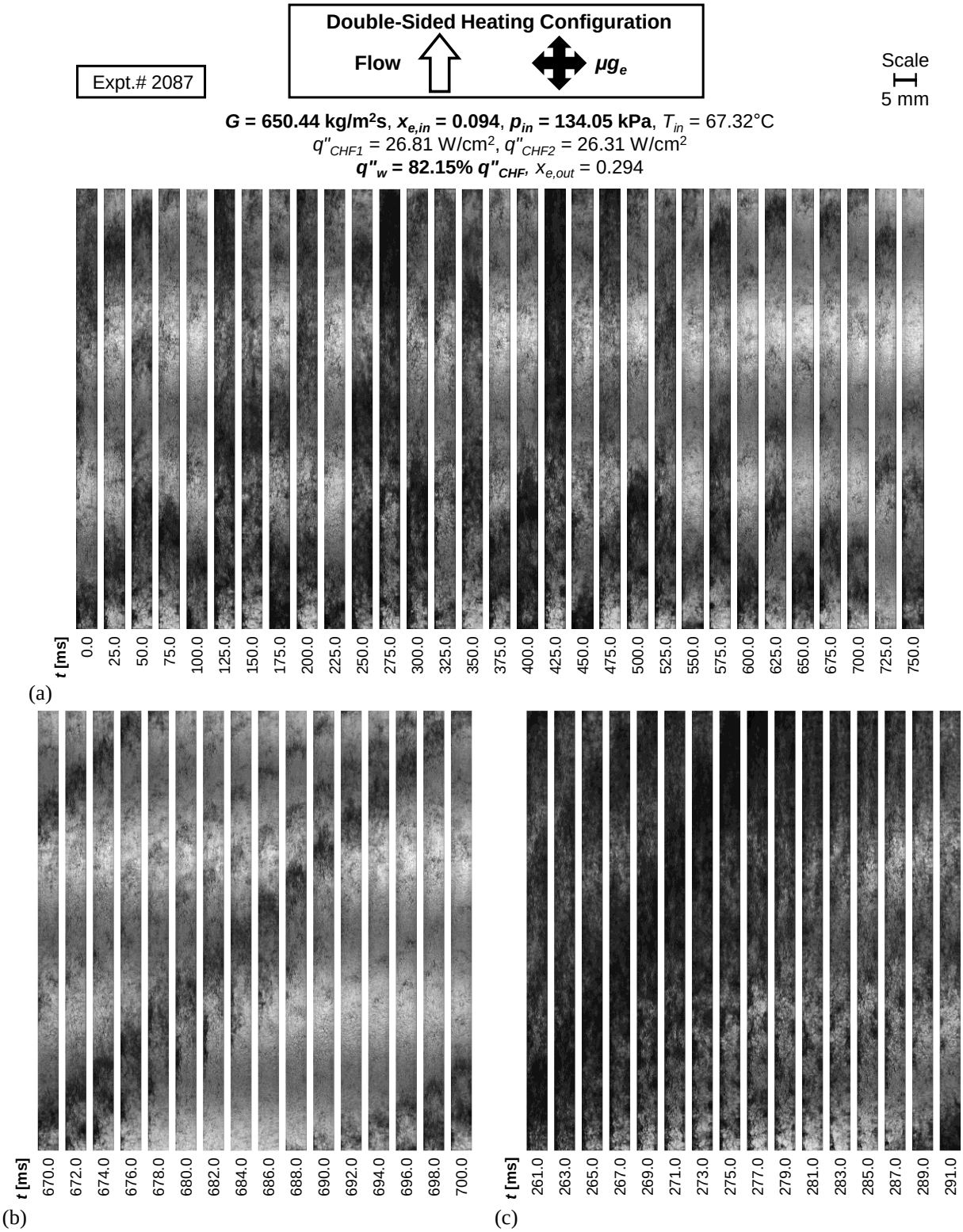

Fig. 17 Flow visualization image sequences for double-sided heating with mass velocity of $G \approx$ 650 kg/m²s, inlet quality of $x_{e,in}$ = 0.094, and wall heat flux of q''_w = 82.15% q''_{CHF}. Shown are (a) the overall transient behavior over an extended time period (25 ms between images), (b) low-density-dominant period (2 ms between images), and (c) high-density-dominant period (2 ms between images). Channel width is 5 mm.

3.3 Average Flow Patterns Along Boiling Curves

The images presented in this section represent the average/intermediate flow pattern, in-between the high- and low-density-dominant periods presented in section 3.2. Each set of images is accompanied by (i) the corresponding set of operating parameters averaged over the respective experimental case, and (ii) the resulting q''_{CHF}. Individual images in each set represent different heat flux increments along the boiling curve, leading up to and including CHF, and the respective heat flux is reported below each image as a percentage of q''_{CHF}.

3.3.1 Flow Patterns for Fixed Mass Velocity – Effects of Inlet Quality, Heat Flux, and Heating Configuration

Fig. 18 presents averaged flow patterns for double-sided heating at a fixed $G \approx 500$ kg/m^{2}s but different $x_{e,in}$. Fig. 18(a) corresponds to the lowest $x_{e,in}$ of 0.100. For relatively low $x_{e,in}$, boiling occurs within the residual liquid layer visible behind passing HDFs. Each image captures the trailing liquid layer in contact with the heated wall, just before liquid contact is extinguished. However, at very low q''_w, shown as 8.17 – 37.10% q''_{CHF} in Fig. 18(a), boiling persists along the entire heated wall, even as the HDF exits. Increasing q''_w results in the liquid layer being sustained a shorter distance downstream. At 51.19% q''_{CHF}, the trailing liquid layer is depleted before the HDF exits the channel. As q''_w is increased, the liquid layer is constrained further upstream. At 100.0% q''_{CHF}, the shortened liquid layer cannot sufficiently cool the heated wall, and the heated strip reaches 122°C.

Figs. 18(b) and (c) present images along the boiling curve for higher $x_{e,in}$ of 0.175 and 0.254, respectively. Flow patterns are similar to those in Fig. 18(a), but the liquid layer recedes from the downstream edge of the channel at a lower 24.87% q''_{CHF} in Fig. 18(b) and 26.26% q''_{CHF} in Fig. 18(c). At CHF, the liquid layer is capable of only reaching a short distance from the channel inlet, prior to evaporating. At even higher $x_{e,in}$, shown in Figs. 18(d-f), boiling within the liquid sublayer trailing HDFs is less apparent. In order to observe parametric trends at high $x_{e,in}$, a uniformly sized HDF in the channel's upstream region is aligned in the presented images. For each $x_{e,in}$, as q''_w is increased from the first increment until CHF, no significant difference in flow patterns is observed. However, throughout each boiling curve, the HDFs featured sporadically within the channel are fainter at the higher $x_{e,in} = 0.493$ in Fig. 18(f) than the lower $x_{e,in} = 0.328$ in Fig. 18(d).

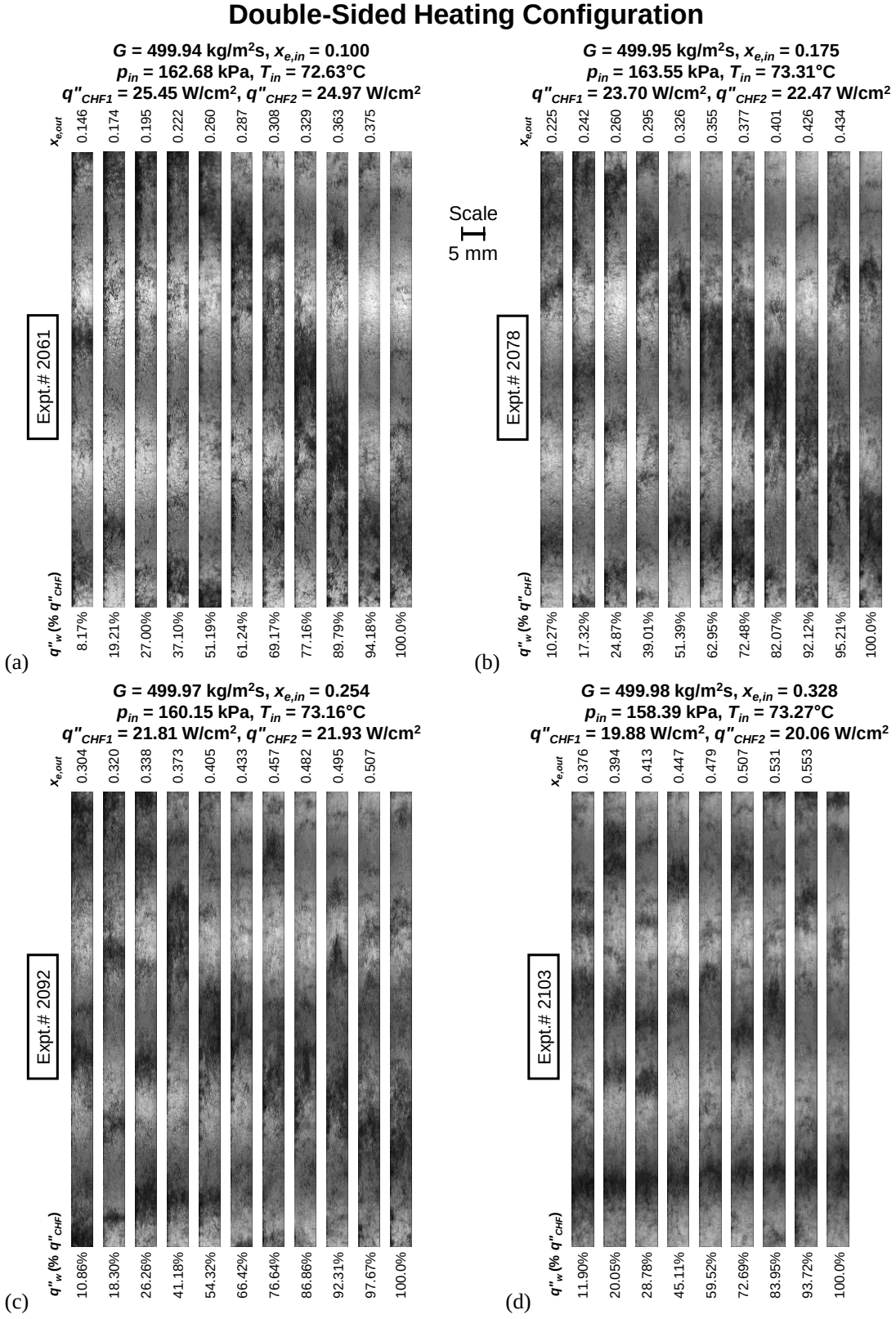

Fig. 18 Flow patterns for increasing heat fluxes until CHF for double-sided heating at a fixed mass velocity of $G \approx 500$ kg/m^{2}s but different inlet qualities of $x_{e,in}$ = (a) 0.100, (b) 0.175, (c) 0.254, (d) 0.328, (e) 0.414, and (f) 0.493. Channel width is 5 mm.

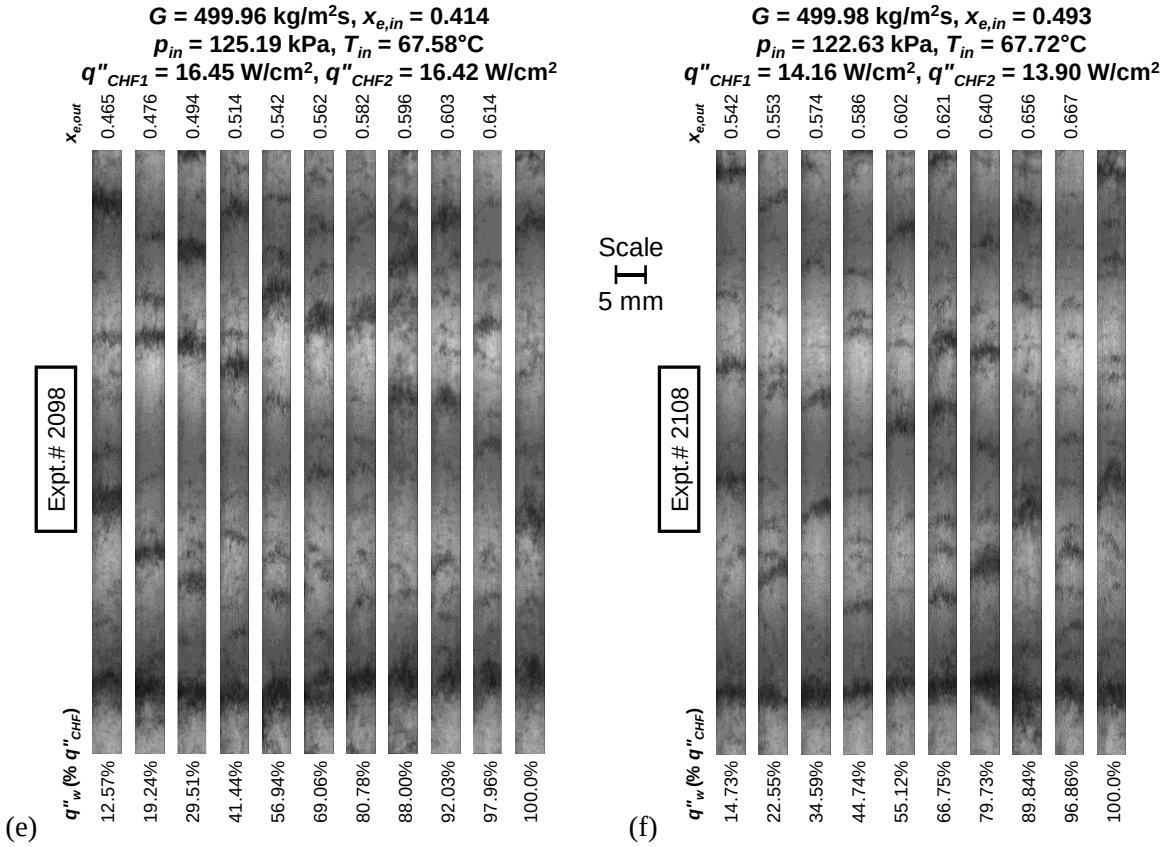

Fig. 18 (continued)

Variations of HDF velocity averaged over the channel length versus q''_w until CHF are shown in Fig. 19 for different $x_{e,in}$. The time instants of $\bar{u}_{HDF}$ measurement correspond to the flow images shown in Fig. 18. Judging by the almost flat horizontal curves, q''_w plays a rather insignificant role in determining the magnitude of $\bar{u}_{HDF}$. Flow acceleration due to boiling within the FBM is not significant when compared to the effects of flow quality introduced at the FBM inlet (which is a consequence of boiling within the BHM). On the other hand, increasing $x_{e,in}$ monotonically increases $\bar{u}_{HDF}$. In Fig. 19, increasing $x_{e,in}$ from 0.100 to 0.414 accelerates the HDFs from 3.00 to 4.29 m/s, *i.e.*, by ~43%. For a given G, higher flow quality implies reduced mixture density, which results in higher flow velocities.

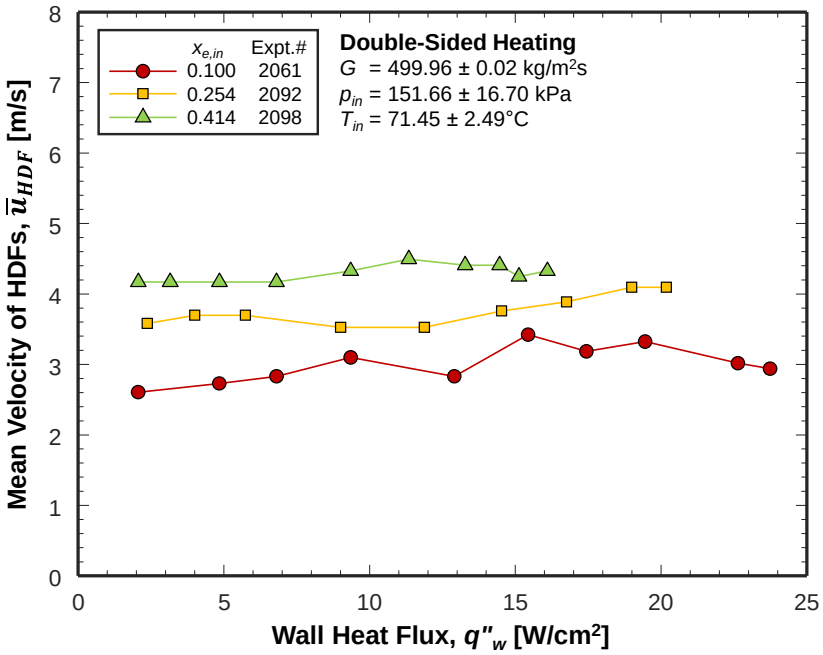

Fig. 19 Variations of mean velocity of HDFs along the channel versus wall heat flux until CHF with double-sided heating for different inlet qualities. The time instants of HDF measurement correspond to the average flow pattern images shown in Fig. 18.

Flow patterns along the boiling curve for single-sided heating at a fixed $G \approx 500$ kg/m^{2}s but different $x_{e,in}$ are shown in Fig. 20. Overall, the flow patterns in each subfigure resemble those at corresponding $x_{e,in}$ for double-sided heating in Fig. 18. Figs. 20(a) and (b) show images at higher $x_{e,in}$ of 0.159 and 0.227, respectively. In both images, up until 50.00% q''_{CHF}, boiling is observed behind an HDF as it exits the channel. However, for double-sided heating, boiling within the residual liquid film is not sustained along the right wall at the channel exit at 51.19% q''_{CHF}, even at $x_{e,in}$ = 0.100 in Fig. 18(a). Figs. 20(c-e) contain images for higher $x_{e,in}$ of 0.342, 0.415, and 0.498, and the dominance of the vapor phase suppresses flow features unique to single-sided heating. The trends observed for double-sided heating with respect to $x_{e,in}$ hold true for single-sided heating, and HDFs become fainter with increasing $x_{e,in}$.

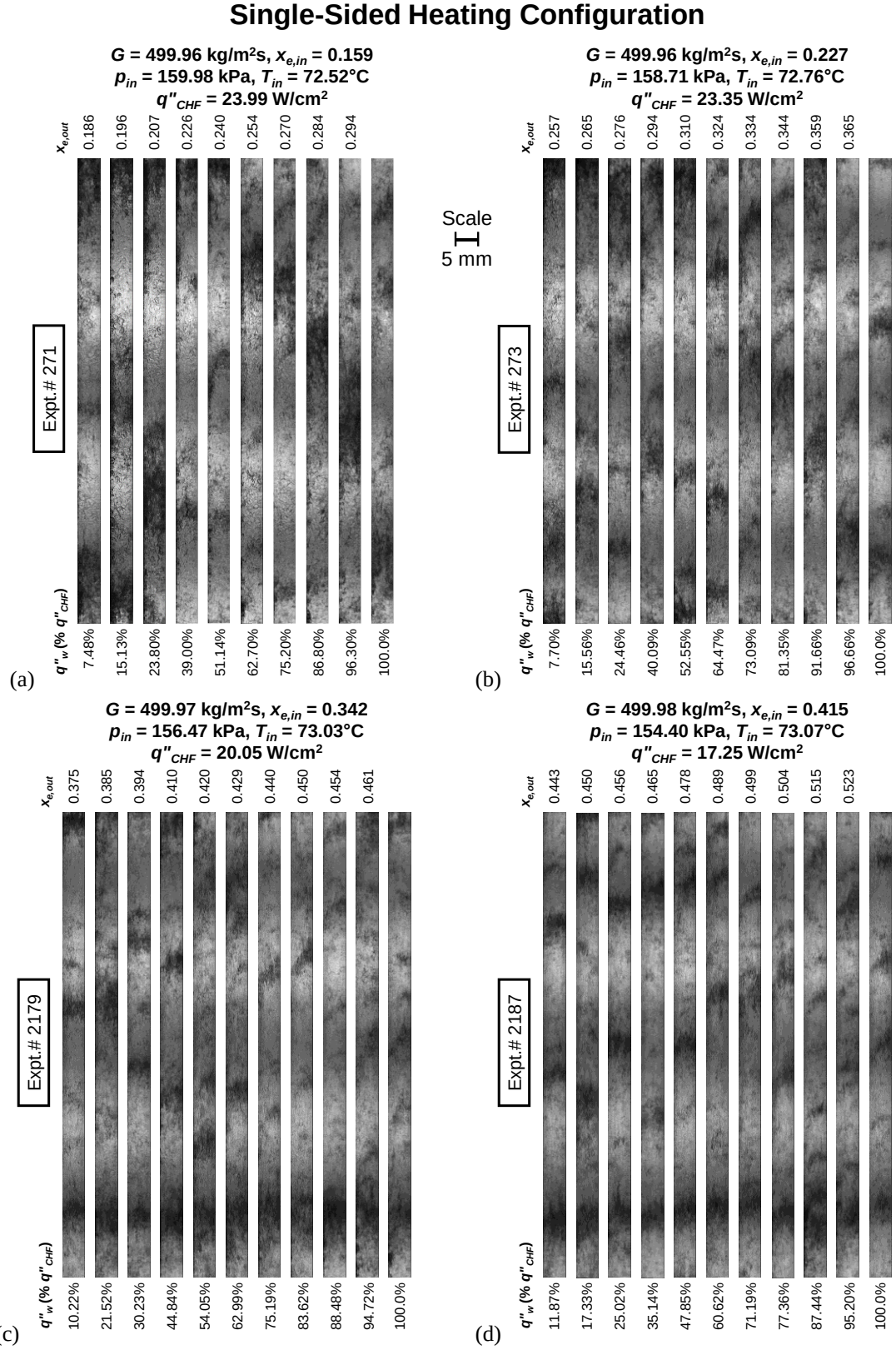

Fig. 20 Flow patterns for increasing heat fluxes until CHF for single-sided heating of left wall at a fixed mass velocity of $G \approx 500$ kg/m^{2}s but different inlet qualities of $x_{e,in}$ = (a) 0.159, (b) 0.227, (c) 0.342, (d) 0.415, and (e) 0.498. Channel width is 5 mm.

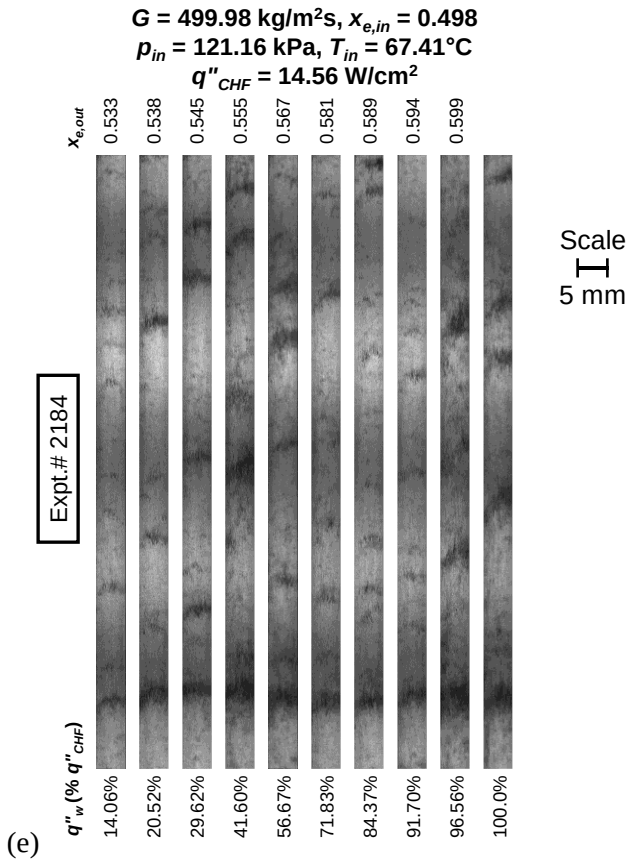

Fig. 20 (continued)

Variations of mean HDF velocity versus q''_w until CHF are shown in Fig. 21 for both single- and double-sided heating, Figs. 20(d) and 18(e), respectively, at near-identical G and $x_{e,in}$. Once again, q''_w plays an insignificant role for both heating configurations. Heating configuration itself also plays an insignificant role with double-sided heating resulting in slightly faster HDFs when compared to single-sided due to greater vapor production, but this could be because of the time instants at which these "average" flow pattern images were selected.

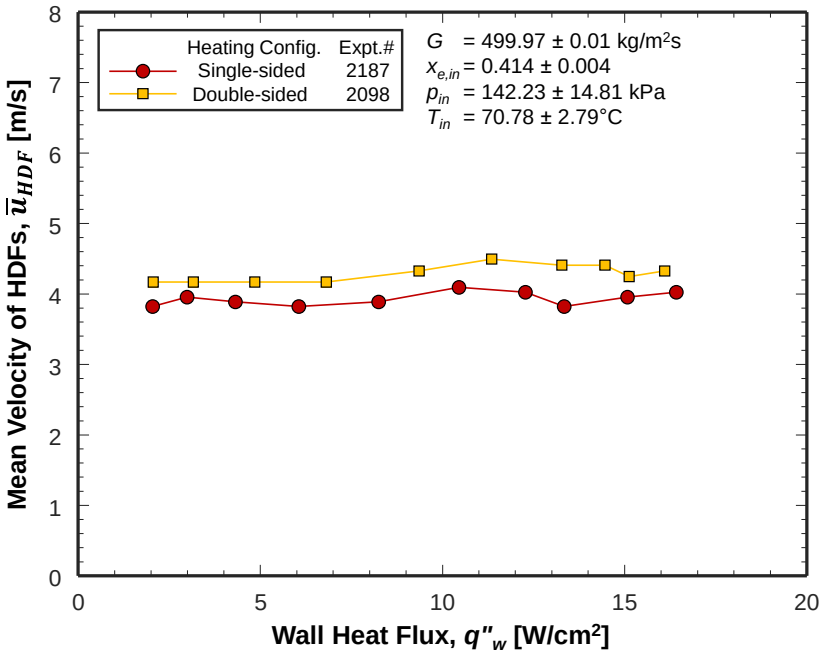

Fig. 21 Variations of mean velocity of HDFs along the channel versus wall heat flux until CHF with single- and double-sided heating at near-identical mass velocity and inlet quality. The time instants of HDF measurement correspond to the average flow pattern images shown in Figs. 18(e) and 20(d).

3.3.2 Flow Patterns at Fixed Low Inlet Quality – Effects of Mass Velocity

Fig. 22 depicts the average flow patterns for each boiling curve for double-sided heating at a relatively low $x_{e,in}$ range of 0.084 – 0.124, but different G. Closer inspection reveals images capture an HDF with a trailing liquid layer on the verge of extinguishment; this is marked in the first image of Fig. 22(a) as an example. Fig. 22(a) depicts the same case as shown in Fig. 18(a) with $G \approx 500$ kg/m^{2}s and $x_{e,in} = 0.100$. Fig. 22(b) shows images for a case with a higher $G \approx 650$ kg/m^{2}s. Unlike the effects of increasing $x_{e,in}$ at low $x_{e,in}$ shown in Figs. 18(a-c), increasing G sustains boiling within the liquid layer further downstream at greater q''_w. At $G \approx 650$ kg/m^{2}s, boiling occurs at the channel exit up to $q''_w = 63.43\%\ q''_{CHF}$ compared to $37.10\%\ q''_{CHF}$ at $G \approx 500$ kg/m^{2}s. At $G \approx 800$ kg/m^{2}s shown in Fig. 22(c), HDFs are larger and darker than at lower G. This is exacerbated at the highest $G \approx 1600$ kg/m^{2}s shown in Fig. 22(d), where HDFs now occupy a large portion of the channel, and LDFs have greater amounts of entrained liquid, impeding the ability to track the liquid layer.

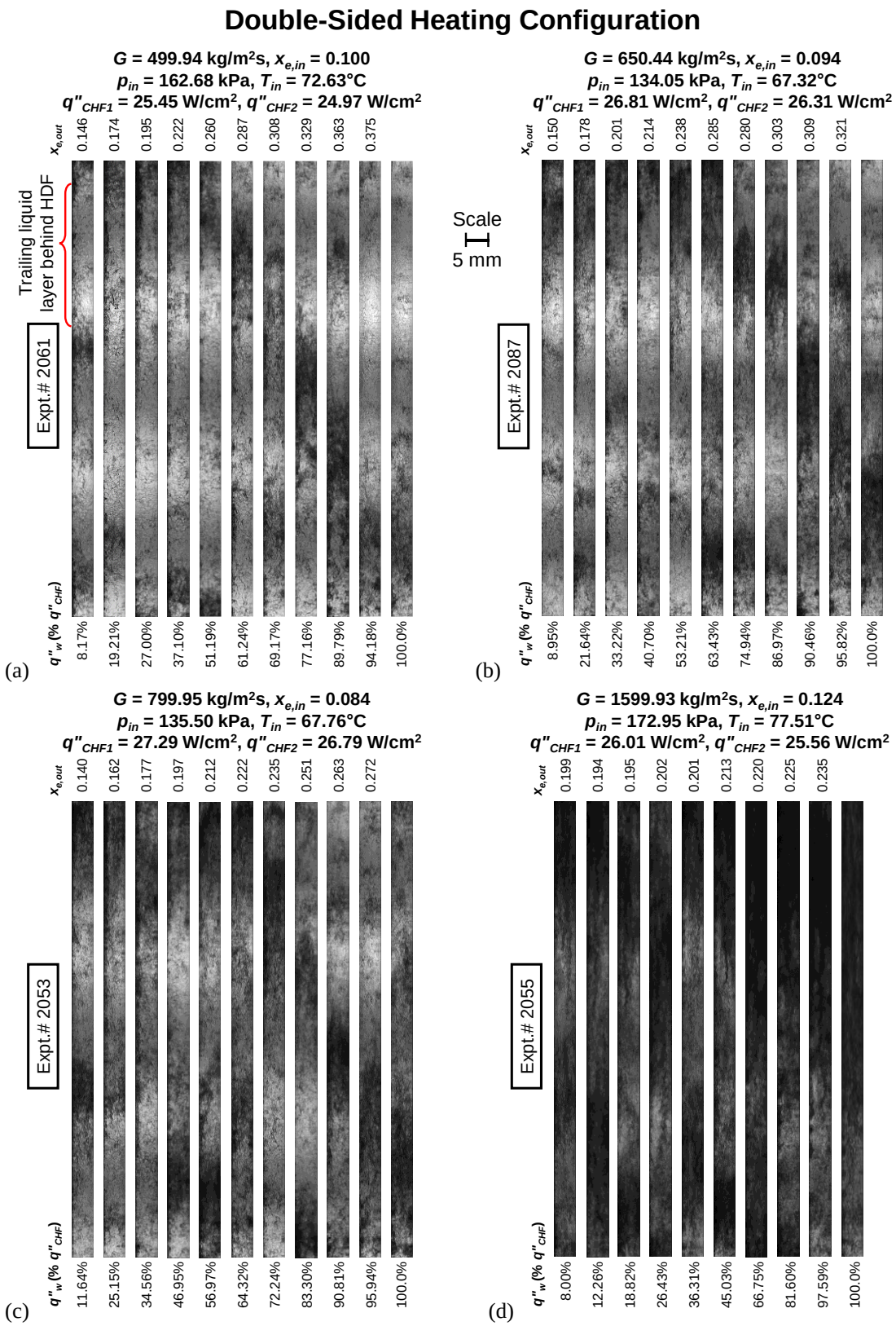

Fig. 22 Flow patterns for increasing heat fluxes until CHF for double-sided heating at a fixed low inlet quality of $x_{e,in} \approx 0.100$ but different mass velocities of $G \approx$ (a) 500, (b) 650, (c) 800, and (d) 1600 kg/m^{2}s. Channel width is 5 mm.

Variations of $\bar{u}_{HDF}$ versus q''_w with double-sided heating are shown in Fig. 23 for different $G \approx$ 500, 800, and 1600 kg/m^{2}s, corresponding to the flow patterns in Figs. 22(a), (c), and (d), respectively. Increasing G significantly increases the velocity of the HDFs within the channel due to higher incoming bulk flow inertia. Increasing G from 500 to 1600 kg/m^{2}s, a factor of 220%, increases $\bar{u}_{HDF}$ from ~3.00 to ~7.17 m/s, a factor of just 139%. The difference in the factors of increase is attributed to small differences in $x_{e,in}$, which results in large differences in mixture density. The effects of mass velocity are once again validated in Appendix E by analyzing flow images at high inlet quality.

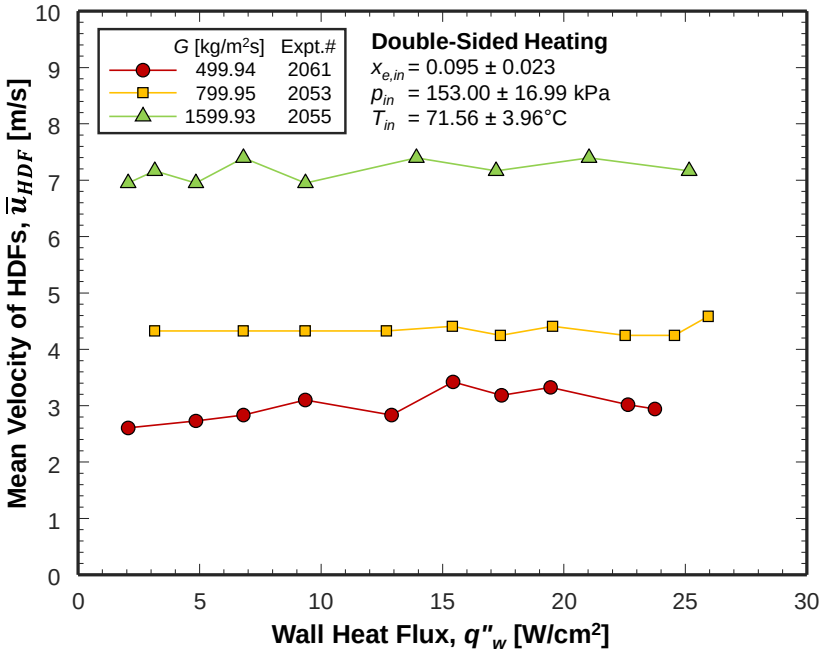

Fig. 23 Variations of mean velocity of HDFs along the channel versus wall heat flux until CHF with double-sided heating for different mass velocities. The time instants of HDF measurement correspond to the average flow pattern images shown in Fig. 22.

4. Heat Transfer of Microgravity Flow Boiling with Two-Phase Inlet – Results and Discussion

Steady-state heat transfer characteristics of microgravity flow boiling with two-phase inlet for both single- and double-sided heating are elaborately presented in this section and parametric trends discussed. These include averaged flow boiling curves, streamwise profiles of wall temperature and heat transfer coefficient, and variations in local and averaged heat transfer coefficients. Heat transfer symmetry and conformation of repeatability of the present experiments is shown in Appendix F.

4.1 Averaged Flow Boiling Curves

Averaged flow boiling curves portray the overall heat transfer characteristics of each heated wall and are plotted as wall heat flux, q''_w, versus average wall superheat, $\overline{T_w} - T_{sat,in}$, where each parameter corresponds to the averaged steady-state value at that heat increment. For two-phase inlet, heat is primarily transferred via boiling within the liquid layer flowing along the heated walls. This means the boiling curves for two-phase inlet share some transition points with those for subcooled inlet such as (i) an ONB (Onset of Nucleate Boiling)/NVG (Net Vapor Generation)-like point at a lower q''_w where the curves' slope increases to an almost constant value in the nucleate boiling region and (ii) an ONBD point at higher q''_w where the curves' slope starts decreasing. Consider any boiling curve presented, such as the ones in Fig. 24. When q''_w is incremented from a minimum, the slope of the curves gradually increases due to (i) development of the nucleate boiling process within the liquid film and (ii) boiling commencing further upstream within the channel. At a certain q''_w, nucleate boiling is fully developed and occurs over the entire channel length, and the curves become linear with a constant slope. The flow contributes some convective aspects to boiling. At an even higher q''_w, nucleate boiling, especially at the downstream portion of the channel degrades due to the formation of a wavy vapor layer beneath the liquid film and incipience of intermittent dryout. This is termed Onset of Nucleate Boiling Degradation (ONBD) or just *dryout incipience*. Further increases in q''_w beyond ONBD results in increased degradation until CHF, where a slight increase in q''_w triggers a large wall superheat increase causing the curve to become almost horizontal due to the wavy vapor layer lifting-off or complete dryout of the heated wall.

4.1.1 Effects of Inlet Pressure and Heating Configuration

Microgravity flow boiling curves are presented in Fig. 24 for both single- and double-sided heating at two different inlet pressures of $p_{in} \approx 127$ and 158 kPa. The other operating conditions are maintained identical at $G \approx 380$ kg/m^{2}s and $x_{e,in} \approx 0.380$. All the curves almost perfectly overlap within experimental uncertainties indicating (i) within the operating ranges of this study, p_{in} does not have a significant effect on heat transfer characteristics and (ii) heating configuration does not significantly influence the heat transfer characteristics, except for a slightly larger q''_{CHF} for single-sided heating. For the same q''_w, double-sided heating transfers twice the heat to the fluid leading to increased vapor production, a factor which usually degrades CHF, but the increased flow acceleration enhances the convective aspects of flow boiling, making q''_{CHF} close to single-sided heating. Owing to its insignificant effects, all boiling curves presented further are not segregated by p_{in}. Note that the respective saturation temperatures for 127 and 158 kPa are 63.96 and 70.91, so even though the wall superheats are equal at each q''_w, the wall temperatures would be ~7°C higher for the higher p_{in}.

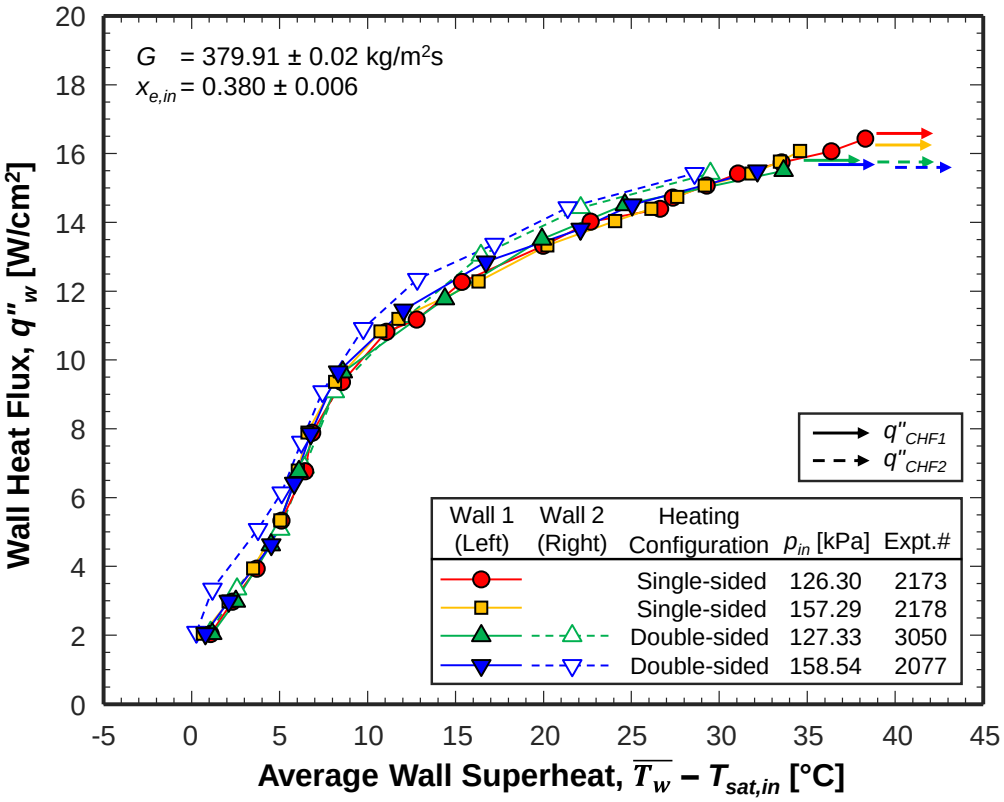

Fig. 24 Microgravity flow boiling curves for both single- and double-sided heating at different inlet pressures, but a fixed mass velocity and inlet quality.

4.1.2 Effects of Mass Velocity

Microgravity flow boiling curves showing the effects of G are presented in Fig. 25 for single-sided heating at various fixed $x_{e,in}$ in the range of -0.001 – 0.585. Included in each plot are curves for G ranging from 180 to 2400 kg/m^{2}s. Note that not all combinations of G and $x_{e,in}$ are possible for experimentation with the FBCE system due to practical limitations of the flow loop's sonic limit and the discrete nature of the BHM heaters.

The lowest $x_{e,in} \approx 0$ included in Fig. 25(a) shows the three cases with $G \approx 180$ kg/m^{2}s have identical nucleate boiling regions with small variations only in the degraded boiling region leading to slightly different q''_{CHF}. Although these cases have $x_{e,in} \approx 0$, typically referring to a saturated liquid, thermodynamic non-equilibrium effects from the BHM result in a liquid-vapor mixture at the FBM channel's inlet. The much higher $G \approx 2400$ kg/m^{2}s results in both the ONB-like and ONBD transition points at much larger q''_w than at 180 kg/m^{2}s. By virtue of its increased flow inertia and ability to better resupply the wall with liquid for sustained boiling, higher G prolongs the degraded boiling region delaying CHF to much larger heat fluxes than that at which ONBD occurs, q''_{ONBD}. For this case, $q''_{ONBD} \approx 20.0$ whereas $q''_{CHF} \approx 37.5$ W/cm^2. Fig. 25(b) shows curves for a slightly higher $x_{e,in}$ of 0.078. Similar trends are seen, excepting the curves for both $G \approx 790$ and 1600 kg/m^{2}s almost overlap with almost no q''_{CHF} augmentation upon doubling G; the only

differences are higher q''_w for the ONB-like and ONBD points. Figs. 25(c-f) show boiling curves for higher $x_{e,in}$ of 0.229 – 0.585, but the span of variation in G in each plot is much narrower than Figs. 25(a) and (b). Nonetheless, all these plots show the same trend of identical nucleate boiling portions of the curve, with higher G monotonically increasing both q''_{ONBD} and q''_{CHF}.

4.1.3 Effects of Inlet Quality

Microgravity flow boiling curves showing the effects of $x_{e,in}$ are presented in Fig. 26 for single-sided heating at various fixed G in the range of 180 – 1600 kg/m^{2}s. Included in each plot are curves for $x_{e,in}$ ranging from -0.002 to 0.587. The lower G of 180, 380, 430, and 500 kg/m^{2}s, respectively presented in Figs. 26(a-d), show identical trends where the boiling curves for all $x_{e,in}$ almost perfectly overlap in the nucleate boiling region, and diverge from this linear trend at different q''_{ONBD}, which decreases with increasing $x_{e,in}$. q''_{CHF} also decreases with increasing $x_{e,in}$. This is due to higher $x_{e,in}$ containing a much smaller volume fraction of liquid available for boiling and liquid film contact with the heated wall cannot be maintained for sufficient distances behind each HDF (as shown in section 3.2). The higher G of 790 kg/m^{2}s shown in Fig. 26(e) has two different sets of nucleate boiling regions. The curves for lower $x_{e,in}$ = 0.059 – 0.183 overlap until the heated-strip reaches the 122°C limit, at which point, the experiments are terminated. This experimental procedure results in a similar q''_{CHF} for moderate to high G coupled with low $x_{e,in}$, which might not represent a true transition to film boiling (due to the entire channel being almost always filled with high-density mixture, Fig. 16). Curves for higher $x_{e,in}$ = 0.433 – 0.582 behave similar to the lower G in Figs. 26(a-d). However, the nucleate boiling region shifting towards the left side for higher $x_{e,in}$ is due to the much larger flow velocity augmenting heat transfer, which results in boiling at T_w extremely close to T_{sat}. The highest $G \approx 1600$ kg/m^{2}s shown in Fig. 26(f) has curves for $x_{e,in}$ = 0.079 and 0.131 fully overlap with identical q''_{CHF}. The shape of the curves' upper portion near CHF tending to become almost horizontal suggests true CHF has indeed reached; note that CHF is truly defined as the heat flux which causes a large, unsteady, and uncontrollable spike in wall superheat.

The effects of both G and $x_{e,in}$ on boiling performance for double-sided heating are shown in Appendix G to be similar to single-sided.

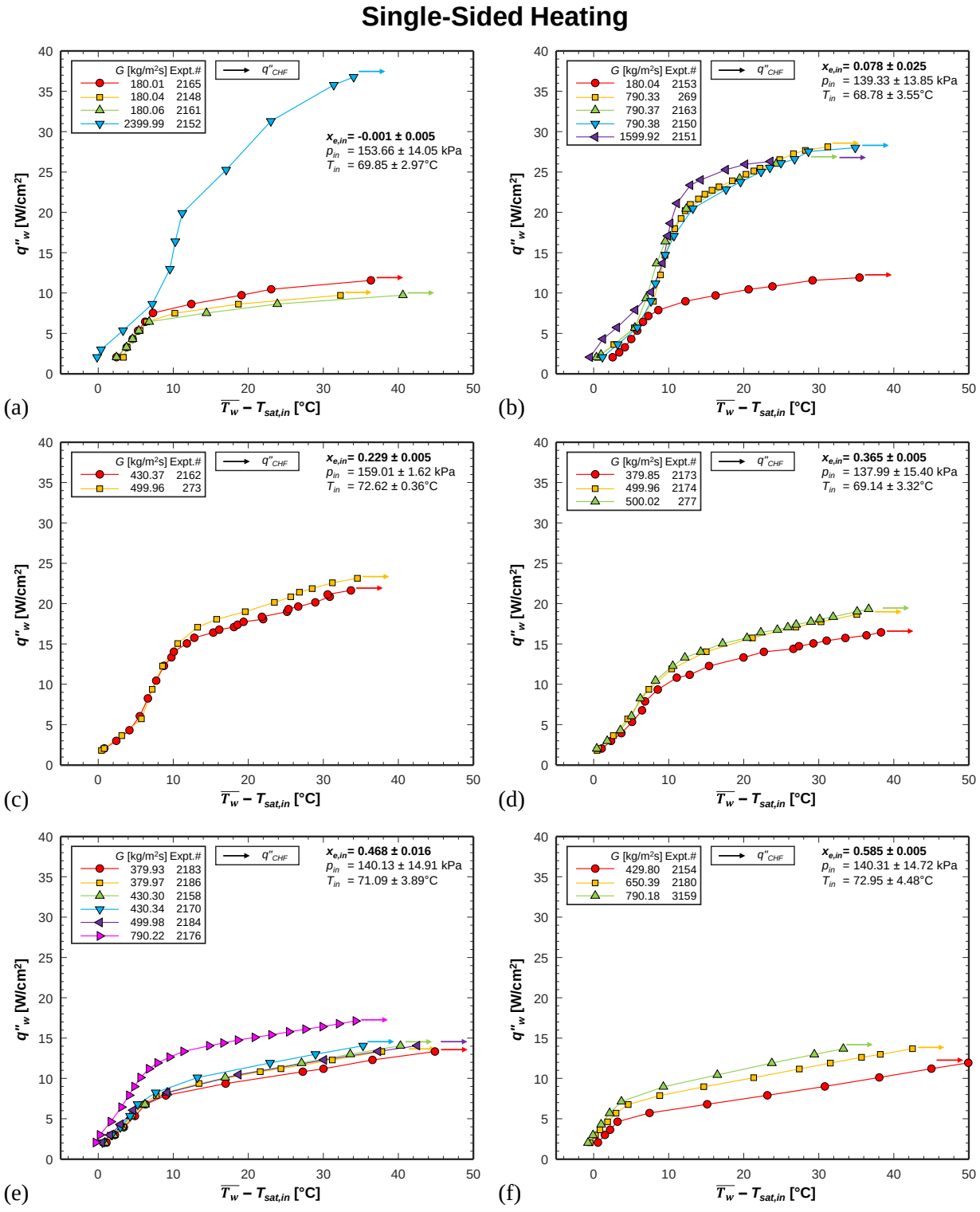

Fig. 25 Microgravity flow boiling curves for two-phase inlet with single-sided heating, showing the effects of mass velocity at various fixed inlet qualities of $x_{e,in}$ = (a) -0.001, (b) 0.078, (c) 0.229, (d) 0.365, (e) 0.468, and (f) 0.585.

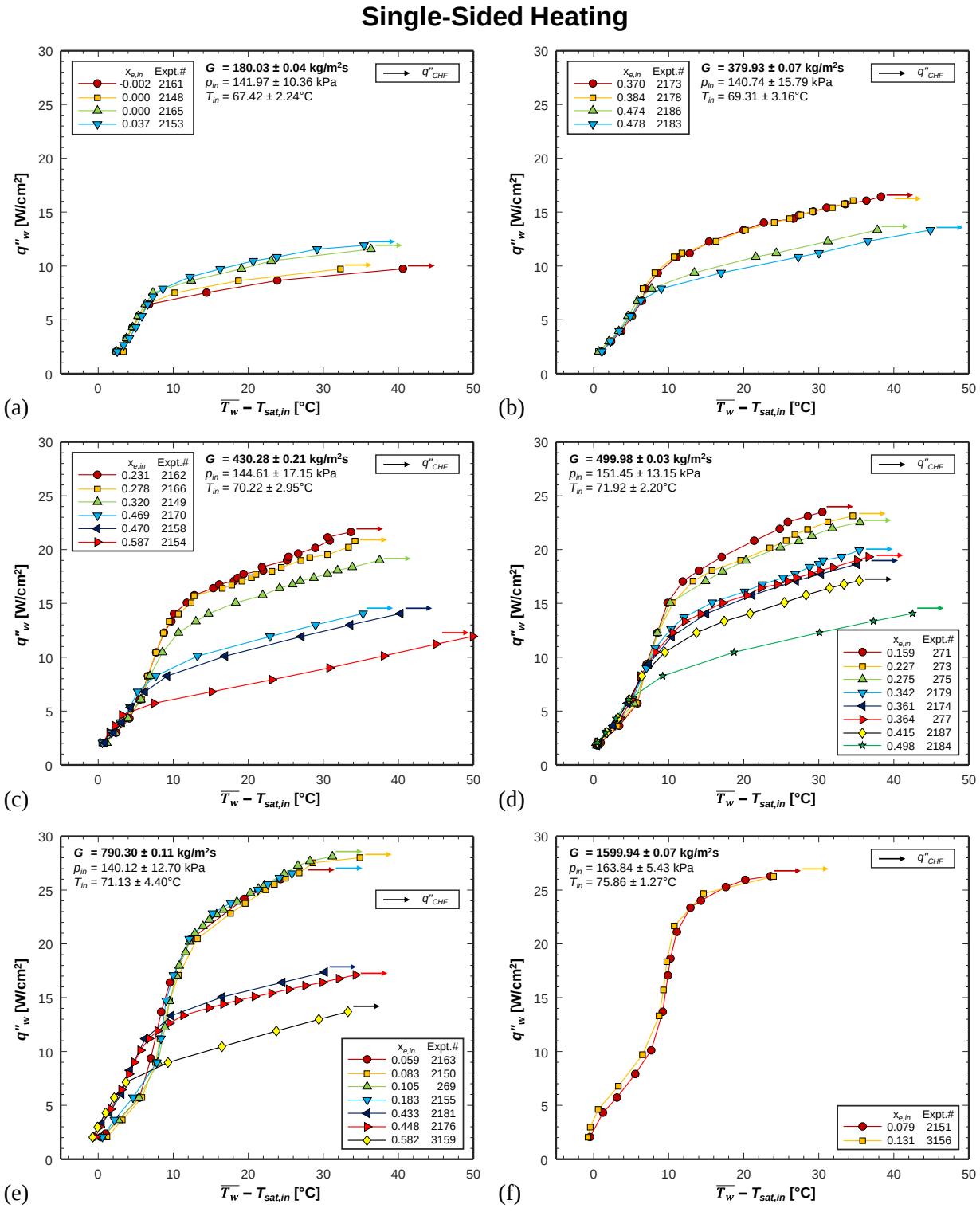

Fig. 26 Microgravity flow boiling curves for two-phase inlet with single-sided heating, showing the effects of inlet quality at various fixed mass velocities of $G \approx$ (a) 180, (b) 380, (c) 430, (d) 500, (e) 790, and (f) 1600 kg/m^{2}s.

4.2 Streamwise Profiles of Wall Temperature

Streamwise profiles of local temperature of both walls ($T_{w,z}$) are presented in Fig. 27. The plots are arranged in the following manner: respectively on the left and right columns are single- and double-sided heating at similar operating conditions and respectively from the top to bottom row are low G at low $x_{e,in}$, high G at low $x_{e,in}$, low G at high $x_{e,in}$, and moderate G at high $x_{e,in}$. Within each plot are included T_w profiles for heat fluxes ranging from ~15% q''_{CHF} to the steady-state heat flux preceding CHF occurrence.

4.2.1 Various Aspects for Single-Sided Heating

The left plot in row 1 of Fig. 27 shows the profiles for lower q''_w are almost flat indicating a nearly isothermal wall. At each streamwise location, T_w monotonically increases with increasing q''_w with the rate of increase rapidly becoming greater at higher q''_w. This is explained by the nature of the boiling regimes, where nucleate boiling is associated with smaller T_w increases over a wide range of q''_w, but beyond ONBD, T_w increases rapidly for small increases in q''_w. At $q''_w \geq$ 73.19 W/cm^2, the curves become concave-downward shaped with T_w peaking between z = 57.3 and 91.9 mm. The concavity becomes larger as q''_w increases, and the peak is indicative of where CHF manifests and takes T_w to 122°C. Both the T_w increase near the channel inlet and the T_w decrease near the channel outlet are possibly due to physical and/or practical design reasons.

The physical reasons are (i) thermal flow development effects near the channel inlet enhances heat transfer and reduces T_w, (ii) flow acceleration effects near the channel outlet due to significant vapor production over the channel length enhances heat transfer and reduces T_w. The practical reason, which is true regardless of the fluid's inlet condition, is the heating strips are designed larger than the fluid heating surface area to effectively embed them within the FBM's polycarbonate layers and sealing with O-rings. The resistive heating elements at either end of the strip cover a larger surface area than the elements in the middle, leading to slightly smaller q''_w at the ends compared to most of the heated length.

The left plot in row 2 shows trends similar to row 1, excepting the profiles near q''_{CHF} show a broad peak spread between z = 22.7 and 91.9 mm. The much higher G, albeit at the same $x_{e,in}$, is responsible for more uniform cooling over the channel length by supplying liquid all along the heated walls. The left plot in row 3 shows profiles similar to row 1, as they both are for low G, but the higher $x_{e,in}$ here degrades cooling capability by the absence of sufficient liquid replenishment, especially near the channel downstream, and causes the profiles to sharply peak around z = 91.9 mm. This trend is also seen in the left plot in row 4, but the higher G provides more cooling to the channel upstream, resulting in an inflexion point at z = 40.0 mm and a sharper peak at z = 91.9 mm.

4.2.2 Comparison of Double-Sided Heating to Single-Sided

For each set of operating conditions, *i.e.*, in each row of Fig. 27, the profiles in the left- and right-side plots match for each heat flux percentage. q''_{CHF} being similar, both heating configurations produce near identical streamwise T_w profiles. In other words, heating configuration has an insignificant effect on T_w.

For double-sided heating, the boiling curves for the two walls overlap for most operating conditions barring two types of deviations. The first type of deviation is the higher q''_w in the top three rows where the entire profiles for wall 1 are higher than those for wall 2, $T_{w1} > T_{w2}$, with the temperature difference between them increasing towards the channel downstream. This is attributed to small differences in q''_w caused by electrical non-uniformity in the heater power controllers' output resulting in large differences in T_w between the two walls between ONBD and CHF. For an example of the q''_w supplied by the power controller to each wall, compare q''_{CHF1} = 13.67 to q''_{CHF2} = 13.22 W/cm^2, the small difference sufficient to produce a large T_w difference at CHF.

The second type of deviation is, in row 2, T_w at z = 5.4 mm is significantly higher for wall 1 than wall 2. This is due to bubble nucleation occurring within the liquid layer at or upstream of z = 5.4 mm for wall 2, whereas bubbles nucleate between z = 5.4 and 22.7 mm for wall 1. Note that this case has a combination of high G and low $x_{e,in}$, so liquid concentration within the channel is high and the liquid layer's required superheat for bubble incipience is only attained after convection heat transfer for a short distance upstream. Another possibility is uneven distribution of incipience cavities on both walls even though both heated strips were vapor polished to the same surface finish.

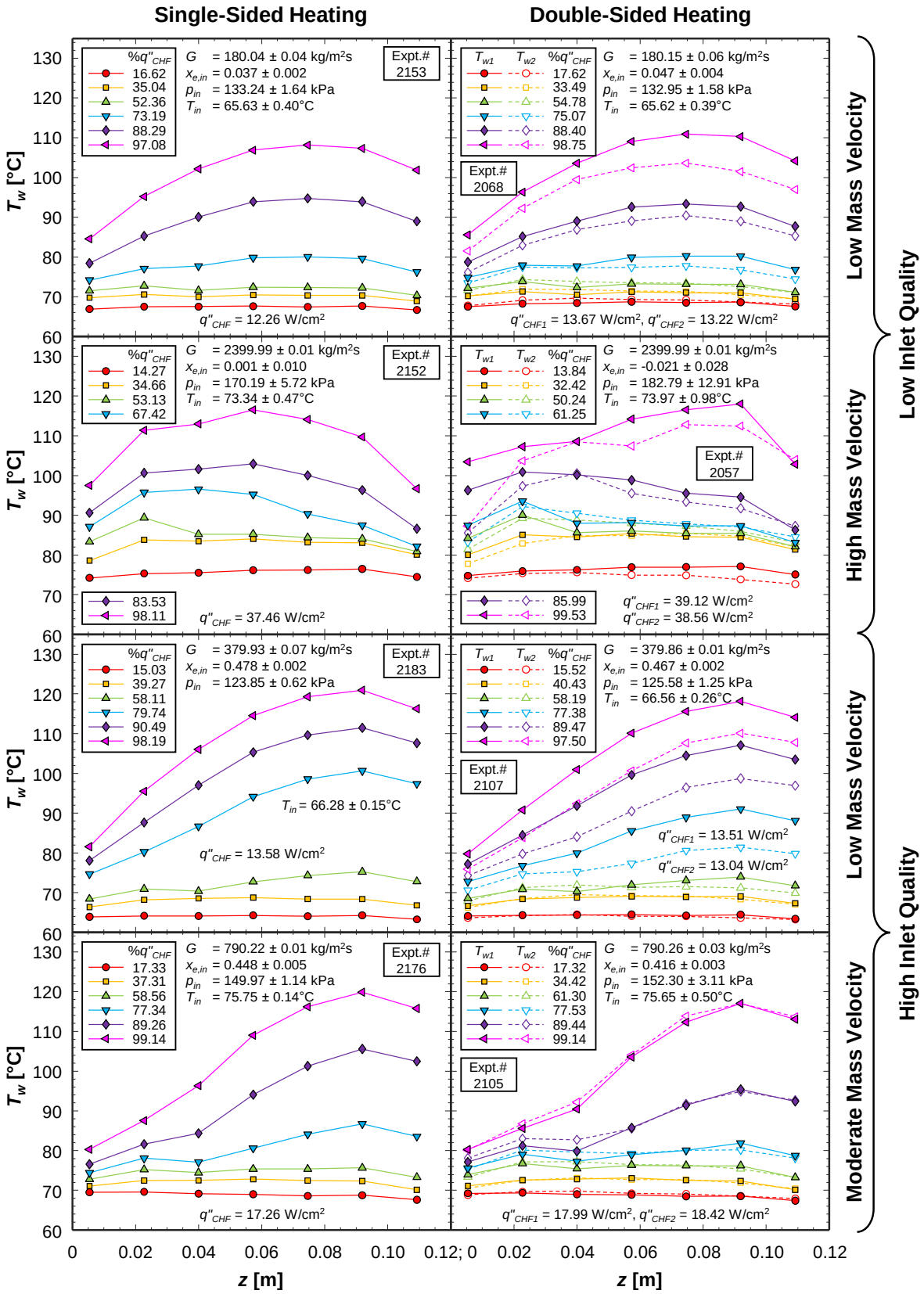

Fig. 27 Streamwise profiles of local wall temperature (T_w versus z) for different heat fluxes (q''_w) at a variety of inlet conditions with single- and double-sided heating.

4.3 Streamwise Profiles of Heat Transfer Coefficient

Streamwise profiles of heat transfer coefficient (h_z) for both walls are presented in Fig. 28 for different heat fluxes at a variety of inlet conditions with both single- and double-sided heating. The layout of this figure and the choice of operating conditions in each plot are identical to Fig. 27.

The h_z profiles for both heating configurations are very similar at similar conditions. Reasons for the deviations have already been elaborated in section 4.2. At each streamwise location, there is no clear trend of h_z variation with increasing q''_w as it is completely determined by the local boiling regime. At all operating conditions and heating configurations, the h_z profiles for ~95% q''_{CHF} are completely degraded below all other q''_w. Comparing rows 1 and 2, higher G yields higher h_z profiles for all q''_w due to enhanced convective effects augmenting heat transfer.

Nearly all h_z profiles are shaped concave-upward with a h decrease near the inlet due to flow becoming thermally fully developed, a rather constant middle portion, and a h increase near the outlet due to flow acceleration effects. The higher h_z at the ends, *i.e.*, at z = 5.4 and 109.2 mm, might be artificial due to the practical design reasons already elaborated in section 4.2. Nonetheless, the curvature of the h_z profiles over the entire channel length is indicative of true flow boiling physics. For example, see rows 3 and 4 for high $x_{e,in}$ where the profiles at high q''_w decrease over the upstream half of the channel and remain constant over the downstream half of the channel. The causation is majorly physical with the large decrease upstream due to nucleate boiling degradation at such large local qualities and the flat region downstream due to h having degraded to low values characteristic of insufficient liquid availability for boiling. Flow visualization supplements this reasoning by showing a lack of HDFs (or maybe very light and thin HDFs) in the channel downstream at high $x_{e,in}$, which is further discussed in section 3.3.3 and Appendix E.

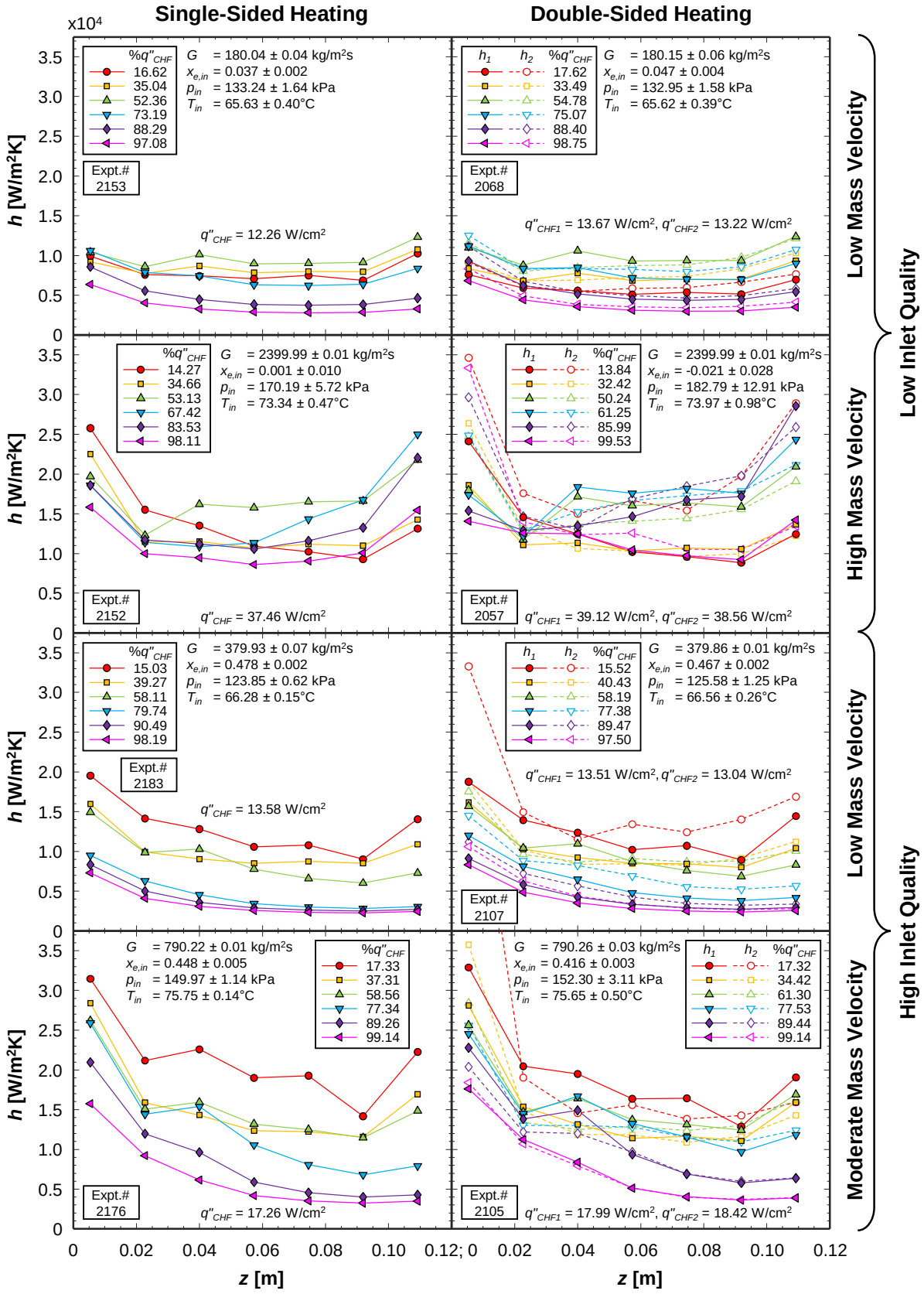

Fig. 28 Streamwise profiles of local heat transfer coefficient (h versus z) for different heat fluxes (q''_w) at a variety of inlet conditions with single- and double-sided heating.

4.4 Heat Transfer Coefficient versus Thermodynamic Equilibrium Quality

Variations of local heat transfer coefficient, h_z, at each heated wall versus local thermodynamic equilibrium quality, x_e, are presented in Fig. 29 for different heat fluxes. Plots are laid out identical to Figs. 27 and 28. The operating condition in each plot is the same as Fig. 28 but h_z only at z = 22.7 – 91.9 mm are considered here to focus on trends due to flow boiling physics rather than include potential trends confounded by the heated-strip design aspects discussed in section 4.2.

h_z versus local flow quality, x, provides an idea of local boiling physics. Ideally, $x \approx x_e$, but from section 3, clear traditional flow regimes such as bubbly, slug, annular flow, *etc*., are not seen at a steady state. Instead, the flow patterns are complex with HDFs and LDFs alternately traversing the channel, so typical boiling mechanisms are inferred here.

Each curve spans a different x_e range depending on the heat added to the fluid, with the span increasing with increasing q''_w and doubling for double-sided heating over single-sided for the same fixed q''_w (since q''_{CHF} is similar for both heating configurations). Although the x_e spans are vastly different for single- and double-sided heating and local x_e significantly varies along the channel, the trends of these curves are similar for each operating condition.

For both low and high G at low inlet quality (rows 1 and 2), at a particular x_e in each plot, h_z first increases with increasing q''_w until local ONBD is reached after which it decreases. In fact, after ONBD is reached, the entire h_z curves are rather flat with a constant h_z over a range of x_e as broad as ~0.26 for the top right plot. At lower $x_{e,in}$ and hence lower x_e, h_z is always a function of q''_w and the curves never merge at any x_e. This is indicative of the dominance of nucleate boiling regime where the volume fraction of liquid is high and flow velocity is relatively small.

At high $x_{e,in}$ shown in rows 3 and 4, all the curves show a significant gradual decrease in h_z with increasing x_e as opposed to the curves for low $x_{e,in}$. Several typical reasons for this trend include strong vapor shear, dryout incipience, and increasing periods of intermittent dryout [39]. For low G at high $x_{e,in}$ (row 3), the curves for $q''_w \geq 80\%\ q''_{CHF}$ are seen to merge for $x_e > \sim 0.52$ and the other curves show a decreasing trend with increasing x_e and could merge for high qualities as well. The same trend is seen for high G at high $x_{e,in}$ (row 4), where the rate of decrease of each curve with increasing x_e intuitively suggests merging for x_e between 0.5 and 0.6. After merging, h_z would be independent of q''_w. These trends are indicative of the dominance of convective boiling regime characterized by high flow velocities, large void fractions, and liquid film evaporation.

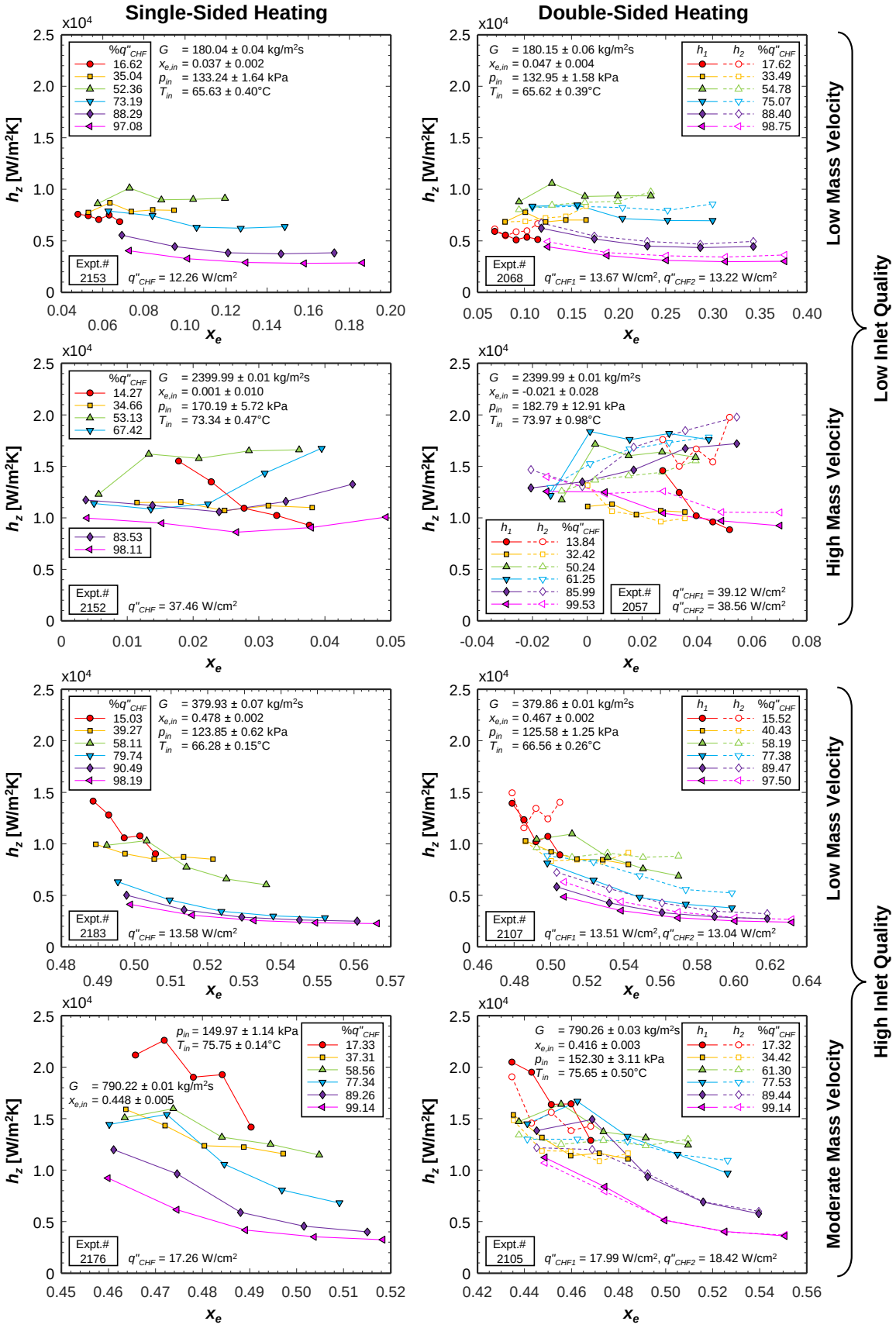
Single-Sided Heating
Double-Sided Heating
Low Mass Velocity
High Mass Velocity
Moderate Mass Velocity
Low Inlet Quality
High Inlet Quality
x10⁴
h_z [W/m²K]
x_e
%q"_CHF
16.62
35.04
52.36
73.19
88.29
97.08
G = 180.04 ± 0.04 kg/m²s
x_e,in = 0.037 ± 0.002
p_in = 133.24 ± 1.64 kPa
T_in = 65.63 ± 0.40°C
Expt.# 2153
q"_CHF = 12.26 W/cm²
G = 180.15 ± 0.06 kg/m²s
x_e,in = 0.047 ± 0.004
p_in = 132.95 ± 1.58 kPa
T_in = 65.62 ± 0.39°C
h_1 h_2 %q"_CHF
17.62
33.49
54.78
75.07
88.40
98.75
Expt.# 2068
q"_CHF1 = 13.67 W/cm², q"_CHF2 = 13.22 W/cm²
%q"_CHF
14.27
34.66
53.13
67.42
83.53
98.11
G = 2399.99 ± 0.01 kg/m²s
x_e,in = 0.001 ± 0.010
p_in = 170.19 ± 5.72 kPa
T_in = 73.34 ± 0.47°C
Expt.# 2152
q"_CHF = 37.46 W/cm²
G = 2399.99 ± 0.01 kg/m²s
x_e,in = -0.021 ± 0.028
p_in = 182.79 ± 12.91 kPa
T_in = 73.97 ± 0.98°C
h_1 h_2 %q"_CHF
13.84
32.42
50.24
61.25
85.99
99.53
Expt.# 2057
q"_CHF1 = 39.12 W/cm²
q"_CHF2 = 38.56 W/cm²
%q"_CHF
15.03
39.27
58.11
79.74
90.49
98.19
G = 379.93 ± 0.07 kg/m²s
x_e,in = 0.478 ± 0.002
p_in = 123.85 ± 0.62 kPa
T_in = 66.28 ± 0.15°C
Expt.# 2183
q"_CHF = 13.58 W/cm²
G = 379.86 ± 0.01 kg/m²s
x_e,in = 0.467 ± 0.002
p_in = 125.58 ± 1.25 kPa
T_in = 66.56 ± 0.26°C
h_1 h_2 %q"_CHF
15.52
40.43
58.19
77.38
89.47
97.50
Expt.# 2107
q"_CHF1 = 13.51 W/cm², q"_CHF2 = 13.04 W/cm²
p_in = 149.97 ± 1.14 kPa
T_in = 75.75 ± 0.14°C
%q"_CHF
17.33
37.31
58.56
77.34
89.26
99.14
G = 790.22 ± 0.01 kg/m²s
x_e,in = 0.448 ± 0.005
Expt.# 2176
q"_CHF = 17.26 W/cm²
G = 790.26 ± 0.03 kg/m²s
x_e,in = 0.416 ± 0.003
p_in = 152.30 ± 3.11 kPa
T_in = 75.65 ± 0.50°C
h_1 h_2 %q"_CHF
17.32
34.42
61.30
77.53
89.44
99.14
Expt.# 2105
q"_CHF1 = 17.99 W/cm², q"_CHF2 = 18.42 W/cm²

Fig. 29 Variations of local heat transfer coefficient at each heated wall, h_z, versus local thermodynamic equilibrium quality, $x_{e,in}$, for different heat fluxes, q''_w, with single- and double-sided heating at a variety of inlet conditions.

4.5 Parametric Trends of Average Heat Transfer Coefficient

Variations of average heat transfer coefficient, $\bar{h}$, with heat flux, q''_w, for each heated wall are presented in Fig. 30 for different $x_{e,in}$ at six combinations of operating conditions and heating configuration. The layout of this figure is as follows: respectively from the top to bottom row are plots for increasing $G \approx 380$, 500, and 790 kg/m^{2}s, and respectively on the left and right side are single- and double-sided heating at similar operating conditions. Within each plot, $x_{e,in}$ is varied over a wide range, but within the limits of the experimental system for that particular G.

All curves portray the same trend with the following aspects: (i) a large $\bar{h}$ at the lowest q''_w, and as q''_w is increased, (ii) a sharp decrease to a local minimum, (iii) a gradual slight increase to a local maximum, and (iv) another decrease (although more gradual) leading to a minimum at CHF. This trend is identical for vertical upflow in Earth gravity [29] and the physical reasoning is similar, excepting that flow acceleration due to vapor production is only due to increase in specific volume of the two-phase mixture and not buoyancy. Aspect (i) is due to bubble nucleation within the annular liquid layer at extremely low wall superheats. Aspect (ii) is due to increase in wall superheat for nucleate boiling as it develops. Aspect (iii) is due to greater vapor production causing greater flow acceleration and enchancement in convective aspects of flow boiling heat transfer. The local peak here indicates the ONBD point, so aspect (iv) is essentially an aftermath of boiling degradation by formation of the wavy vapor layer underneath the liquid layer and significant downstream void fraction causing intermittent dryout incipience, which overshadows acceleration effects.

For each fixed G, higher $x_{e,in}$ yields higher $\bar{h}$ at smaller q''_w and lower $\bar{h}$ at larger q''_w. This is due to faster liquid-vapor mixture traversing the channel, which at smaller q''_w, enhances heat transfer by virtue of a faster moving liquid film and liquid replenishment further downstream, but at larger q''_w, results in significant increase in void fraction in the channel downstream degrading heat transfer. Higher G results in the $\bar{h}$ curves for each $x_{e,in}$ to span a broader q''_w range due to each regime transition point including CHF delayed to higher heat fluxes.

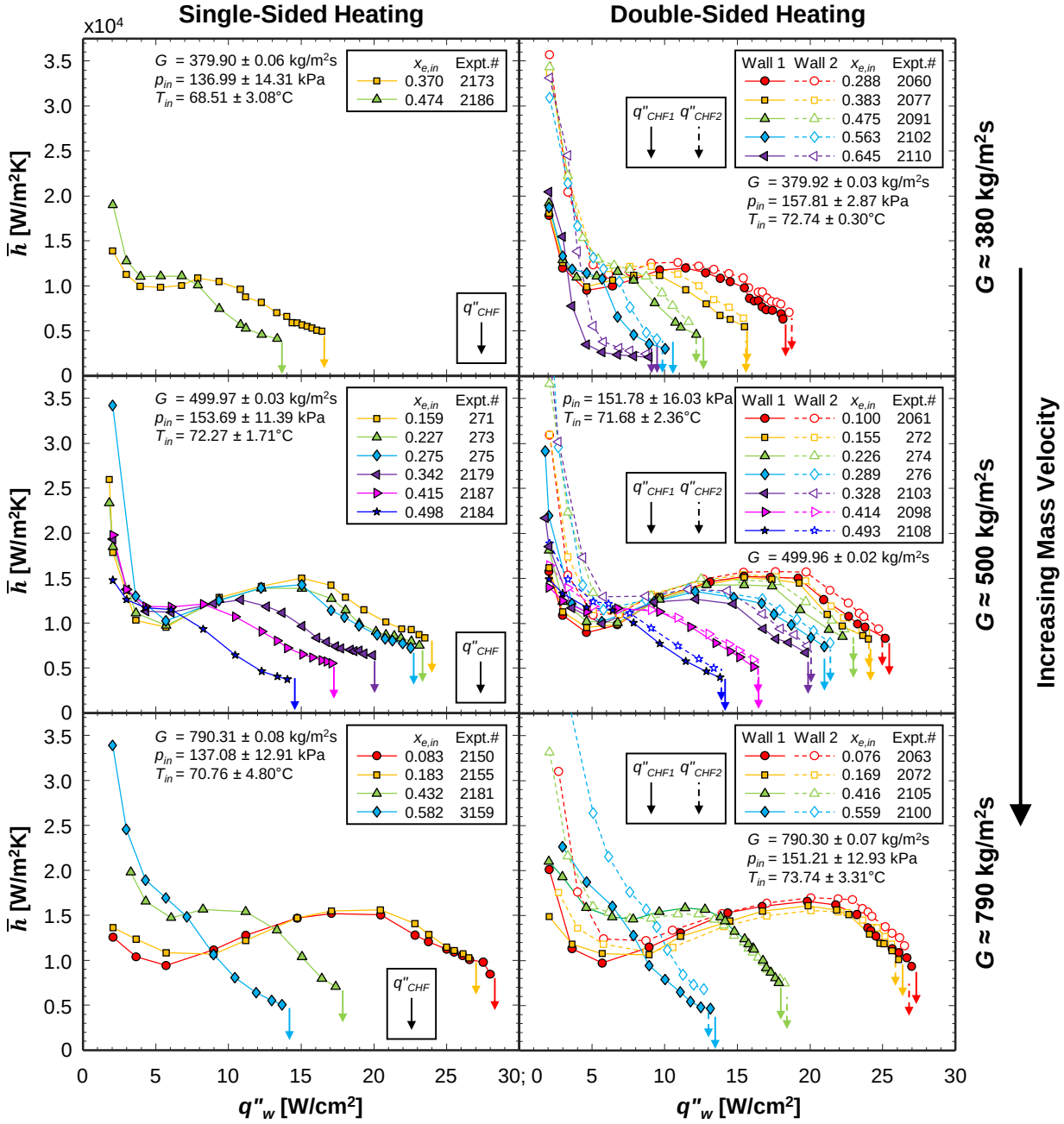

Fig. 30 Variations of average heat transfer coefficient, $\bar{h}$, versus wall heat flux, q''_w, for different inlet qualities, $x_{e,in}$, at six combinations of operating conditions and heating configuration: mass velocity, G, is increasing from the top to bottom plot, and single- and double-sided heating are respectively on the left and right.

Variations of $\bar{h}$ with q''_w for each heated wall are presented in Fig. 31 for different G at low and high $x_{e,in}$. Fig. 31(a) shows, for a low $x_{e,in} \approx 0.04$, increasing G does not significantly change the linear developed boiling portions of the curves, but it enhances $\bar{h}$ at both lower and higher heat fluxes (*i.e.*, below and above the linear portions) as well as augment q''_{ONBD} and q''_{CHF}. This is owing to the ability of higher G to better replenish the wall with liquid, especially at the

channel's downstream region, and increased mixing effects. Fig. 31(b) shows, for a high $x_{e,in} \approx 0.40$, increasing G has similar effects, but to a smaller extent due to the much smaller volume fraction of liquid in the incoming flow. Note that a much wider range of $G \approx 180 - 2400$ kg/m^{2}s was possible at $x_{e,in} \approx 0.04$, but only $G \approx 380 - 790$ kg/m^{2}s was practically possible at $x_{e,in} \approx 0.40$ to safeguard the system from very high flow velocities.

Overall, in both Figs. 30 and 31, both single- and double-sided heating yield similar trends and values of $\bar{h}$ and q''_{CHF} at similar operating conditions.

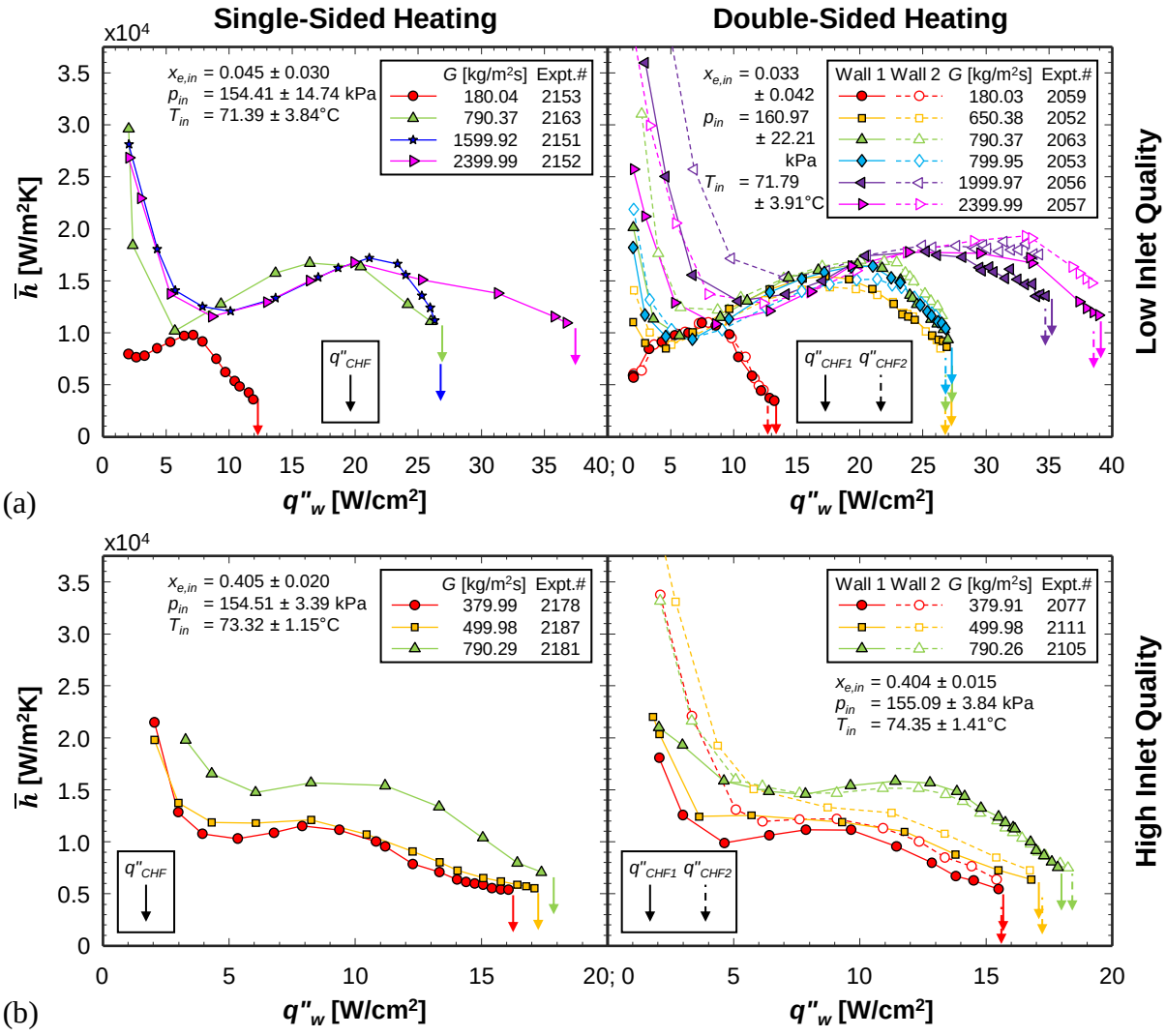

Fig. 31 Variations of average heat transfer coefficient, $\bar{h}$, versus wall heat flux, q''_w, for different mass velocities, G, with single- and double-sided heating at (a) low and (b) high inlet qualities, $x_{e,in}$.

In closing, the heat transfer data and flow visualization images presented in this study provide a foundation for CHF modeling, a major pursuit at PU-BTPFL since the 1980s [40,41], as

well as ongoing adaptation of machine learning methods, which have shown successes in correlating data for both flow boiling [42-44] and flow condensation [45]. Equally important is the usefulness of both the data and flow visualization results to validation of flow boiling CFD models [46,47].

5. Conclusions

This study explored flow boiling with liquid-vapor mixture inlet in the long-duration and stable microgravity environment onboard the ISS. nPFH is used in a rectangular channel of cross-section 5.0×2.5 mm^2 with single- and double-sided heating. Both flow patterns and heat transfer characteristics are explored in an elaborate manner by considering the parametric effects of mass velocity, inlet quality, inlet pressure, and heating configuration for heat fluxes ranging from a minimum until CHF. The present experiments for two-phase inlet on the ISS were successful and a large database was amassed for the first time in the literature, which can further be used for detailed analyses and modeling. Key conclusions are as follows:

(i) In general, flow patterns are comprised of HDFs and LDFs traversing the channel, the thicknesses of which depend on the operating conditions. Of all parameters, inlet pressure has a negligible effect on flow patterns. Double-sided heating depletes the HDFs faster than single-sided due to increased vaporization. Inlet quality most dictates the flow patterns followed by mass velocity. Combinations of low inlet quality and high mass velocity result in greater liquid fraction and dispersion within the channel. Variations in heat flux throughout each boiling curve do not result in visually perceivable differences in flow patterns.

(ii) Both the velocity and frequency of HDFs averaged over the channel length are higher during the high-density-dominant period compared to low-density at all operating conditions. Mean HDF velocity is higher for higher mass velocities and inlet qualities but is negligibly affected by wall heat flux and heating configuration.

(iii) Close inspection of the flow patterns suggests an annular flow entering the channel with a central vapor core surrounded by an annular liquid layer. The HDFs leave a trail of liquid layer deposited onto the heated walls. Boiling occurs within the liquid layer resulting in the formation of a vapor layer along the wall, which then lifts the liquid layer off the wall while trying to merge with the central vapor core. CHF occurs when the liquid layer completely lifts off or dryout occurs, both not providing the wall with any liquid for sustained boiling in the channel's downstream portion.

(iv) Flow boiling curves suggest heat transfer symmetry between the two walls for double-sided heating and repeatability of the present experiments in microgravity. Inlet pressure does not affect the heat transfer characteristics, but the walls are hotter at higher

pressures. Heating configuration does not significantly influence the heat transfer characteristics, except for a slightly larger q''_{CHF} for single-sided heating. Higher mass velocities augment heat transfer and the heat fluxes required for regime transitions. Inlet quality does not affect the nucleate boiling region but degrades both q''_{ONBD} and q''_{CHF}.

(v) The walls are nearly isothermal at lower heat fluxes, but at higher heat fluxes, the wall temperature profiles are shaped concave downward with a peak in the middle, which is dependent on the operating conditions.

(vi) Streamwise profiles of heat transfer coefficient are shaped concave upward shape with high heat transfer near the channel entrance and exit. At high heat fluxes, intermittent dryout causes the entire profiles to be completely degraded below the other heat fluxes.

(vii) Local heat transfer coefficient varies with local thermodynamic equilibrium quality in the same manner for both single- and double-sided heating, even though double-sided causes larger changes in local quality. Nucleate boiling regime is dominant at lower inlet qualities and convective boiling regime is dominant at qualities higher than 0.5-0.6.

(viii) For a fixed mass velocity, higher inlet qualities yield higher average heat transfer coefficients at lower heat fluxes and lower $\bar{h}$ at higher heat fluxes. For a fixed inlet quality, high mass velocities yield higher $\bar{h}$ at both lower and higher heat fluxes, while the nucleate boiling regime at intermediate heat fluxes is unaffected.

CRediT author contribution statement – **I. Mudawar**: Conceptualization, Methodology, Supervision, Writing – review and editing, Funding acquisition. **V.S. Devahdhanush**: Methodology, Software, Formal analysis, Investigation, Data curation, Writing – original draft, Writing – review and editing. **S.J. Darges**: Formal analysis, Investigation, Writing – original draft. **M.M. Hasan**: Conceptualization, Investigation, Writing – review and editing. **H.K. Nahra**: Investigation, Writing – review and editing. **R. Balasubramaniam**: Investigation, Writing – review and editing. **J.R. Mackey**: Investigation.

Declaration of Competing Interest – None. The authors declare that they have no known competing financial interests or personal relationships that could have appeared to influence the work reported in this paper.

Data Availability – The experimental raw data used in this paper will be publicly made available in a NASA repository later.

Acknowledgement – The authors are appreciative of the support of the National Aeronautics and Space Administration (NASA) under grant no. 80NSSC22K0328. The authors are also thankful to the FBCE personnel at NASA Glenn Research Center, Cleveland, Ohio, especially Nancy Hall (FBCE Project Manager), Rochelle May and Phillip Gonia (Software Engineering), Mark Sorrells

(Assembly, Integration and Test Lead), Jesse DeFiebre (Fluids Lead), Monica Guzik (FBCE Chief Engineer), and ZIN FCF Mission Operations Team, for their dedicated technical assistance and successful completion of ISS testing.

Appendix A. ISS Experiment Summary

Summaries of ISS experiments for two-phase inlet are provided in Tables A.1 and A.2 for single- and double-sided heating, respectively. To cross-reference the data reported in this study to the original database (which will be made available to the community via a NASA repository later), experiment reference numbers (Expt.#) are provided for each set of operating conditions, including mass velocity, G, inlet pressure, p_{in}, and inlet thermodynamic equilibrium quality, $x_{e,in}$. Due to considerable variations in p_{in} and $x_{e,in}$ along some boiling curves, ranges are provided instead of averages. The naming convention for Expt.# is the latter three digits of the four-digit number represents unique case numbers while the first digit (if present) represents the trial number. For example, Expt.# 277 denotes the first trial of case 277.

Table A.1 Summary of ISS microgravity experiments for flow boiling with two-phase inlet and single-sided heating. The included values represent averages or ranges of steady state datapoints along the respective boiling curve.

Experiment Reference Number (Expt.#)	G [kg/m^{2}s]	p_{in} [kPa]	$x_{e,in}$
2148	180.04	130.56 – 133.55	-0.001 – 0.000
2149	430.35	125.27 – 128.74	0.313 – 0.335
2150	790.38	124.19 – 131.08	0.074 – 0.098
2151	1599.92	155.87 – 164.19	0.071 – 0.091
2152	2399.99	162.91 – 178.84	-0.012 – 0.016
2153	180.04	130.59 – 135.03	0.034 – 0.041
2154	429.80	119.56 – 120.38	0.585 – 0.590
2155	790.32	120.71 – 129.45	0.173 – 0.199
3156	1599.96	163.93 – 173.89	0.116 – 0.146
2157	249.80	128.12 – 128.60	0.675 – 0.679
2158	430.30	121.89 – 124.44	0.468 – 0.472
3159	790.18	154.31 – 156.82	0.580 – 0.583
2161	180.06	150.48 – 152.46	-0.003 – -0.002
2162	430.37	156.04 – 160.67	0.227 – 0.239
2163	790.37	155.84 – 162.82	0.057 – 0.061
2165	180.01	151.97 – 156.23	0.000 – 0.000
2166	430.32	155.65 – 162.13	0.274 – 0.282
2170	430.34	153.53 – 155.62	0.466 – 0.468
2173	379.85	124.36 – 127.46	0.367 – 0.375
2174	499.96	122.48 – 126.26	0.354 – 0.370

2175	650.30	138.06 – 139.41	0.863 – 0.868
2176	790.22	147.58 – 151.71	0.441 – 0.460
2178	379.99	155.45 – 158.40	0.382 – 0.387
2179	499.97	153.99 – 157.86	0.337 – 0.350
2180	650.39	143.29 – 146.60	0.574 – 0.594
2181	790.29	146.74 – 151.09	0.430 – 0.436
2183	379.93	122.82 – 124.62	0.478 – 0.483
2184	499.98	119.89 – 122.22	0.496 – 0.500
2186	379.97	154.56 – 156.32	0.473 – 0.475
2187	499.98	152.46 – 155.70	0.412 – 0.419
269	790.33	125.12 – 133.09	0.098 – 0.119
271	499.96	156.70 – 162.38	0.150 – 0.169
273	499.96	155.45 – 160.85	0.223 – 0.237
275	499.96	153.26 – 160.41	0.271 – 0.276
277	500.02	153.51 – 158.34	0.362 – 0.368

Table A.2 Summary of ISS microgravity experiments for flow boiling with two-phase inlet and double-sided heating. The included values represent averages or ranges of steady state datapoints along the respective boiling curve.

Experiment Reference Number (Expt.#)	G **[kg/m^{2}s]**	p_{in} **[kPa]**	$x_{e,in}$
3049	179.89	140.33 – 153.14	-0.018 – 0.000
3050	379.91	124.48 – 129.67	0.370 – 0.384
2051	499.96	125.06 – 135.20	0.180 – 0.215
2052	650.38	127.37 – 140.44	0.026 – 0.074
2053	799.95	125.09 – 141.81	0.064 – 0.103
3054	1199.98	165.50 – 183.30	0.199 – 0.245
2055	1599.93	164.70 – 183.36	0.095 – 0.155
2056	1999.97	168.30 – 196.89	-0.009 – 0.062
2057	2399.99	164.11 – 198.64	-0.047 – 0.030
2059	180.03	150.61 – 161.57	-0.011 – -0.006
2060	379.91	156.69 – 162.97	0.282 – 0.305
2061	499.95	155.33 – 167.52	0.088 – 0.117
2062	649.92	155.63 – 168.88	0.034 – 0.066
2063	790.37	155.39 – 169.92	0.062 – 0.102
2068	180.15	130.12 – 134.86	0.042 – 0.054
3070	499.99	123.27 – 132.65	0.259 – 0.282
2071	650.41	121.82 – 135.10	0.161 – 0.200
2072	790.32	123.67 – 138.17	0.152 – 0.197
2073	1199.96	166.07 – 184.54	0.205 – 0.250
2074	1599.95	164.92 – 182.99	0.095 – 0.137
2075	1999.93	167.62 – 200.44	0.018 – 0.060
2076	180.04	151.82 – 160.84	-0.001 – 0.000

2077	379.91	155.75 – 160.75	0.380 – 0.389
2078	499.95	157.09 – 167.70	0.167 – 0.190
2079	650.44	155.68 – 167.82	0.088 – 0.121
4084	249.80	128.49 – 129.56	0.664 – 0.669
2086	499.96	121.48 – 128.79	0.337 – 0.357
2087	650.44	126.25 – 139.51	0.077 – 0.120
3088	790.30	153.75 – 157.08	0.551 – 0.557
2089	1199.97	166.95 – 184.64	0.205 – 0.250
2091	379.96	154.65 – 157.65	0.473 – 0.478
2092	499.97	155.02 – 164.34	0.246 – 0.266
2093	650.44	152.86 – 166.63	0.186 – 0.209
2096	249.90	128.21 – 129.82	0.749 – 0.781
2097	379.81	125.29 – 133.09	0.342 – 0.347
2098	499.96	121.36 – 127.84	0.409 – 0.423
2099	650.29	138.29 – 140.65	0.861 – 0.864
2100	790.23	154.64 – 158.21	0.556 – 0.563
2102	379.95	154.12 – 155.97	0.562 – 0.564
2103	499.98	154.15 – 162.10	0.320 – 0.338
2104	650.35	142.61 – 144.71	0.617 – 0.622
2105	790.26	145.68 – 155.35	0.413 – 0.424
2107	379.86	123.51 – 127.15	0.465 – 0.470
2108	499.98	120.72 – 124.53	0.489 – 0.496
2110	379.92	154.24 – 154.99	0.643 – 0.647
2111	499.97	153.84 – 159.93	0.395 – 0.409
270	790.41	123.05 – 139.58	0.089 – 0.131
272	499.97	156.63 – 166.28	0.143 – 0.170
274	499.95	155.47 – 164.68	0.215 – 0.239
276	499.97	153.34 – 162.32	0.280 – 0.298
278	499.99	153.62 – 160.47	0.361 – 0.377

Appendix B. Temporal Variations for a Typical Experimental Case

Temporal variations of T_{in}, T_{out}, T_{tc} (heating-strip temperatures), and q''_w are shown in Fig. B.1 for a typical experimental case, Expt.# 2149. The temperatures correspond to the left-side vertical axis and the heat flux to the right-side vertical axis. The operating conditions for the data presented in each plot are reported as "parameter = average ± standard deviation".

At time $t = 0^+$ s, the first heat increment is set, which results in a corresponding T_{tc} increase. Thereafter, heat is incremented every 120 s, which results in monotonic T_{tc} increases, and for each heat increment, all the temperatures become steady (or quasi-steady) during the 120-s waiting period. This is true excepting the last heat increment, during which, the downstream T_{tc} curves change their trend to a concave-upward shape and sharply increase. At $t \approx 2370$ s, $T_{tc1,6}$ reaches 122°C, at which point, the software senses CHF and lowers the FBM heat to a minimum. This

validates the assumption that CHF is the root cause for strip temperatures reaching 122°C for the FBCE design.

Since the flow is saturated all along the heated length, all heat is transferred via latent heat of vaporization, which occurs at the saturation temperature at local pressure within the channel. Saturated two-phase flow also means a significant pressure drop along the channel length, *i.e.*, $p_{in} > p_{out}$. This results in (i) the fluid being hotter at the inlet compared to the outlet for all heat increments, (ii) no significant variation in T_{in} and T_{out} as heat flux is incremented.

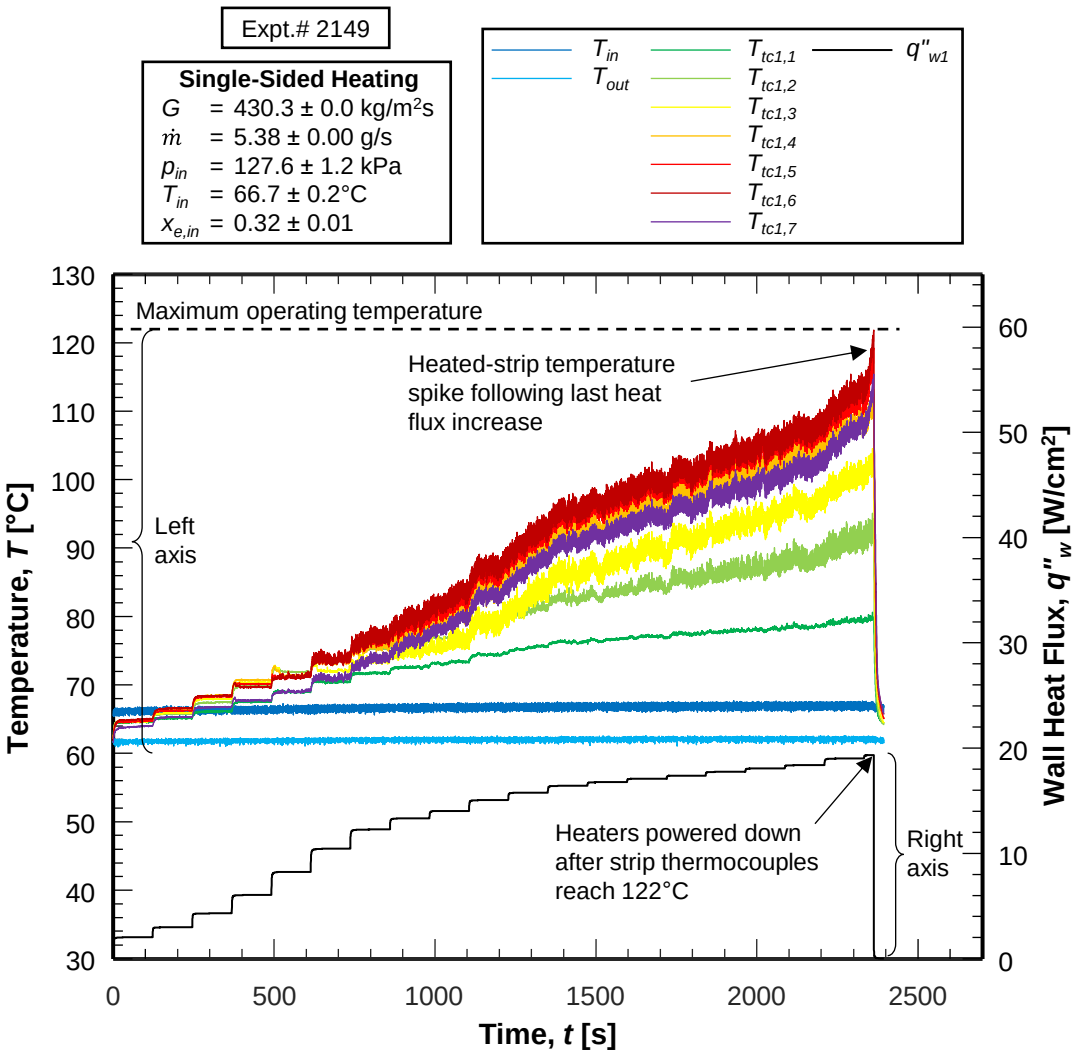

Fig. B.1 Temporal variations of fluid inlet (T_{in}), fluid outlet (T_{out}), and heating-strip temperatures (T_{tc}) for heat flux (q''_w) increments from a minimum until CHF for a typical experimental case with the following mean operating conditions: mass velocity of G = 430.3 kg/m^{2}s, mass flow rate of $\dot{m}$ = 5.38 g/s, inlet pressure of p_{in} = 127.6 kPa, fluid inlet temperature of T_{in} = 66.7°C, and inlet quality of $x_{e,in}$ = 0.32.

Appendix C. Estimation of Heat Losses and Determination of Fluid Enthalpy at FBM Inlet

The heat loss relevant to the present study pertains to the flow path between the BHM's inlet and the FBM heated section's outlet, which comprises losses from (i) the BHM, (ii) the flow plumbing between the BHM outlet and the FBM inlet, (iii) the FBM's development length, and (iv) the FBM's heated section. Of these, the latter, *i.e.*, heat loss from the FBM's heated section, is estimated to be within the FBM heater power's measurement uncertainty and considered negligible [38]. The FBM's wall heat flux, q''_w, is calculated as FBM heater power divided by the nPFH heating surface area.

Heat loss from the first three flow sub-sections can be cumulatively estimated as "net losses upstream of the FBM". To estimate this, a set of special experimental cases with near-saturated inlet ($0 < \Delta T_{sub,in} < 10$°C) were conducted prior to starting the regular experimental cases; these heat-loss experiments had a waiting period of 1200 s rather than the regular 120 – 180 s. This data was consolidated with regular near-saturated cases reported in [19] for single-sided heating and [32] for double-sided. The flow images of this consolidated "heat loss database" were manually analyzed to note all heat increments with no bubble presence within the FBM (be it nucleating within or entering from the upstream). Each ISS case is considered a single datapoint, *i.e.*, the temporal data is averaged from the second time instant until the instant where bubbles are not observed within the FBM. These efforts resulted in (i) a heat loss database with fully single-phase liquid flow from the BHM inlet to the FBM heated-section inlet, meaning purely sensible heat transfer, and (ii) BHM operation for these cases is practically very similar to the two-phase-inlet experiments of the present study, enabling applicability of these heat loss estimations to the latter. Percentage heat loss for each datapoint is estimated as

$$\%q_{net,loss} = \frac{q_{BHM} - \dot{m}\left(h_{in} - h_{BHM,in}\right)}{q_{BHM}} \times 100\%, \tag{C.1}$$

where q_{BHM} is measured heat input to the BHM and h_{in} and $h_{BHM,in}$ are fluid enthalpies at the FBM inlet and BHM inlet, respectively, and can be directly evaluated from local pressures and temperatures. Statistically, among all parametric relationships, $\%q_{net,loss}$ is most significantly affected by $\dot{m}$ and the best non-linear regression yields a *heat loss correlation* with a root mean square error of 1.89%, which is almost identical to the MST experiments [29] using a much smaller heat-loss database. With the leading constant fixed at 0.700, the ISS database yielded an exponent of -0.682 compared to the -0.680 for the MST; due to negligible difference between the two values and for consistency with previously analyzed data, -0.680 is used here to obtain the dimensional correlation,

$$\%q_{net,loss} = 0.700\dot{m}^{-0.680}, \tag{C.2}$$

where all parameters are in SI units. Fig. C.1 shows a comparison of experimental datapoints with the heat loss correlation in Eq. (C.2). Heat losses are significant at low flow rates. For the present two-phase inlet experiments, fluid enthalpy at the FBM inlet is determined from an energy balance

over the entire upstream region in conjunction with the upstream heat loss correlation (Eq. (C.2)) as

$$h_{in} = h_{BHM,in} + \frac{q_{BHM}}{\dot{m}}\left(1 - \frac{\%q_{net,loss}}{100\%}\right) = h_{BHM,in} + \frac{q_{BHM}}{\dot{m}}\left(1 - 0.007\dot{m}^{-0.68}\right), \qquad \text{(C.3)}$$

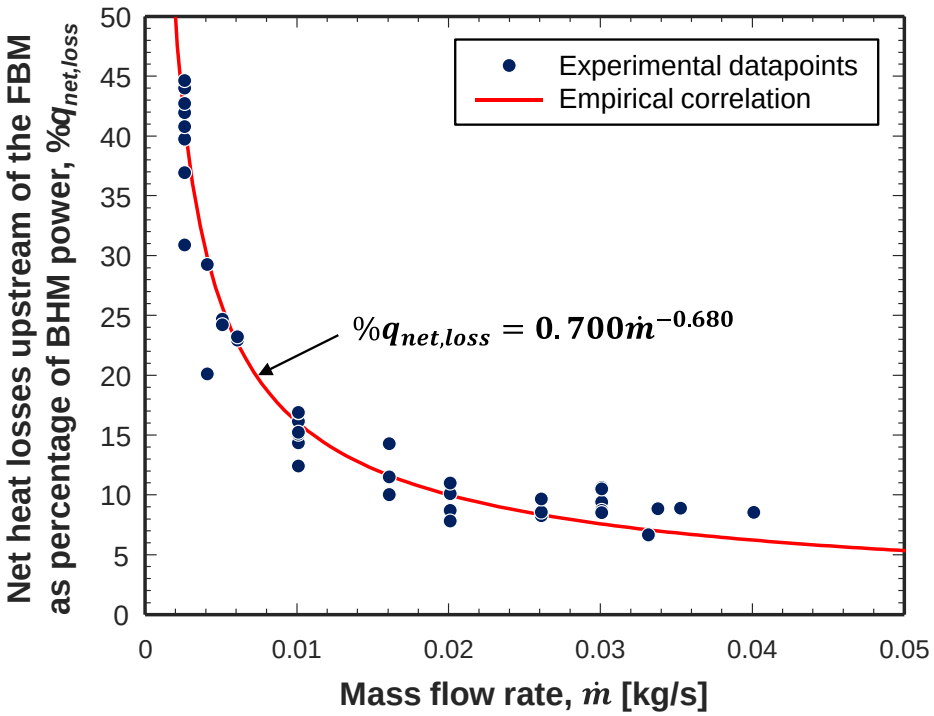

Fig. C.1 *Heat loss correlation* for experimental datapoints of heat loss for near-saturated inlet cases with no bubbles within the channel's heated section.

Appendix D. Image Sequences at Low Inlet Quality for Double-Sided Heating – Validation of the Effects of Heating Configuration

Figs. D.1 and D.2 display comparable operating conditions to Figs. 11 and 12 with $G \approx 500$ kg/m^{2}s and $x_{e,in} = 0.175$, but for double-sided heating with 24.87 and 95.21% q''_{CHF}, respectively. Flow patterns during the low-density-dominant period are similar to those observed for single-sided heating. The scarcity of liquid during these periods precludes distinct interfacial features along the wall. However, one noticeable difference between single- and double-sided heating is fading of HDFs along the channel is more pronounced for double-sided heating, especially at higher q''_w. In Fig. D.2(b), the HDF entering the channel at 0.0 ms is noticeably lighter at the end of the sequence compared to Fig. 12(b). During the high-density-dominant period, boiling within the liquid layer trailing the HDF is observed along both heated walls. At the lower q''_w shown in Fig. D.1(c), the HDF exits the channel at 645.5 ms and boiling is observed along both heated walls upstream of the HDF. To the contrary, at the higher q''_w shown in Fig. D.2(c), the heated walls appear relatively dry between successive HDFs as one exits the channel at 443.0 ms.

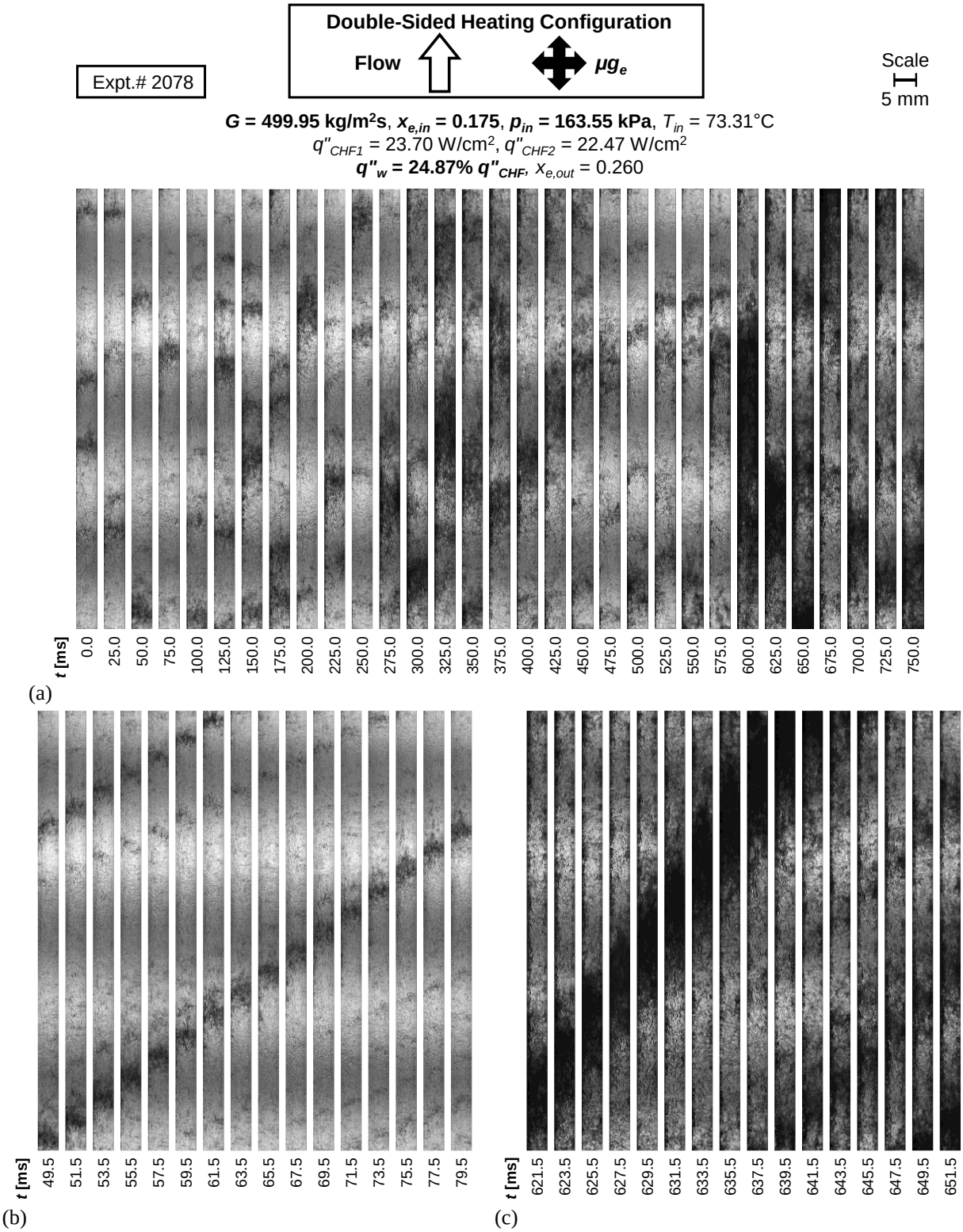

Fig. D.1 Flow visualization image sequences for double-sided heating with mass velocity of $G \approx 500$ kg/m²s, inlet quality of $x_{e,in} = 0.175$, and wall heat flux of $q''_w = 24.87\%\ q''_{CHF}$. Shown are (a) the overall transient behavior over an extended time period (25 ms between images), (b) low-density-dominant period (2 ms between images), and (c) high-density-dominant period (2 ms between images). Channel width is 5 mm.

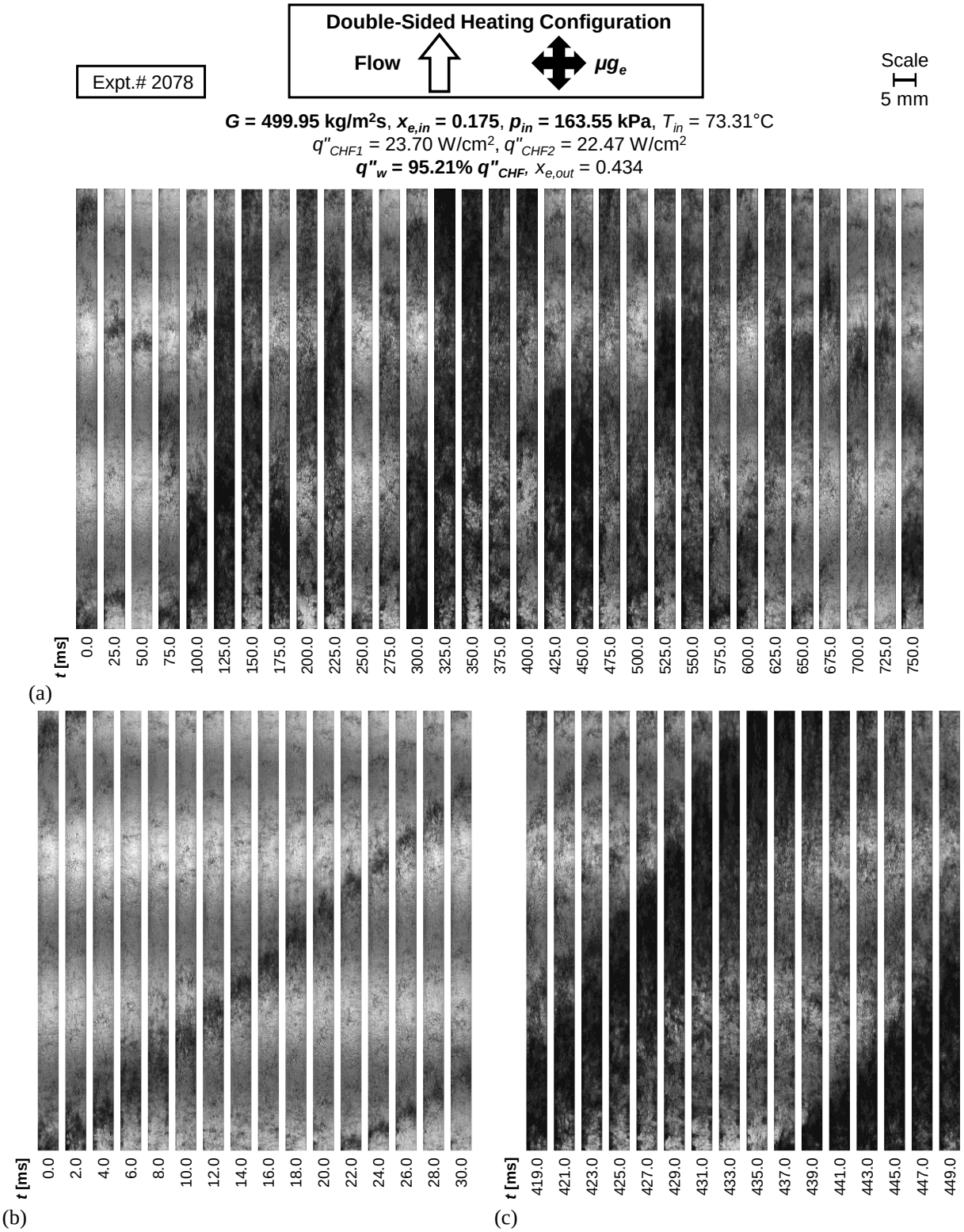

Fig. D.2 Flow visualization image sequences for double-sided heating with mass velocity of $G \approx 500$ kg/m²s, inlet quality of $x_{e,in} = 0.175$, and wall heat flux of $q''_w = 95.21\%\ q''_{CHF}$. Shown are (a) the overall transient behavior over an extended time period (25 ms between images), (b) low-density-dominant period (2 ms between images), and (c) high-density-dominant period (2 ms between images). Channel width is 5 mm.

Appendix E. Flow Patterns at Fixed High Inlet Quality – Effects of Mass Velocity

As observed in Fig. 18, flow patterns at high inlet qualities provide a limited amount of information regarding interfacial behavior, but some useful information may still be obtained regarding trends with respect to mass velocity. Fig. E.1 presents images of the average flow patterns along each boiling curve for double-sided heating at a relatively high $x_{e,in}$ range of 0.383 – 0.416, but different G. Each subfigure features a uniform size HDF aligned in the upstream portion of the channel at each heat increment presented. Fig. E.1(a) shows images for the lowest presented flow rate of $G \approx 380$ kg/m^{2}s. Heat flux does not impact flow patterns within the channel, and HDFs exist sporadically throughout the channel during each heat increment. Flow patterns are nearly identical at a higher G of 500 kg/m^{2}s, shown in Fig. E.1(b). Further increasing G to 790 kg/m^{2}s yields larger and darker HDFs, as shown in Fig. E.1(c). This is akin to the observations made in Fig. 22 at low $x_{e,in}$, in which increasing G resulted in more liquid throughout the channel. However, at high $x_{e,in}$, vapor occupies most of the channel.

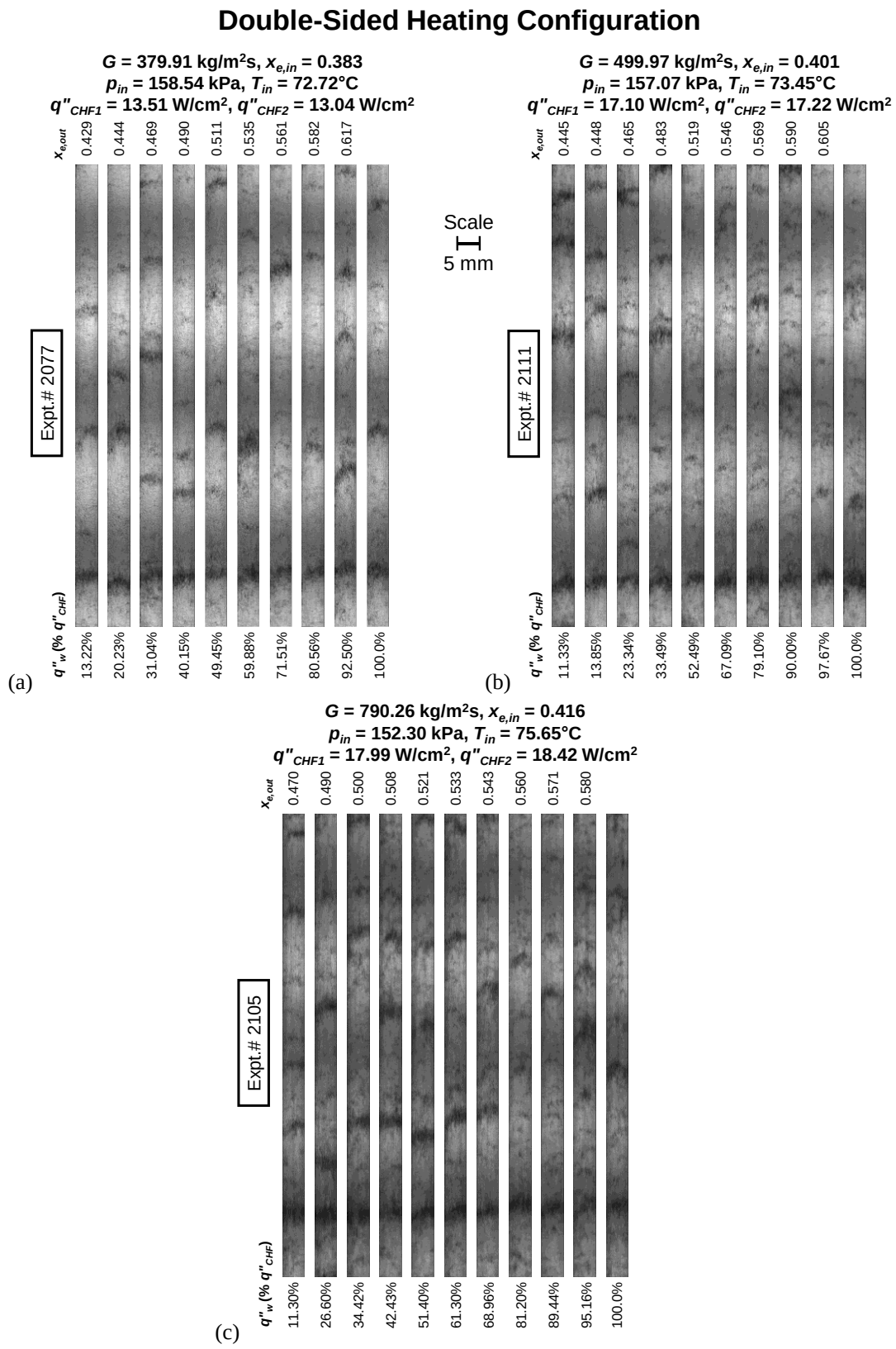

Fig. E.1 Flow patterns for increasing heat fluxes until CHF for double-sided heating at a fixed high inlet quality of $x_{e,in} \approx 0.400$ but different mass velocities of $G \approx$ (a) 380, (b) 500, and (c) 790 kg/m^{2}s. Channel width is 5 mm.

Appendix F. Heat Transfer Symmetry and Repeatability in Present Experiments

The representative flow boiling curves in Fig. F.1 help validate two aspects: (i) repeatability in the present microgravity experiments and (ii) symmetry in heat transfer between the two heated walls.

Firstly, Fig. F.1(a) for single-sided heating shows two experimental trials with identical operating conditions. Expt.# 2159 was performed on March 3rd, 2022, and 3159 on May 16th, 2022, with several experiments for other operating conditions between these two dates. Clearly, both trials yield identical nucleate boiling regions and q''_{CHF}. The degraded nucleate boiling region is slightly different due to the coarser heat increments for 2159 compared to 3159 resulting in slightly larger wall superheat increases. This indicates the necessity for finer heat increments for flow boiling experiments especially between ONBD and CHF to accurately capture the heat transfer characteristics and q''_{CHF}, which was in fact adhered to in the present study. Similarly, Fig. F.1(b) shows two experimental trials with identical operating conditions for double-sided heating: Expt.# 2050 and 3050, both performed on April 11th, 2022, with slightly different choices of heat increments to accurately capture CHF. Once again, both trials yield identical boiling curves with identical q''_{CHF}. This clearly proves the present experiments are indeed repeatable for both single- and double-sided heating.

Secondly, Fig. F.1(b) also shows the flow boiling curves for the two walls overlap, showing boiling heat transfer symmetry between the two walls. The slight differences could be due to experimental uncertainties or slightly different power supplied to each wall resulting in slightly different heat fluxes, cavity activation, and wall superheat.

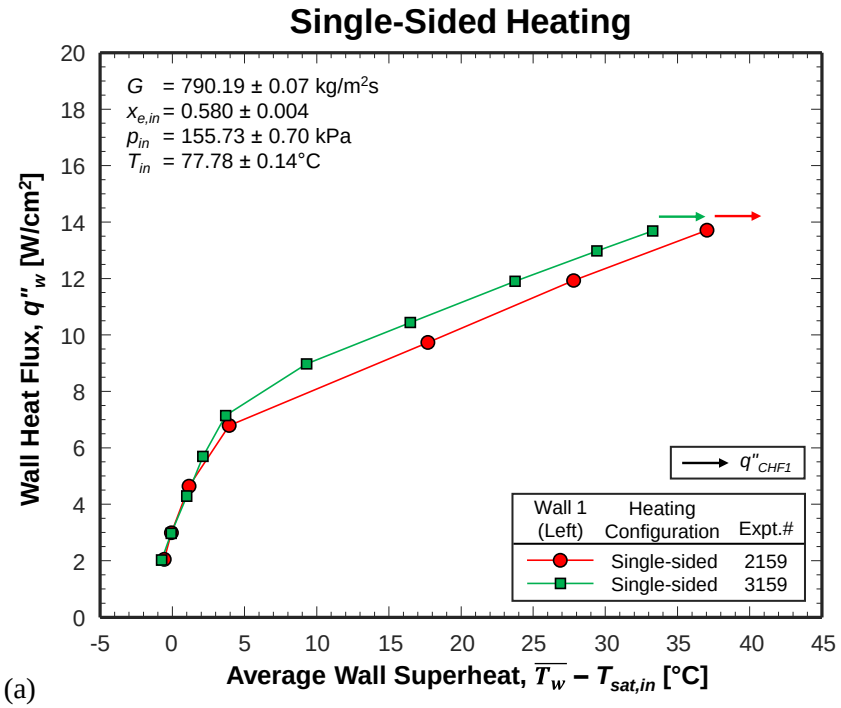

(a)

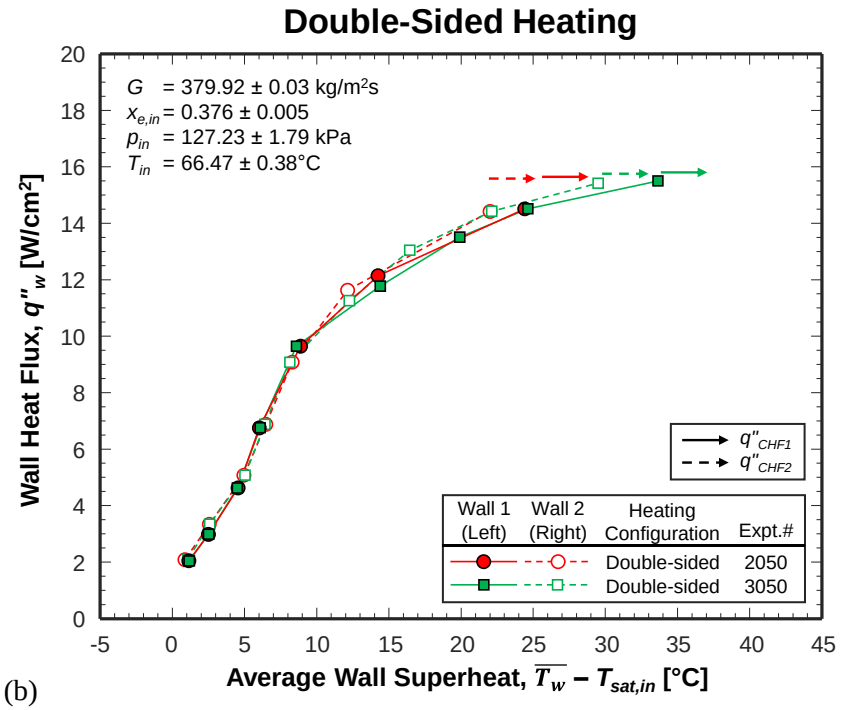

(b)

Fig. F.1 Boiling curves showing heat transfer symmetry and repeatability in microgravity flow boiling experiments for both (a) single- and (b) double-sided heating with two-phase inlet.

Appendix G. Effects of Mass Velocity and Inlet Quality on Boiling Performance for Double-Sided Heating

The effects of G and $x_{e,in}$ on boiling performance and associated parametric trends are similar between single- and double-sided heating.

With respect to G, Fig. 25 is similar to Fig. G.1 for $x_{e,in}$ = -0.002 – 0.558. Increasing G beyond 790 kg/m^{2}s does not enhance the convective properties of flow boiling with two-phase inlet for $x_{e,in} \geq 0.045$.

With respect to $x_{e,in}$, Fig. 26 is similar to Fig. G.2 for fixed $G \approx 180 – 790$ kg/m^{2}s. Much finer increments in $x_{e,in}$ were made for double- over single-sided and the monotonicity in some trends still hold true. For example, Fig. G.2(c) contains boiling curves for 14 different inlet qualities ranging from $x_{e,in}$ = 0.100 to 0.493 and all curves almost perfectly overlap in their nucleate boiling regions and q''_{CHF} monotonically decreases with increasing $x_{e,in}$ over the entire ranges, albeit some outliers exist within experimental uncertainties.

Double-Sided Heating

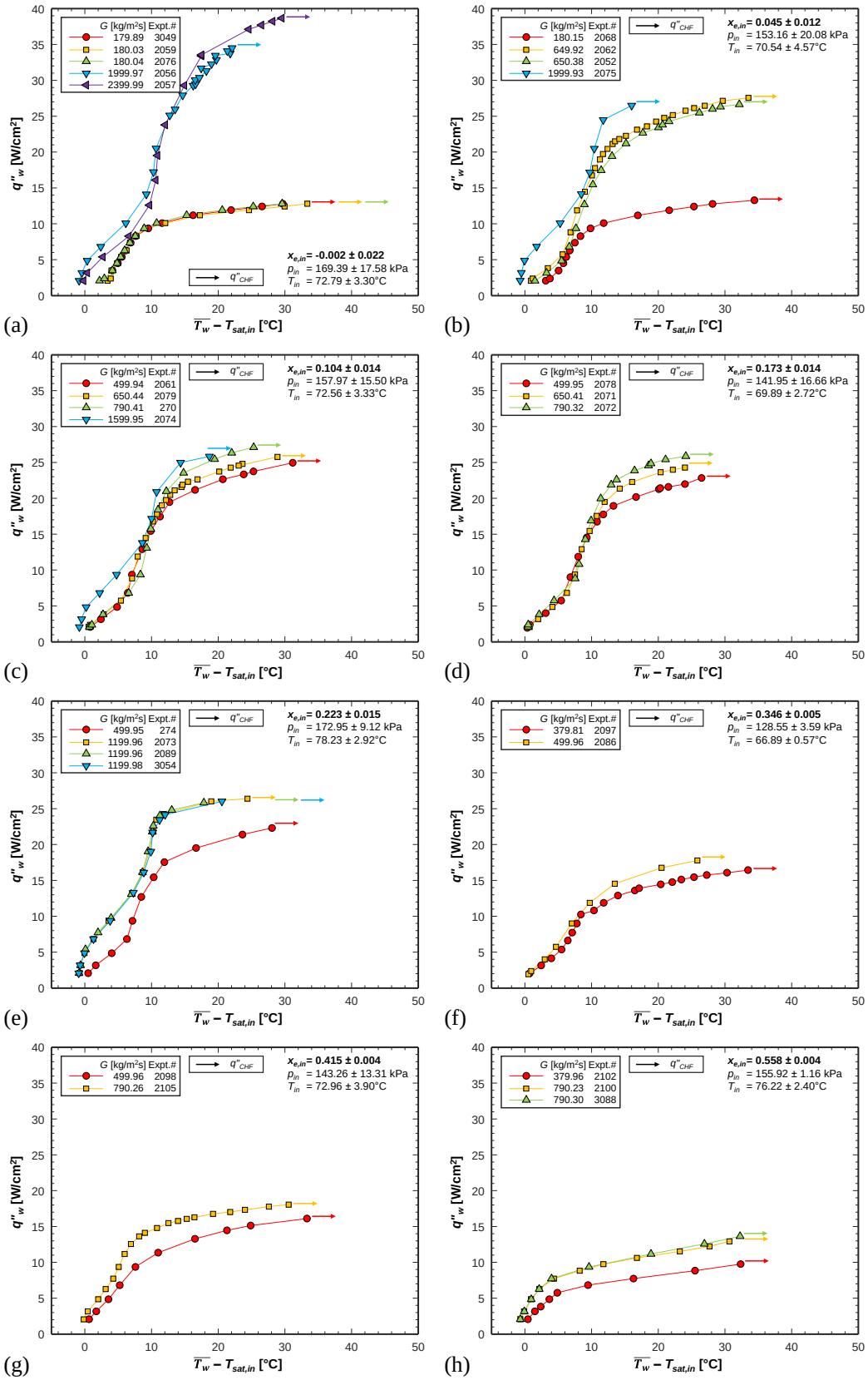

Fig. G.1 Microgravity flow boiling curves for two-phase inlet with double-sided heating, showing the effects of mass velocity at various fixed inlet qualities of $x_{e,in}$ = (a) -0.002, (b) 0.045, (c) 0.104, (d) 0.173, (e) 0.223, (f) 0.346, (g) 0.415, and (h) 0.558.

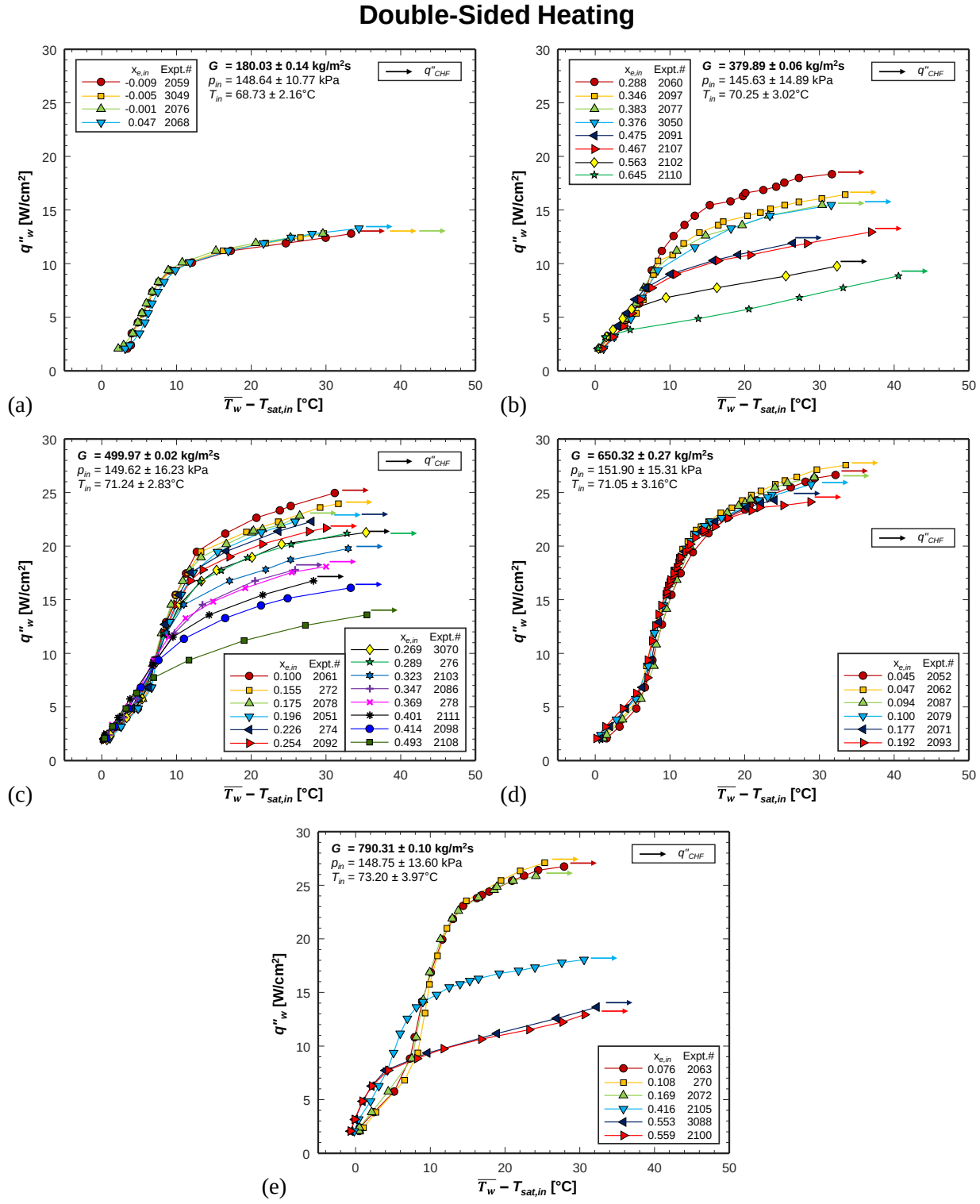

Fig. G.2 Microgravity flow boiling curves for two-phase inlet with double-sided heating, showing the effects of inlet quality at various fixed mass velocities of $G \approx$ (a) 180, (b) 380, (c) 430, (d) 500, and (e) 790 kg/m^{2}s.

References

[1] F.P. Chiaramonte, J. McQuillen, H.K. Nahra, P. Manoharan, H. Vanhala, B.J. Motil, J. Kim, V. Carey, W.G. Anderson, J. Plawsky, L. Carter, A. Jackson, 2019 NASA division of space and life and physical sciences research and applications fluid physics workshop report, NASA/CP-20205001256, NASA Glenn Research Center, Cleveland, OH, USA, 2020.

[2] I. Mudawar, Flow boiling and flow condensation in reduced gravity, in: Adv. Heat Transfer, 2017, pp. 225–306, doi: 10.1016/bs.aiht.2017.06.002.

[3] Y. Ma, J.N. Chung, An experimental study of forced convection boiling in microgravity, Int. J. Heat Mass Transfer 41 (15) (1998) 2371–2382.

[4] D.M. Iceri, G. Zummo, L. Saraceno, G. Ribatski, Convective boiling heat transfer under microgravity and hypergravity conditions, Int. J. Heat Mass Transfer 153 (2020) 119614, doi: 10.1016/j.ijheatmasstransfer.2020.119614.

[5] C. Konishi, I. Mudawar, Review of flow boiling and critical heat flux in microgravity, Int. J. Heat Mass Transfer 80 (2015) 469–493, doi: 10.1016/j.ijheatmasstransfer.2014.09.017.

[6] P. Di Marco, W. Grassi, Pool boiling in microgravity: Assessed results and open issues, in: Proceedings of 3rd European Thermal-Sciences Conference, Heidelberg, Germany, 2000, pp. 81–90.

[7] R. Raj, J. Kim, J. McQuillen, Pool Boiling Heat Transfer on the International Space Station: Experimental Results and Model Verification, J. Heat Transfer 134 (10) (2012) 101504, doi: 10.1115/1.4006846.

[8] H.S. Lee, H. Merte, F. Chiaramonte, Pool boiling curve in microgravity, J. Thermophys. Heat Transfer 11 (2) (1997) 216–222, doi: 10.2514/2.6225.

[9] H. Merte, Momentum effects in steady nucleate pool boiling during microgravity, Ann. N. Y. Acad. Sci. 1027 (2004) 196–216, doi: 10.1196/annals.1324.018.

[10] J.F. Zhao, G. Liu, S.X. Wan, N. Yan, Bubble dynamics in nucleate pool boiling on thin wires in microgravity, Microgravity Sci. Technol. 20 (2) (2008) 81–89, doi: 10.1007/s12217-008-9010-y.

[11] J.F. Zhao, J. Li, N. Yan, S.F. Wang, Bubble behavior and heat transfer in quasi-steady pool boiling in microgravity, Microgravity Sci. Technol. 21 (S1) (2009) 175–183, doi: 10.1007/s12217-009-9151-7.

[12] V.K. Dhir, G.R. Warrier, E. Aktinol, D. Chao, J. Eggers, W. Sheredy, W. Booth, Nucleate pool boiling experiments (NPBX) on the International Space Station, Microgravity Sci. Technol. 24 (5) (2012) 307–325, doi: 10.1007/s12217-012-9315-8.

[13] G.R. Warrier, V.K. Dhir, D.F. Chao, Nucleate pool boiling experiment (NPBX) in microgravity: International Space Station, Int. J. Heat Mass Transfer 83 (2015) 781–798, doi: 10.1016/j.ijheatmasstransfer.2014.12.054.

[14] H. Ohta, H. Asano, O. Kawanami, K. Suzuki, R. Imai, Y. Shinmoto, S. Matsumoto, T. Kurimoto, H. Takaoka, K. Fujii, M. Sakamoto, K. Sawada, H. Kawasaki, A. Okamoto, K. Kogure, T. Oka, K. Usuku, T. Tomobe, M. Takayanagi, Development of boiling and two-phase flow experiments on board ISS (Research objectives and concept of experimental setup), Int. J. Microgravity Sci. Appl. 33 (1) (2016) 330101, doi: 10.15011/ijmsa.33.330102.

[15] K. Inoue, H. Ohta, Y. Toyoshima, H. Asano, O. Kawanami, R. Imai, K. Suzuki, Y. Shinmoto, S. Matsumoto, Heat loss analysis of flow boiling experiments onboard International Space Station with unclear thermal environmental conditions (1st Report: Subcooled liquid flow conditions at test section inlet), Microgravity Sci. Technol. 33 (2) (2021) 28, doi: 10.1007/s12217-021-09869-5.

[16] K. Inoue, H. Ohta, H. Asano, O. Kawanami, R. Imai, K. Suzuki, Y. Shinmoto, T. Kurimoto, S. Matsumoto, Heat loss analysis of flow boiling experiments onboard International Space Station with unclear thermal environmental conditions (2nd Report: Liquid-vapor two-phase flow conditions at test section inlet), Microgravity Sci. Technol. 33 (5) (2021) 57, doi: 10.1007/s12217-021-09902-7.

[17] A. Sielaff, D. Mangini, O. Kabov, M.Q. Raza, A.I. Garivalis, M. Zupančič, S. Dehaeck, S. Evgenidis, C. Jacobs, D. Van Hoof, O. Oikonomidou, X. Zabulis, P. Karamaounas, A. Bender, F. Ronshin, M. Schinnerl, J. Sebilleau, C. Colin, P. Di Marco, T. Karapantsios, I. Golobič, A. Rednikov, P. Colinet, P. Stephan, L. Tadrist, The multiscale boiling investigation on-board the International Space Station: An overview, Appl. Therm. Eng. 205 (2022) 117932, doi: 10.1016/j.applthermaleng.2021.117932.

[18] P. Chorin, A. Boned, J. Sebilleau, C. Colin, O. Schoele-Schulz, N. Picchi, C. Schwarz, B. Toth, D. Mangini, Conception of a compact flow boiling loop for the International Space Station- First results in parabolic flights, Comptes Rendus. Mécanique 351 (S2) (2023) 1–20, doi: 10.5802/crmeca.147.

[19] I. Mudawar, V.S. Devahdhanush, S.J. Darges, M.M. Hasan, H.K. Nahra, R. Balasubramaniam, J.R. Mackey, Heat transfer and interfacial flow physics of microgravity flow boiling in single-side-heated rectangular channel with subcooled inlet conditions – Experiments onboard the International Space Station, Int. J. Heat Mass Transfer 207 (2023) 123998, doi: 10.1016/j.ijheatmasstransfer.2023.123998.

[20] A. Sharon, L. Chen, S.G. Bankoff, Convective boiling heat transfer in a concentric annular gap, Int. J. Multiphase Flow 9 (5) (1983) 545–560, doi: 10.1016/0301-9322(83)90017-4.

[21] C.R. Kharangate, L.E. O'Neill, I. Mudawar, L.E. O'Neill, I. Mudawar, L.E. O'Neill, I. Mudawar, Effects of two-phase inlet quality, mass velocity, flow orientation, and heating perimeter on flow boiling in a rectangular channel: Part 1 – Two-phase flow and heat transfer results, Int. J. Heat Mass Transfer 103 (2016) 1261–1279, doi: 10.1016/j.ijheatmasstransfer.2016.05.060.

[22] W. Li, K. Zhou, J. Li, Z. Feng, H. Zhu, Effects of heat flux, mass flux and two-phase inlet quality on flow boiling in a vertical superhydrophilic microchannel, Int. J. Heat Mass Transfer 119 (2018) 601–613, doi: 10.1016/j.ijheatmasstransfer.2017.11.145.

[23] S. Gong, Y. Mei, M.Y. Amin, B. Zhang, W. Ma, Orientation effect on heat transfer coefficient of a downward surface for flow boiling in a rectangular channel under low flow rate, Int. J. Heat Mass Transfer 153 (2020) 119594, doi: 10.1016/j.ijheatmasstransfer.2020.119594.

[24] Y. Huang, Q. Yang, J. Miao, K. Tang, J. Zhao, J. Huang, Y. Guo, Experimental investigation on flow boiling characteristics of a radial micro pin–fin heat sink for hotspot heat dissipation, Appl. Therm. Eng. 219 (2023) 119622, doi: 10.1016/j.applthermaleng.2022.119622.

[25] C. Konishi, I. Mudawar, M.M. Hasan, Criteria for negating the influence of gravity on flow boiling critical heat flux with two-phase inlet conditions, Int. J. Heat Mass Transfer 65 (2013) 203–218, doi: 10.1016/j.ijheatmasstransfer.2013.05.070.

[26] C. Konishi, H. Lee, I. Mudawar, M.M. Hasan, H.K. Nahra, N.R. Hall, J.D. Wagner, R.L. May, J.R. Mackey, Flow boiling in microgravity: Part 1 – Interfacial behavior and experimental heat transfer results, Int. J. Heat Mass Transfer 81 (2015) 705–720, doi: 10.1016/j.ijheatmasstransfer.2014.10.049.

[27] V.S. Devahdhanush, I. Mudawar, H.K. Nahra, R. Balasubramaniam, M.M. Hasan, J.R. Mackey, Experimental heat transfer results and flow visualization of vertical upflow boiling in Earth gravity with subcooled inlet conditions – In preparation for experiments onboard the International Space Station, Int. J. Heat Mass Transfer 188 (2022) 122603, doi:

10.1016/j.ijheatmasstransfer.2022.122603.

[28] S.J. Darges, V.S. Devahdhanush, I. Mudawar, H.K. Nahra, R. Balasubramaniam, M.M. Hasan, J.R. Mackey, Experimental results and interfacial lift-off model predictions of critical heat flux for flow boiling with subcooled inlet conditions – In preparation for experiments onboard the International Space Station, Int. J. Heat Mass Transfer 183 (2022) 122241, doi: 10.1016/j.ijheatmasstransfer.2021.122241.

[29] V.S. Devahdhanush, S.J. Darges, I. Mudawar, H.K. Nahra, R. Balasubramaniam, M.M. Hasan, J.R. Mackey, Flow visualization, heat transfer, and critical heat flux of flow boiling in Earth gravity with saturated liquid-vapor mixture inlet conditions – In preparation for experiments onboard the International Space Station, Int. J. Heat Mass Transfer 192 (2022) 122890, doi: 10.1016/j.ijheatmasstransfer.2022.122890.

[30] V.S. Devahdhanush, I. Mudawar, Subcooled flow boiling heat transfer in a partially-heated rectangular channel at different orientations in Earth gravity, Int. J. Heat Mass Transfer 195 (2022) 123200, doi: 10.1016/j.ijheatmasstransfer.2022.123200.

[31] S.J. Darges, V.S. Devahdhanush, I. Mudawar, Assessment and development of flow boiling critical heat flux correlations for partially heated rectangular channels in different gravitational environments, Int. J. Heat Mass Transfer 196 (2022) 123291, doi: 10.1016/j.ijheatmasstransfer.2022.123291.

[32] I. Mudawar, V.S. Devahdhanush, S.J. Darges, M.M. Hasan, H.K. Nahra, R. Balasubramaniam, J.R. Mackey, Effects of heating configuration and operating parameters on heat transfer and interfacial physics of microgravity flow boiling with subcooled inlet conditions – Experiments onboard the International Space Station, Int. J. Heat Mass Transfer (2023) under review.

[33] I. Mudawar, S.J. Darges, V.S. Devahdhanush, Parametric experimental trends, interfacial behavior, correlation assessment, and interfacial lift-off model predictions of critical heat flux for microgravity flow boiling with subcooled inlet conditions – Experiments onboard the International Space Station, Int. J. Heat Mass Transfer 213 (2023) 124296, doi: 10.1016/j.ijheatmasstransfer.2023.124296.

[34] W.A. Arnold, T.G. Hartman, J. McQuillen, Chemical characterization and thermal stressing studies of perfluorohexane fluids for space-based applications, J. Spacecr. Rockets 44 (1) (2007) 94–102, doi: 10.2514/1.22537.

[35] J. Lee, V.S. Devahdhanush, S.J. Darges, I. Mudawar, Effects of flow loop compressible volume position on system instabilities during flow boiling in micro-channel heat sinks, Int. J. Heat Mass Transfer 198 (2022) 123394, doi: 10.1016/j.ijheatmasstransfer.2022.123394.

[36] H. Zhang, I. Mudawar, M.M. Hasan, Flow boiling CHF in microgravity, Int. J. Heat Mass Transfer 48 (15) (2005) 3107–3118, doi: 10.1016/j.ijheatmasstransfer.2005.02.015.

[37] E.W. Lemmon, I.H. Bell, M.L. Huber, M.O. McLinden, NIST Standard Reference Database 23: Reference Fluid Thermodynamic and Transport Properties-REFPROP, Version 10, NIST, Gaithersburg, MD, USA, 2018.

[38] C. Konishi, I. Mudawar, M.M. Hasan, Investigation of localized dryout versus CHF in saturated flow boiling, Int. J. Heat Mass Transfer 67 (2013) 131–146, doi: 10.1016/j.ijheatmasstransfer.2013.07.082.

[39] S. Lee, V.S. Devahdhanush, I. Mudawar, Investigation of subcooled and saturated boiling heat transfer mechanisms, instabilities, and transient flow regime maps for large length-to-diameter ratio micro-channel heat sinks, Int. J. Heat Mass Transfer 123 (2018) 172–191, doi: 10.1016/j.ijheatmasstransfer.2018.02.020.

[40] D.E. Maddox, I. Mudawar, Critical heat flux in subcooled flow boiling of fluorocarbon liquid on a simulated electronic chip in a rectangular channel, Int. J. Heat Mass Transfer 32 (2) (1989) 379-394, doi:10.1016/0017-9310(89)90184-1.

[41] C.O. Gersey, I. Mudawar, Effects of heater length and orientation on the trigger mechanism for near-saturated flow boiling CHF - II. CHF model, Int. J. Heat Mass Transfer 38 (4) (1995) 643-654, doi:10.1016/0017-9310(94)00193-Y.

[42] Y. Qiu, D. Garg, L. Zhou, C.R. Kharangate, S. Kim, I. Mudawar, An artificial neural network model to predict mini/micro-channels saturated flow boiling heat transfer coefficient based on universal consolidated data, Int. J. Heat Mass Transfer 149 (2020) 119211, doi:10.1016/j.ijheatmasstransfer.2019.119211.

[43] Y. Qiu, D. Garg, S. Kim, I. Mudawar, C.R. Kharangate, Machine learning algorithms to predict flow boiling pressure drop in mini/micro-channels based on universal consolidated data, Int. J. Heat Mass Transfer 178 (2021) 121607, doi:10.1016/j.ijheatmasstransfer.2021.121607.

[44] I. Mudawar, S.J. Darges, V.S. Devahdhanush, Prediction technique for flow boiling heat transfer and critical heat flux in both microgravity and earth gravity via artificial neural networks (ANNs), Int. J. Heat Mass Transfer 220 (2024) 124998, doi:10.1016/j.ijheatmasstransfer.2023.124998.

[45] L. Zhou, D. Garg, Y. Qiu, C.R. Kharangate, S. Kim, I. Mudawar, Machine learning algorithms to predict flow condensation heat transfer coefficient in mini/micro-channel utilizing universal data, Int. J. Heat Mass Transfer 162 (2020) 120351, doi:10.1016/j.ijheatmasstransfer.2020.120351.

[46] I. Mudawar, J. Lee, Experimental and computational investigation into hydrodynamic and heat transfer characteristics of subcooled flow boiling on the International Space Station, Int. J. Heat Mass Transfer 207 (2023) 124000, doi:10.1016/j.ijheatmasstransfer.2023.124000.

[47] I. Mudawar, S. Kim, J. Lee, A coupled level-set and volume-of-fluid (CLSVOF) method for prediction of microgravity flow boiling with low inlet subcooling on the International Space Station, Int. J. Heat Mass Transfer 217 (2023) 124644, doi:10.1016/j.ijheatmasstransfer.2023.124644.